The Dissertation Committee for Graham William Piburn Certifies that this is the approved version of the following dissertation:

Development of Noble Metal Alloy Nanoparticles and Mesoporous Metal Oxides for Applications in Catalysis and Charge Storage

Committee:

Simon M. Humphrey, Supervisor

Michael J. Rose

Graeme A. Henkelman

David A. Vanden Bout

Charles J. Werth

Development of Noble Metal Alloy Nanoparticles and Mesoporous Metal Oxides for Applications in Catalysis and Charge Storage

by

Graham William Piburn, B.S.

Dissertation

Presented to the Faculty of the Graduate School of

The University of Texas at Austin

in Partial Fulfillment

of the Requirements

for the Degree of

Doctor of Philosophy

The University of Texas at Austin

May 2017

Dedication

For my Family

Acknowledgements

First, I must thank my advisor, Prof. Simon Humphrey, for his patience and guidance during my time here at UT. Working in his group has been a unique opportunity, and has helped me grow significantly as a scientist.

I would also like to thank the members of the Humphrey Group during my time here. In particular, I would like to acknowledge Pranaw Kunal, who has been an invaluable teammate in the nano-subgroup and whose advice has aided me a great deal over the years. I would also like to thank Luis Polanco, Joseph Reynolds, Sam Dunning, An Nguyen, and Ryan Riparetti, who make a splendid adventuring party. Of course, I would be remiss if I did not acknowledge Stephany García, upon whose work so much of my own is based.

Next, I would like to acknowledge my collaborators: Dr. Tyler Mefford and Prof. Keith Stevenson for testing the charge storage capabilities of my $LaMnO_3$ composites, and Hao Li and Prof. Graeme Henkelman for providing theoretical backing for my RhPd nanoparticle work. I also owe a debt of thanks to Drs. Karalee Jarvis, Hugo Celio, Dwight Romanovicz, Shouliang Zhang, and Vincent Lynch for sharing their technical expertise. Completing this work would have been immeasurably more difficult without their assistance.

Last, but far from least, I would like to thank my family, especially my parents, my siblings, and my wonderful fiancée, whose encouragement and belief in me kept me going through the darker days. I could not have come as far as I have without their support.

Development of Noble Metal Nanoparticles and Mesoporous Metal Oxides for Applications in Catalysis and Charge Storage

Graham William Piburn, Ph.D.

The University of Texas at Austin, 2017

Supervisor: Simon M. Humphrey

The creation of next-generation functional materials will require fine control of nanoscale surface characteristics. Two common approaches to this problem are the formation of nanoparticles and the synthesis of mesoporous materials. By incorporating nanoscale structural features, not only can a greater proportion of the material be devoted to active surface area, but properties can also emerge that are absent in the corresponding bulk material. For example, metals can be miscible on the nanoscale despite being immiscible in the bulk, and restrictive mesopores can lead to increased catalytic selectivity.

Mesoporous $LaMnO_3$-SiO_2 composites were synthesized by several different nanocasting routes using SBA-15 silica as the hard template. The final composites were stable in refluxing NaOH solution, indicating encapsulation of the remaining SiO_2 in each case, although the exact structure of the composites depended on the solvent mixture in which they were prepared. All three composites displayed respectable pseudocapacitative capabilities, with normalized specific capacitances over 200 F g^{-1}.

The next project revolved around the synthesis of RhPd alloy nanoparticles and the examination of their hydrogenation activity. RhPd alloy nanoparticles were synthesized using both microwave and conventional heating and a range of reaction

times. Application of these particles to the hydrogenation of cyclohexene revealed that particles synthesized at very short reaction times showed comparable reactivity to particles that had been heated for hours longer. In addition, the empirical finding that RhPd alloys have a hydrogenation activity between those of the two pure metals was further supported by DFT calculations.

Third, RhPdAu alloy nanoparticles were synthesized for use as hydrogenation catalysts. Tuning the exact composition of this alloy system is expected to influence the catalysts' activity, and the inclusion of gold may promote selective hydrogenation of the carbonyl bond in unsaturated aldehydes. A series of alloy compositions has been successfully synthesized, but their catalytic properties remain untested.

Finally, Rh nanoparticles supported on Co_3O_4 are also being studied for the selective hydrogenation of unsaturated aldehydes. Preliminary results suggest the mesoporosity of the support may play a crucial role in controlling the orientation of the substrate molecule, and therefore the selectivity toward the desired product.

Table of Contents

List of Tables

List of Figures

List of Schemes

Chapter One: Introduction

It is a common adage in the chemical sciences that structure determines function, and this is certainly true in the context of nanomaterials. Whether the structure under examination is the composition of an alloy nanoparticle or the dimensions of a pore only a few nanometers across, these features play significant roles in determining the properties of their respective materials, and therefore their suitability for a range of applications. This chapter is intended to serve as a general introduction to the fields of noble metal nanoparticles and mesoporous metal oxides, and provide some background knowledge on the characterization techniques and applications that will be explored with greater specificity in later chapters.

NOBLE METAL NANOPARTICLES

History and Properties

Metal nanoparticles, generally defined as particles with at least one dimension between 1 and 100 nm, have been used in some form for centuries in applications such as the coloring of stained glass; modern investigations into their structure and properties have developed significantly in the last sixty years.[1] Nanoparticles have attracted substantial interest in recent decades owing to their unique optical,[2-4] magnetic,[4-6] and catalytic properties,[7,8] which may differ significantly from the properties of the corresponding bulk materials. Many of the unusual properties of nanoparticles derive from their size and shape, including so-called quantum size effects.[9] For example, optical properties can change significantly due to the energies of particle-wide electron waves entering the visible spectrum.[10] These surface plasmon resonances lead to absorptions

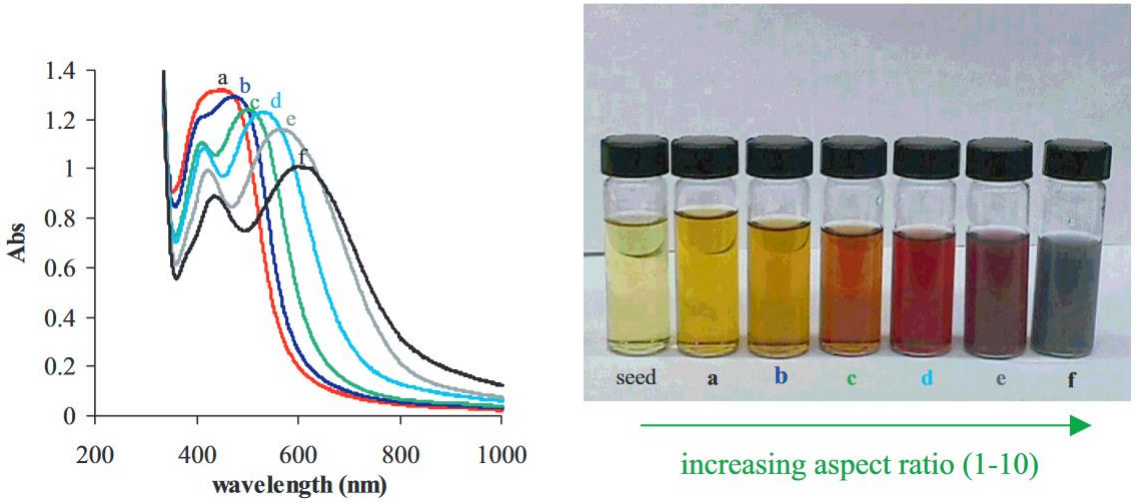

Figure 1.1. Right: photograph of 4 nm Ag nanoparticles and a collection of Ag nanorod samples with aspect ratios ranging from 1 to 10. Left: corresponding UV-vis spectra showing the shift of the surface plasmon resonances. Reproduced with permission from Wiley VCH. [11]

that would not otherwise be expected for that material. For example, gold spheres with diameters near 100 nm exhibit an absorption maximum at 575 nm, leading to a purple color.[7] The energy levels of these wave are heavily dependent on the size, shape, and composition of the particle. For comparison, gold spheres only 50 nm across appear red,[7] and silver nanorods with differing aspect ratios can vary from yellow to red to purple (Figure 1.1).[11]

The chemical properties of nanoparticles are also affected by their morphologies. Many metals, especially noble metals, are used as heterogeneous catalysts for a variety of reactions. These reactions occur at the surface of the metal, so increasing the surface area-to-volume ratio by making nanoparticles dramatically increases the number of active surface sites compared to the number of metal atoms that are trapped in the interior of the catalyst and are unable to participate in reactions.[12] Smaller particles also have more corner and edge sites, which are more reactive due to their greater degree of coordinative

unsaturation. Additionally, bottom-up syntheses can be tuned to produce shapes that only have one kind of exposed crystal facet; the identity of the exposed facet influences the activity of the surface with respect to a given reaction.[13] These factors combine to make metal nanoparticles more reactive than their bulk metal counterparts.

Synthesis of Noble Metal Nanoparticles

The synthesis of nanoparticles can be approached from either of two basic directions. If nanoparticles of a homogenous material that already exists in the bulk are desired, then that material could be ground to the point where the remaining grains were nanoparticles. However, this "top-down" approach offers little to no control over size or morphology, which are both important determiners of the properties of the particles, and it offers no opportunity to create new nanoscale materials. For these reasons, "bottom-up" approaches, in which nanoparticles are built up from precursor ions or molecules, are vastly preferred.[14,15] One way to further divide the wide range of bottom-up syntheses is to separate them into *in situ* supported methods, which produce nanoparticles on the surface of a solid support, and unsupported methods, which produce polymer- or ion-capped colloidal nanoparticles which may later be added to a solid support.

Synthesis of Nanoparticles inside Support Media

When synthesizing nanoparticles from atomic-level precursors, a key concern is to prevent uncontrolled agglomeration of the particles as they form. Since many applications involve nanoparticles attached to solid supports, one strategy is to have the intended support present during the synthesis of the nanoparticles such that the particles form directly on the support.[16,17] The presence of the solid support increases the odds

that nanoparticles will get stuck on the support surface as they form, thereby immobilizing them before they can agglomerate with other particles. This strategy is industrially popular as an efficient way to produce the desired active material, and has been used to synthesize a wide variety of particles. The support can be chosen to direct the morphology of the nanoparticles as they form, or to enhance the catalytic properties of the nanoparticles toward a desired application.[18-20] *In situ* supported syntheses can also circumvent issues that can arise from loading polymer-capped nanoparticles onto solid supports, such as agglomeration or uneven special distribution.

Synthesis of Unsupported Nanoparticles

Instead of relying on collisions with the support to prevent agglomeration, methods for the production of unsupported nanoparticles incorporate "capping agents" in the reaction solution.[21] These species bind to the surface of the nanoparticles as they form and provide a steric barrier to interactions between metal surfaces beyond a certain size. These capping agents can be organic ions, such as citrate, or large polymers, like polyvinylpyrrolidone (PVP). The choice of capping agent largely comes down to solubility and its affinity for the desired metal surface; smaller, stronger-binding capping agents favor forming smaller particles than do polymeric or weaker-binding ones.

In the synthesis of metal nanoparticles, the most common precursors are metal salts, from halides and acetates to more exotic organometallic species. It is therefore necessary to reduce the precursor metal ions down to the neutral atomic species to form the building blocks of the nanoparticles. Some syntheses incorporate a dedicated reducing agent for this purpose, commonly $NaBH_4$.[10] In syntheses involving citrate, the citrate can not only act as a capping agent, but also as a reducing agent by undergoing

decarboxylation.[22] Another popular and versatile approach to this problem is known as the "polyol method" in which a relatively small organic molecule with multiple alcohol groups, often ethylene glycol, acts as both the solvent and the reducing agent.[23,24] Both the usual precursor salts and polymeric capping agents tend to be readily soluble in polyols, and because the solvent is necessarily in massive excess with respect to the metal species, there is no noticeable change in the availability of the reducing agent over the course of the reaction.

Although unsupported nanoparticles require additional steps to anchor the synthesized particles to a support if that is the intended goal, they can provide an excellent degree of morphological control.[10,25] These methods also provide an opportunity not only to study the nanoparticles away from the support, but also to perform further modifications, such as the formation of core-shell structures,[26-28] exchanging capping agents,[29-31] or forming multipods on relatively isotropic cores.[32,33]

Microwave Synthesis

In most cases, the heat required to drive the reactions that form nanoparticles is provided by conductive means: the reaction vessel, whether an autoclave or a round-bottom flask, is heated directly by an oven or by an oil bath, and that heat must be transferred conductively into the solution. As a result, the solution is much hotter where it meets the container than it is at its core. Stirring relieves a great deal of this disparity within the solution, but a temperature gradient remains.[34] Such a gradient can lead to uneven reaction rates throughout the solution, leading to poorer morphological control. If the temperature must be changed during the procedure, the effects of the temperature

gradient are only exacerbated as different parts of the solution reach the necessary temperature to activate or deactivate a given reaction at different times.

Microwave heating has become an increasingly popular solution to these problems.[35] The method was first explored by organic chemists, who discovered that the more even and efficient heating provided by microwaves led to increased yields and improved selectivity for their desired products.[34] The key difference is the mechanism by which microwave irradiation heats the solution. As electromagnetic radiation, microwaves contain oscillating electric fields which interact with polar or charged species as they pass through the solution. Microwave frequencies occupy a "sweet spot" in the sense that the electric field oscillates slowly enough for chemical species to react to the changes in field polarity, but too fast for these species to be able to keep up perfectly. The failure of polar molecules to rotate quickly enough to keep pace with the changing electric field generates heat by dielectric loss. Ionic species in the solution also contribute by being dragged back and forth by the electric field, generating heat through collisions with other molecules. Because these heat-generating mechanisms occur directly in and throughout the solution, the heating provided is far more even and efficient, as diagrammed in Figure 1.2.[34]

Microwave heating has more recently been extended to materials synthesis, particularly the synthesis of metal nanoparticles.[35] Studies of pure rhodium nanoparticles showed that particles synthesized by microwave heating were more crystalline, had a tighter distribution of sizes and shapes, and contained more highly active surface sites, leading to greater catalytic activity as compared to particles made with conventional oil-bath heating.[31] Additional studies within the Humphrey Group have demonstrated the usefulness of microwave heating for producing thermodynamically disfavored Au@Rh core-shell structures[28] and even enabling the alloying of rhodium with gold and silver,

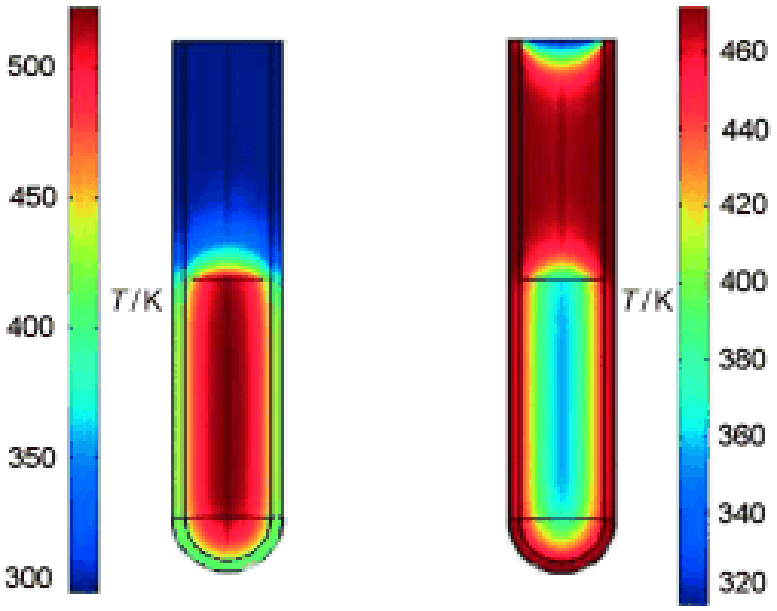

Figure 1.2. Comparison of the temperature gradients created within a test tube by microwave heating (left) and conventional, conduction-based heating (right). Reproduced with permission from Wiley VCH.[34]

which is not possible by conventional heating methods, even on the nanoscale.[36] Although the benefits of microwave heating in organic chemistry are now largely recognized to be thermal effects brought about by more efficient heating rather than characteristic microwave effects that result specifically from the presence of microwaves,[37] this may not be the case in materials syntheses. The ionic conduction mechanism of microwave heating does produce more heat than dipole rotation, so it would be reasonable to conclude that localized hotspots would exist around the metal precursor ions, increasing their reactivity or even their ability to anneal the nanoparticles as they form.[35,38-39] Perhaps more fascinatingly, studies of silver nanoparticles have shown that certain conditions that form isotropic silver particles under conventional heating form silver nanowires in the microwave. This morphological difference has been

attributed to the activation of certain facets of the forming particles by the flow of electrons conducted by the oscillating electric field of the microwaves.[40]

Microwave chemistry does have its drawbacks. Metal tools and measuring equipment must not be used within the microwave chamber, and uncontrolled agglomeration of metal particles could cause dangerous arcing if the particles reached *ca.* micron size.[41] Microwave reactions are also limited in terms of scale; since microwaves can only penetrate a solution to a depth of about 10 cm, there are clear limits to how large a reaction vessel can get without compromising homogenous heating.[42] However, this challenge is not insurmountable; investigations into continuous flow processing have shown great promise as a means of scaling up microwave-heated reactions.

Characterization Techniques

A wide variety of techniques are commonly used to analyze the structure and properties of nanoparticles. Some are common techniques that would be familiar in other areas of chemistry. For example, nanoparticles made of metals like gold have surface plasmon resonances detectable by UV-visible (UV-vis) spectroscopy, and the wavelengths of these absorptions can provide useful structural data.[43,44] Infrared (IR) spectroscopy and nuclear magnetic resonance (NMR) can be used to interrogate the organic capping agents commonly employed to control agglomeration, thereby revealing how much of the capping agent is bound directly to the nanoparticles.[31,45] X-ray powder diffraction (XRPD) is a valuable tool for verifying the crystallographic structure of a batch of nanoparticles by comparing the pattern produced to the existing database. Alloy diffraction patterns may be approximated by Vegard's law, which predicts that the lattice parameter of an alloy of two or more metals will be the weighted average of the

individual metals' lattice parameters, assuming all the components have the same general crystal structure; since most noble metals have face-centered cubic (fcc) structures, this assumption is typically valid for noble metal alloys.[46]

However, techniques such as those listed above are insufficient to fully characterize metallic nanoparticles. Many metals and alloys lack a surface plasmon resonance within the range of UV-visible spectrometers.[47] Although crystallite size can be approximated *via* the Scherrer equation[48], the sizes of polycrystalline particles cannot be judged by XRPD alone, nor can the distribution of particle diameters. More complex, polymetallic structures would also not be clearly distinguished; for instance, a Janus particle would appear identical to two separate monometallic particles by diffraction. Subtle surface features, such as a thin layer of one metal over the core of another, are also difficult or impossible to distinguish. The following techniques are ones that are often used to address these problems, and are all used in the projects discussed in later chapters.

Electron Microscopy

Electron microscopy is a critical tool for the study of nanoparticles because it enables the imaging of features smaller than the wavelength of visible light.[49] Because of the uncertainty principle, nanometer-scale objects are impossible to resolve using typical light microscopy; however, a high-energy beam of electrons has a much shorter de Broglie wavelength, allowing Angstrom-scale resolutions in the most advanced instruments. Electron microscopes are therefore ideal for examining the size and shape of nanoparticles.

All electron microscopes feature an electron source, generally a metal cone put under extremely high voltage, and a series of magnetic lenses to focus and direct the electron beam under high vacuum, but the details of where the beam is focused and where the detector is placed depend on the intended use of the microscope. Scanning electron microscopy (SEM) focuses the beam to a point at the surface of the sample and scans across the area being examined; the detector is placed at an angle above the sample, and the image is formed based on the secondary electrons ejected backward by collisions between beam electrons and the sample.[50] This reliance on secondary electrons makes SEM useful for examining surface features on bulk materials, since the sample does not need to be extremely thin to be effectively imaged. Additionally, the point-by-point raster enables granular analysis of regions of the sample material by methods like energy-dispersive X-ray spectroscopy (*vide infra*). However, SEM is limited in its ability to clearly image particles smaller than 10 nm.

By contrast, transmission electron microscopy (TEM) manipulates the electron beam such that it intersects the plane of the sample at a right angle at all points, then focuses that beam on a detector located directly below the sample.[51] In the standard "bright-field" imaging mode, electrons transmitted around the sample material form a bright background, and objects appear dark because they deflected the electron beam off the path to the detector. Because TEM relies on transmitted electrons, the sample must be kept extremely thin to allow the enough of the beam through to create contrast between the bright background and the darker features of interest. To this end, nanoparticle samples are typically supported on a thin layer of carbon backed by a copper grid; the carbon is thin enough that the high-energy electron beam is easily transmitted. TEM is the most common imaging technique used to examine nanoparticles, especially polymer-capped ones, but the thickness restrictions impose limits on imaging

nanoparticles attached to solid supports. In addition, the simultaneous illumination of the entire sample precludes granular analyses that are possible under SEM.

To address the latter shortcoming, some electron microscopes can be realigned such that the beam is focused on the sample plane. Because the beam scans across the area of interest but the electrons used to form the image are those being transmitted, this technique is called scanning transmission electron microscopy (STEM).[52] As in conventional TEM, the detector is located below the sample plane, but detectors used for STEM are usually ring-shaped, such that only electrons strongly deflected by inelastic collisions with sample atoms are collected. As a result, the background is dark instead of bright; this combination of detector and lens alignment is referred to as high-angle annular dark field STEM (HAADF-STEM). The size of the atoms in the sample directly correlates with their ability to deflect electrons to the detector, so HAADF-STEM can also distinguish elements of dramatically different atomic number by Z-contrast.

Energy-dispersive X-ray Spectroscopy

Raster-based electron microscopy techniques like SEM and STEM can be used to achieve point-by-point analysis of surface composition. Perhaps the most common means to do so is energy-dispersive X-ray spectroscopy, usually abbreviated EDX or EDS.[51,52] The incident electron beam has a high enough energy that it can eject core electrons from the atoms it hits. As electrons from higher energy levels within each affected atom drop down to fill the resulting gaps, the energy differences between these levels are emitted as X-rays, which are collected by a detector above the plane of the sample. Because the exact differences between energy levels vary by atomic number, the pattern of X-ray energies detected is diagnostic for the elements present in the sample.

This can be used to determine the elements present across an area of the sample being imaged, or, given enough resolution, can be used to construct a map of the elemental composition by recording the X-ray energies detected at each point during the raster.

Although extremely useful, especially as a compliment to electron microscopy, EDX does have its limitations.[51,52] EDX is unable to provide information about the chemical environments of the atoms it is interrogating because of the limited resolution (*ca.* 2 eV) of the energy-dispersive X-ray detector. It is also unable to detect elements lighter than beryllium. Propagation of the electron beam through the sample can lead X-rays to be emitted from a balloon-shaped region up to a micron deep below the surface; while this may be useful in gauging bulk composition, it can leave surface structure ambiguous. Worse, the ability of EDX to quantify composition varies depending on the nature of the sample. For extremely thin, flat samples that are homogenous within the interaction volume and composed of heavier elements, the results are reliable enough to be considered quantitative.[52] Departure from these assumptions, especially the inclusion of light elements such as oxygen, without the use of an internal standard leads to semi-quantitative results that are likely close, but not as accurate as other techniques.

X-ray Photoelectron Spectroscopy

X-ray photoelectron spectroscopy, or XPS, is another tool for determining the elemental composition of a surface. In a sense, XPS is the reverse of EDX: whereas EDX relies on high-energy electrons to produce characteristic X-rays, XPS exposes a sample under high vacuum to X-rays with a series of wavelengths and detects core electrons that have been ejected from surface atoms due to the photoelectric effect.[53] The

energies of these photoelectrons are related to the energy levels they were ejected from, and so can be used to identify the elements present in the surface, much like EDX.

However, there are several key differences between the abilities XPS and EDX to characterize a material. Regardless of the penetration depth of the incident X-rays, only photoelectrons from about the top 10 nm can escape the material due to their vulnerability to inelastic collisions and recombination events.[53] XPS is therefore a much more surface sensitive technique than EDX, but may produce misleading results if the sample is nonhomogeneous with respect to depth (*e.g.* polymer-coated nanoparticles) .[28] By incorporating ion sputtering into the experimental setup, XPS can be extended to provide accurate depth profiles of the composition of a material.[54] On the other hand, XPS instruments are not typically set up to do point-by-point mapping the way EDX can be. The most significant difference between the two comes as a consequence of their different detectors. Electron energies can be measured with more precision than can X-ray energies, and as a result XPS can distinguish between electrons ejected from atoms of the same element in different chemical environments, a difference usually *ca.* 2 eV.[52,53] XPS is also able to get quantitative signals from elements as light as lithium. Consequently, XPS is a valuable tool for quantifying not only the precise elemental composition of a surface, but also the oxidation states of the elements present.

Inductively Coupled Plasma Optical Emission Spectrometry

Inductively coupled plasma optical emission spectrometry (ICP-OES) is a technique for judging the bulk elemental composition of a sample.[55] The liquid solution to be analyzed is pumped into a nebulizer to disperse it into a mist, which is then fed into a high-temperature plasma flame, usually argon at about 7000 K. Collisions between the

ions and electrons of the plasma quickly ionize the components of the solution and rip its atoms apart from each other. As ions and electrons are separated and recombined repeatedly within the flame, each atom emits its characteristic spectrum based on the energy levels repopulated by captured electrons. By analyzing the wavelengths of light emitted during this process and the corresponding intensities, the elemental composition of the original sample can be determined.

ICP-OES is a powerful way to determine bulk sample composition, though it does have some drawbacks. Although other sample introduction methods exist that can accommodate solid particles, most common ICP-OES instruments are equipped to aerosolize liquids.[55] Consequently, solid samples must be dissolved, which often means digesting metals or other inorganic materials in strong acid, which is easier for some materials than others. ICP-OES offers accurate quantification of even trace amounts of most elements, though the use of aqueous solutions does preclude accurate analysis of oxygen in dissolved species.[55]

Noble Metal Nanoparticles as Hydrogenation Catalysts

Noble metals are key components of industrial and commercial catalysts for reactions ranging from carbon-carbon bond formation to exhaust gas reformation.[56-58] The catalytic focus of this dissertation will be on the hydrogenation of gas-phase organic molecules. Hydrogenation is a widely-used process that accounts for an estimated 10-20% of the catalysis done by industry, and is vital to fields as diverse as pharmaceuticals, cosmetics, and food products.[59] Unfortunately, the noble metals that enable hydrogenation on this scale are scarce in the Earth's crust, and this limited supply also makes them very expensive.[60] The efficient use of these metals is therefore of great

interest. As discussed above, the formation of nanoparticles is one way to get more active surface area out of the same amount of metal, but this strategy can be further improved upon by forming alloys or leveraging support interactions to tune the energies of the nanoparticles to better suit the reaction at hand.

Hydrogenation on a (111) Surface

Most noble metals possess a face-centered cubic (fcc) crystal structure.[61] As such, the most commonly exposed crystal facets presented by well-defined nanocrystals are the (111) and the (100) facets. A cubic particle with an fcc structure will be bounded by six (100) facets, whereas a perfectly octahedral particle with the same crystal structure will be bounded by eight (111) facets. Small noble metal nanoparticles often adopt the comparatively isotropic cuboctahedral structure, which is a truncated cube (or octahedron) with six square (100) faces and eight triangular (111) faces.[61] Since the (111) facet has the lower surface energy, it is typically used when modeling hydrogenation behavior on noble metal nanoparticles with a mixture of facets.[62]

The catalytic cycle for hydrogenation begins with hydrogen gas oxidatively adding to the metal surface to form two equivalents of hydride. Because of their small size, these hydrides are able to nestle into the threefold hollow sites on the (111) surface and gain stabilization from three separate metal atoms.[63] Next, the alkene binds to the surface *via* the π-orbital of its carbon-carbon double bond in a ligand association step. The alkene is much larger than the hydride and may contain bulky groups attached to either end; for this reason, the alkene is best accommodated by atop and bridge sites on the (111) surface.[63] One hydride then adds to the alkene by migratory insertion, causing the electrons that had been forming the alkene π-bond to instead form a σ-bond between

the opposite carbon and the metal surface. Another hydride adds to form the alkane by reductive elimination, returning a pair of electrons to the metal surface in the process. Although the cycle might be considered complete at this point for organometallic catalysts, heterogeneous catalysts must consider desorption of the product from the surface as the final step; after all, if the product remains physisorbed to the surface, then the active sites remain blocked and the catalyst cannot turn over. Although the example given was an alkene, the process would be fundamentally the same for any double bond. However, double bonds between different elements suffer from some degree of polarization, which leads them to bind to the surface asymmetrically and generally hydrogenate less favorably than alkene bonds.[64]

Alloy Formation and Reactivity

To make the catalytic cycle described above work, the metal surface must be able to dissociate hydrogen gas into hydrides and effectively bind the double bond of interest. This requires an energetic balancing act: if either reactant is bound too tightly, the catalyst will not be able to turn over. The interplay of these requirements can be seen in the volcano plot in Figure 1.3, in which the darker red colors toward the center indicate more optimal balance between hydrogen binding and alkene binding for the hydrogenation of cyclohexene.[36] Commonly used hydrogenation catalysts like rhodium and palladium can be found on the higher levels of this volcano, but they are not at the top; their hydrogen binding energies in particular are stronger than optimal.

One way to adjust the properties of a metal surface is to form an alloy instead of using a pure metal. Kitagawa and coworkers in particular have shown how mixing two metals in the same nanoparticle can adjust the electron energy profile of the material,

with surprising consequences for reactivity.[65] For example, the RuPd nanoparticles produced by that group had markedly higher activity toward CO oxidation than either of the component metals by themselves.[66] That same year, García *et al.* of the Humphrey Group reported the formation of RhAu and RhAg alloy nanoparticles, both of which were more active for hydrogenation than pure rhodium despite pure gold and silver being inactive for the same reaction. This can be partially understood by consulting the volcano plot in Figure 1.3.[36] As mentioned above, the hydrogen binding energy of rhodium is stronger than optimal; in contrast, both gold and silver have hydrogen binding

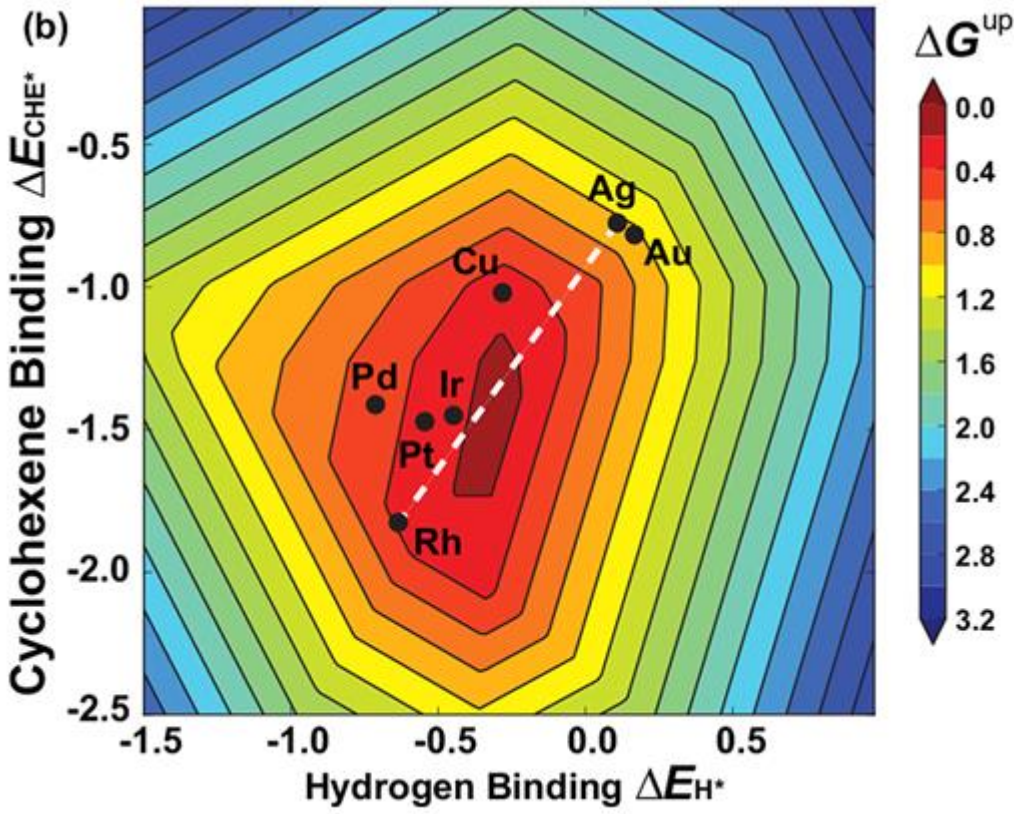

Figure 1.3. Volcano plot modeling the interplay of cyclohexene and hydrogen binding energies in determining the suitability of various metals to serve as hydrogenation catalysts. Reproduced with permission from the American Chemical Society.[36]

energies that are weaker than optimal, to the point that dissociation of hydrogen on a gold or silver surface is an endothermic process at room temperature. By drawing a line between the two metals on the volcano plot, one can predict that by alloying rhodium with either of the other two metals, a range of compositions would exist that would cross into the optimal region for reactivity; experimental study has shown this to be the case.[36] It is also interesting to note that all three of these alloy systems are immiscible in the bulk and can only be produced on the nanoscale; in addition, RhAu and RhAg can only be accessed by microwave synthesis.

Support Effects

In addition to the morphology and composition of the nanoparticles, the structure of any solid support they are attached to can also play a major role in the catalytic behavior of the system. These effects can take several different forms. First, metal nanoparticles supported on transition metal oxides can experience strong metal support interactions as a result of the overlap of d-orbitals in the support with orbitals in the nanoparticle.[67-69] These interactions serve to tune the electron energies within the nanoparticle, thereby influencing reactivity not unlike the alloying examples described above. Second, reactants can migrate along the surface of the catalyst and may cross the interface between nanoparticle and support. Taking hydrogenation as an example, hydrides dissociated by noble metal nanoparticles can migrate onto the surfaces of metal oxide supports, even if that metal oxide would not be able to dissociate hydrogen on its own.[70,71] This can lead to unique reactivity by the metal oxide surface.[72,73]

The support can also impact the reactivity of the system by influencing how the substrate interacts with the nanoparticle catalysts. A micro- or mesoporous support can

limit the orientations in which a prospective substrate molecule can approach the catalyst, which can increase the selectivity of the catalysis toward products that might not be favored otherwise.[74-77] Supports can also influence substrate orientation by creating favorable interactions between functional groups in the substrate and the support surface. For example, TiO_2 and Co_3O_4 have been shown to interact favorably with the carbonyl oxygen in unsaturated aldehydes, leading that group closer to the catalytically active surface and increasing the selectivity of hydrogenating the carbonyl bond with respect to the nearby alkene bond.[78,79]

MESOPOROUS METAL OXIDES

History and Properties

Porous materials are typically divided into three categories based on pore diameter: macroporous (greater than 50 nm), mesoporous (between 2 and 50 nm), and microporous (less than 2 nm).[80] Naturally occurring microporous metal oxides, also known as zeolites, have been known since the 18th century, and have found uses ranging from the catalytic cracking of hydrocarbons to gas separation and water purification.[81] Synthetic zeolites have been synthesized since the 1950s by templating the growth of the zeolite framework around alkaline cations and organic molecules, which could be subsequently removed.[81]. By contrast, the development of mesoporous metal oxides has been much more recent, following the discovery of mesoporous silica materials in the 1990s.[82-85] The different synthetic routes to these materials are described in the section below.

In general, the properties of mesoporous transition metal oxides are the same as those of their unstructured counterparts, with magnetic, catalytic, and optical properties

that are a direct result of the unfilled d-orbitals and multiple accessible oxidation states of most transition metals.[86] However, the porosity of the material can influence how the material interacts with its environment. Mesoporous materials commonly have specific surface areas of hundreds of square meters per gram, providing significantly more active surface area for catalysis or small molecule adsorption.[87] The pores also provide the possibility of excluding potential substrate molecules based on size. Only molecules or parts of molecules that are sterically unencumbered can fit into the pores, thereby adding selectivity to reactions catalyzed by species inside the pores. Even if the entire molecule can fit into the pore, the dimensions of the pore can restrict the orientation of the substrate molecule such that it may only be able to present one reactive functional group to the catalyst. These additional properties have made the synthesis of mesoporous metal oxides an area of great interest for the development of new functional materials.

Synthesis of Mesoporous Metal Oxides

The principle challenge in the synthesis of mesoporous metal oxides is how to impart an ordered porous structure on the final product. The general solution is to use an existing mesostructured material as a template to shape the metal oxide as if forms, then remove this template to liberate the desired material. Mesoporous syntheses can be divided into two basic categories based on what kind of material is used as the template: "hard-templated" routes rely on mesoporous solids, whereas "soft-templated" approaches employ self-assembling micellar arrays.

"Hard-template" Nanocasting Routes

The "hard-template" method for mesoporous metal oxide synthesis, also known as nanocasting, involves using a known mesoporous material to serve as a template to guide the assembly of the precursor salts or molecules.[88-91] For this to work effectively, the template material must have pores that are interconnected in some way; otherwise the metal oxide product would be doomed to collapse as soon as the template was removed. For example, SBA-15 silica has a hexagonal, honeycomb-like array of cylindrical mesopores that are connected to each other by a network of micropores; as a result, materials formed using SBA-15 as a template consist of a hexagonal arrangement of rods connected by smaller struts.[92]

The synthesis itself involves loading of the template with the metal precursor followed by annealing of the newly formed metal oxide and, finally, removal of the template. Impregnation of the template with precursor salts often relies on capillary action, either through slow dissolution of the solvent or because two solvents were used with radically different polarities. For instance, hexane is sometimes used to drive the precursors in a small amount of water into the pores of polar templates like silica.[90,91] Because the metal precursors tend to be ionic, a polar template is generally beneficial. Nonpolar materials like mesoporous carbons have also been used in (and produced by) hard-template routes, though it has been found to be helpful to oxidize the carbon surface to increase interactions between the metal precursor salts and the template.[92,93]

The primary benefit to hard-template methods is their robustness; because the template is a stable solid, heating it to the temperatures needed to anneal metal oxides is not typically a problem.[88-91] However, they do take significantly more time than most soft-template routes, since hard-template approaches require the production of at least one mesoporous intermediate. For example, the production of a metal oxide with the

same pore structure as SBA-15 by a hard-template route would first require the synthesis of SBA-15, then the production of a material with its inverse structure (*e.g.* the carbon material CMK-3), and finally the use of this inverse template to pattern the desired metal oxide.[94] The targeted material must also be stable enough to withstand whatever conditions are required to remove the template; for example, metal oxides templated by silica materials must be resistant to either alkali metal hydroxides or HF.

"Soft-template" Micellar Routes

The "soft-template" method for mesoporous metal oxide synthesis utilizes self-assembling micelles to impart structure to the oxide material as it forms.[95,96] This is the same strategy used to form mesoporous silica variations like SBA-15 or KIT-6.[97,98] As such, these routes offer direct access to such structures without having to undergo the lengthy process of producing a porous material, only to use it template the template for the actual metal oxide synthesis. However, achieving even gelation of the metal precursors around the micelles can be tricky and depend on precise pH and temperature control.[94] Furthermore, micellar templates may not be stable at higher temperatures, which can be limiting for metal oxides that require temperatures in excess of 400 °C to anneal.[87] Soft-templated metal oxides are typically less crystalline than their hard-templated counterparts for this reason.

Characterization Techniques

Many of the techniques used to analyze mesoporous metal oxides are the same as those used to characterize nanoparticles (*vide supra*). Electron microscopy provides a means of visualizing the pore structure, although oxides of heavier metals can be more

challenging to image by TEM except on their thinnest edges due to their greater deflection of the electron beam. EDX and XPS are both commonly used to assess the elemental composition of metal oxides, and vibrational spectroscopies like IR and Raman give insights into the structure and the functional groups terminating the surface. By far the most significant difference between the two analysis schemes is the inclusion of gas sorption analysis for mesoporous metal oxides.

Gas Sorption Analysis

Gas sorption analysis is a means of measuring the specific surface area of a material and assess its pore structure.[99] At cryogenic temperatures, dispersion forces are strong enough to bind gas molecules to solid surfaces. By adding carefully measured doses of a probe gas to an evacuated chamber containing a solid sample and tracking how much probe gas needed to be added to increase the pressure relative to a standard pressure, an adsorption isotherm can be constructed. The most commonly used probe gas is N_2, which is typically measured at the temperature of liquid nitrogen (77 K). The adsorption isotherm is stopped before reaching a relative pressure of 1.0 to avoid condensation in the sample vessel. The process is then usually performed in reverse, vacuuming out known quantities of gas while measuring the relative pressure to construct a desorption isotherm.

A significant amount of information can be extracted from gas sorption isotherms. First, the shape of the adsorption isotherm reveals whether the material in question is predominantly microporous, mesoporous, or macroporous/nonporous. Mesoporous materials, especially those with cylindrical mesopores like SBA-15 produce Type IV isotherms, characterized by a dramatic, S-shaped feature after monolayer formation is

complete.[100] This sharp rise is caused by capillary condensation, which happens when enough gas molecules have packed into the mesopores that they condense into a liquid; until the pores are completely filled, more gas molecules become trapped in this liquid phase and do not significantly add to the relative pressure. In addition to providing this qualitative knowledge, the adsorption isotherm can be used to calculate the specific surface area of the sample based on the known footprint of the probe gas and how much gas is required to form the first few monolayers on the surface (p/p_0 = 0.05 – 0.30); this is known as the BET method, and is best applied to mesoporous systems.[101]

Desorption isotherms also contain useful information. The BJH method for determining pore size, which assumes cylindrical mesopores, is based on the inflection of the desorption isotherm: the greater the drop at a specific point in the relative pressure scale, the more pores of the corresponding diameter.[102] The shape of the hysteresis between the adsorption and desorption isotherms indicates the shape of the pores in the sample. For example, a symmetrical hysteresis indicates that the pores are even and free of blockages, whereas a wedge-shaped hysteresis denotes a bottleneck in the pores that limits the flow of gas.[100]

Applications of Mesoporous Metal Oxides

Metal oxides are used for a wide variety of applications, but this work will focus on their uses in catalysis and energy storage. In both fields, the increased surface area that comes with mesoporosity has proven to be a great boon. Considering the diversity of reactivity among metal oxides, it is perhaps unsurprising that mesoporous metal oxides have been explored for a wide range of catalytic applications, including oxygen evolution, total hydrocarbon oxidation, various organic reactions, and fuel cell-related

reactions such as the oxidation of methanol or formic acid.[87] Mesoporous metal oxides have also been explored as supports for metal nanoparticle catalysts, which themselves have a diverse portfolio of catalytic applications.[103] Whether a metal oxide is used as a support or as the catalyst itself, the porosity of the material adds to the active surface area of the system per unit volume, typically increasing activity. However, with bulkier molecules, mesoporous catalyst supports can instead increase selectivity by excluding all potential substrate groups other than those that can fit into the pore.[74-77]

While some of the catalytic applications of mesoporous metal oxides are aimed at producing energy, these materials are also being explored as possibilities for storing energy. Pseudocapacitors are materials that can store energy by adsorption and subsequent intercalation of ions, typically assisted by oxidation state changes by the transition metal ions already present.[104] By far the most common use of this motif is the reversible intercalation of lithium ions into metal oxides; MnO_2 in particular has been well studied for this process in its mesoporous form.[92,105] Pseudocapacitors will be explored in greater detail in Chapter 2.

REFERENCES

1. F. J. Heiligtag, M. Niederberger, *Mater. Today* **2013**, *16*, 262-271.
2. M. Magnani, L. Galluzzi, I. J. Bruce, *J. Nanosci. Nanotechnol.* **2006**, *6*, 2302-2311.
3. S. Morneta, S. Vasseura, F. Grassteb, P. Veverkac, G. Goglioa, A. Demourguesa, J. Portiera, E. Pollertc, E. Duguet, *Prog. Solid State Chem.* **2006**, *34*, 237-247.
4. T. Kim, D. S. Kim, B. Y. Lee, Z. H. Kim, S. Hong, *Adv. Mater.* **2009**, *21*, 1238-1242.
5. L. Z. Zhang, G. Q. Tang, *Opt. Mater.* **2004**, *21*, 217-220.
6. Y. Sun, G. P. Wiederrecht, *Small* **2007**, *3*, 1964-1975.
7. M. C. Daniel, D. Astruc, *Chem. Rev.* **2004**, *104*, 293-346.

8. A. Roucoux, J. Schultz, H. Patin, *Chem. Rev.* **2002**, *102*, 3757-3778.

9. Y. Volokitin, J. Sinzing, L. J. de Jong, G. Schmid, M. N. Vargaftik, I. I. Moiseev, *Nature* **1996**, *384*, 621-623.

10. S. Eustis, M. A. El-Sayed, *Chem. Soc. Rev.* **2006**, *35*, 209-217.

11. C. J. Murphy, N. R. Jana, *Adv. Mater.* **2002**, *14*, 80-82.

12. D. Astruc, F. Lu, J. R. Aranzaes, *Angew. Chem. Int. Ed.* **2005**, *44*, 7852-7872.

13. W. Zang, G. Li, L. Wang, X. Zhang, *Catal. Sci. Technol.* **2015**, *5*, 2532-2553.

14. L. Shen, N. Bao, K. Yanagisawa, K. Domen, A. Gupta, C. Grimes, *Nanotechnology* **2006**, *17*, 5117-5123.

15. J. S. Wang, S. Yin, M. Komatsu, Q. W. Zhang, F. Saito, T. Sato, *Appl. Catal. B* **2004**, *52*, 11-21.

16. T. Tuval, A. Gedanken, *Nanotechnology* **2007**, *18*, 255601.

17. J. M. Campelo, T. D. Conesa, M. J. Gracia, M. J. Jurado, R. Luque, J. M. Marinas, A. A. Romero, *Green Chem.* **2008**, *10*, 853-858.

18. E. Rogemond, N. Essayem, R. Frety, V. Perrichon, M. Primet, F. Mathis, *J. Catal.* **1997**, *166*, 229-235.

19. Y. Sugiura, D. Mukai, Y. Murai, S. Tochiya, Y. Sekine, *J. Hypdrogen Energy* **2013**, *38*, 7822.

20. P. Zhang, S.-Y. Huang, B. N. Popov, *J. Electrochem. Soc.* **2010**, *157*, B1163-B1172.

21. S. Campisi, M. Schiavoni, C. E. Chan-Thaw, A. Villa, *Catalysts* **2016**, *6*, 185.

22. I. Ojea-Jiménez, J. M. Campanera, *J. Phys. Chem. C* **2012**, *116*, 23682-23691

23. F. Fievet, J. P. Lagier, M. Figlarz, *MRS Bull.* **1989**, *14*, 29-34.

24. F. Fievet, J. P. Lagier, B. Blin, B. Beaudoin, M. Figlarz, *Solid State Ionics* **1989**, *32-33*, 198-205.

25. C. Burda, X. Chen, R. Narayanan, M. A. El-Sayed, *Chem. Rev.* **2005**, *105*, 1025-1102.

26. P. Strasser, S. Koh, T. Anniyev, J. Greeley, K. More, C. Yu, Z. Liu, S. Kaya, D. Nordlund, H. Ogasawara, M. F. Toney, A. Nilsson, *Nature Chem.* **2010**, *2*, 454-460.

27. R. Harpeness, A. Gedanken, *Langmuir*, **2004**, *20*, 3431-3434.

28. S. García, N. Dahal, J. Zhou, H. Celio, A. Dolocan, S. M. Humphrey, *Chem. Commun.* **2013**, *49*, 4241-4243.

29. S. Peng, C. Wang, J. Xie, S. Sun, *J. Am. Chem. Soc.* **2006**, *128*, 10676-10677.

30. A. H. Latham, M. E. Williams, *Acc. Chem. Res.* **2008**, *41*, 411-420.

31. N. Dahal, S. García, J. Zhou, S. M. Humphrey, *ACS Nano*, **2012**, *6*, 9433-9446.

32. T. K. Sau, A. L. Rogach, *Complex-shaped Metal Nanoparticles*; Wiley-VCH Verlag & Co.: Weinheim, 2012.

33. S. M. Humphrey, M. E. Grass, S. E. Habas, K. Niesz, G. A. Somorjai, T. D. Tilley, *Nano Lett.* **2007**, *7*, 785-790.

34. C. O. Kappe, *Angew. Chem. Int. Ed.* **2004**, *43*, 6250-6284.

35. S. García, G. W. Piburn, S. M. Humphrey, *Microwave-assisted Synthesis of Metallic Nanoparticles*, In *Microwave Engineering of Materials – From Mesoscale to Nanoscale*, Ed. Erwann Guenin; Pan Stanford Publishing: Singapore, 2016.

36. S. García, L. Zhang, G. W. Piburn, G. Henkelman, S. M. Humphrey, *ACS Nano* **2014**, *8*, 11512-11521.

37. D. Obermayer, B. Gutmann, C. O. Kappe, *Angew. Chem. Int. Ed.* **2009**, *48*, 8321-8324.

38. J. Anwar, U. Shafique, W. uz-Zaman, R. Rehman, M. Salman, A. Dar, J. M. Anzano, U. Ashraf, S. Ashraf, *Arab. J. Chem.* **2015**, *8*, 100-104.

39. W. Wang, B. Wang, J. Sun, Y. Mao, X. Zhao, Z. Song, *RSC Adv.* **2016**, *6*, 52974-52981.

40. L. Gou, M. Chipara, J. M. Zaleski, *Chem. Mater.* **2007**, *19*, 1755-1760.

41. W. Chen, B. Gutman, C. O. Kappe, *ChemistryOpen* **2012**, *1*, 39-48.

42. M. B. Gawande, S. N. Shelke, R. Zboril, R. S. Varma, *Acc. Chem. Res.* **2014**, *47*, 1338-1348.

43. T. R. Jensen, G. C. Schatz, R. P. Van Duyne, *J. Phys. Chem. B* **1999**, *103*, 2394-2401.

44. S. K. Ghosh, T. Pal, *Chem. Rev.* **2007**, *107*, 4797-4862.

45. P. Kunal, H. Li, B. L. Dewing, L. Zhang, K. Jarvis, G. Henkelman, S. M. Humphrey, *ACS Catalysis* **2016**, *6*, 4882-4893.

46. A. R. Denton, N. W. Ashcroft, *Phys. Rev. A* **1991**, *43*, 3161.

47. Y. Xiong, J. Chen, B. Wiley, Y. Xia, Y. Yin, Z.-Y. Li, *Nano Lett.* **2005**, *5*, 1237-1242.

48. U. Holzwarth, N. Gibson, *Nature Nanotech.* **2011**, *6*, 534.

49. D. B. Williams, C. B. Carter, *Transmission Electron Microscopy: A Textbook for Materials Science*; Springer: Berlin, 1996.

50. L. Reimer, *Scanning Electron Microscopy: Physics of Image Formation and Microanalysis*; Springer: Berlin, 2013.

51. L. Reimer, *Transmission Electron Microscopy: Physics of Image Formation and Microanalysis*; Springer: Berlin, 2013.

52. K. J. Ganesh, M. Kawasaki, J. P. Zhou, P. J. Ferreira, *Microsc. Microanal.* **2010**, *16*, 614-621.

53. C. C. Chusuei, D. W. Goodman, *X-ray Photoelectron Spectroscopy*, In *Encyclopedia of Physical Science and Technology, Third Edition, Volume 17*; Academic Press: Cambridge, MA, 2002.

54. S. Oswald, W. Brückner, *Surf Interface Anal*, **2004**, *36*, 17-22.

55. X. Hou, B. T. Jones, *Inductively Coupled Plasma/Optical Emission Spectrometry*, In *Encyclopedia of Analytical Chemistry*; John Wiley & Sons Ltd: Chichester, 2000.

56. J. D. Burrington, *Industrial Catalysis: Chemistry and Mechanism*; Imperial College Press, London, **2016**.

57. K. C. Taylor, *Catal. Rev.* **1993**, *35*, 457-481.

58. L. Yin, J. Liebscher, *Chem. Rev.* **2007**, *107*, 133-173.

59. F. Nerozzi, *Platinum Metals Rev.* **2012**, *56*, 236-241.

60. P. Fröhlich, T. Lorenz, G. Martin, B. Brett, M. Bertau, *Angew. Chem. Int. Ed.* **2017**, *56*, 2544-2480.

61. Y. Xia, Y. Xiong, B. Lim, S. E. Skrabalak, *Angew. Chem. Int. Ed* **2009**, *48*, 60-103.

62. L. Vitosa, A. V. Rubana, H. L. Skrivera, J. Kollárb, *Surf. Sci.* **1998**, *411*, 186-202.

63. C. J. Heard, S. Siahrostami, H. Grönbeck, *J. Phys. Chem. C* **2016**, *120*, 995-1003.

64. P. Claus *Top. Catal.* **1998**, *5*, 51-62.

65. H. Kobayashi, K. Kusada, H. Kitagawa, *Acc. Chem. Res.* **2015**, *48*, 1551-1559.

66. K. Kusada, H. Kobayashi, R. Ikeda, Y. Kubota, M. Takata, S. Toh, T. Yamamoto, S. Matsumura, N. Sumi, K. Sato, K. Nagaoka, H. Kitagawa, *J. Am. Chem. Soc.* **2014**, *136*, 1864-1871.

67. S.-Y. Wang, S. H. Moon, M. Albert Vannice, *J. Catal.* **1981**, *71*, 167-174.

68. S. J. Tauster, *Acc. Chem. Res.* **1987**, *20*, 389-394.

69. X. Liu, M.-H. Liu, Y.-C. Luo, C.-Y. Mou, S. D. Lin, H. Cheng, J.-M. Chen, J.-F. Lee, T.-S. Lin, *J. Am. Chem. Soc.* **2012**, *134*, 10251-10258.

70. K.-W. Park, K.-S. Ahn, Y.-C. Nah, J.-H. Choi, Y.-E. Sung, *J. Phys. Chem. B* **2003**, *107*, 4352-4355.

71. V. B. Parambhath, R. Nagar, K. Sethupathi, S. Ramaprabhu, *J. Phys. Chem. C* **2011**, *115*, 15679-15685.

72. Z. Wu, Y. Mao, X. Wang, M. Zhang, *Green Chem.* **2011**, *13*, 1311-1316.

73. S. K. Beaumont, S. Alayoglu, C. Specht, N. Kruse, G. A. Somorjai, *Nano Lett.* **2014**, *14*, 4792-4796.

74. H. Shen, H. Tang, H. Yan, W. Han, Y. Li, J. Ni, *RSC. Adv.*, **2014**, *4*, 30180-30185.

75. N. Tiengchad, O. Mekasuwandumrong, C. Na-Chiangmai, P. Weerachawanasak, J. Panpranot, *Catal. Commun.* **2011**, *12*, 910-916.

76. C. Li, H. Zhang, D. Jiang, Q. Yang, *Chem. Commun.* **2007**, 547-558.

77. T. Maschmeyer, F. Rey, G. Sankar, J. M. Thomas, *Nature*, **1995**, *378*, 159-162.

78. G. Kennedy, L. R. Baker, G. A. Somorjai, *Angew. Chem. Int. Ed.* **2014**, *53*, 3405-3408.

79. G. Kennedy, G. Melaet, H.-L. Han, W. T. Ralston, G. A. Somorjai, *ACS Catalysis* **2016**, *6*, 7140-7147.

80. K. S. W. Sing, D. H. Everett, R. A. W. Haul, L. Moscou, R. A. Pierotti, J. Rouquérol, T. Siemieniewska, *Pure Appl. Chem.* **1985**, *57*, 603.

81. S. M. Auerbach, K. A. Carrado, P. K. Dutta (Eds), *Handbook of Zeolite Science and Technology*; Marcel Dekker: New York, 2003.

82. T. Yanagisawa, T. Shimizu, K. Kuroda, C. Kato, *Bull. Chem. Soc. Jpn.* **1990**, *63*, 988.

83. C. T. Kresge, M. E. Leonowicz, W. J. Roth, J. C. Vartuli, J. S. Beck, *Nature* **1992**, *359*, 710.

84. J. S. Beck, J. C. Vartuli, W. J. Roth, M. E. Leonowicz, C. T. Kresge, K. D. Schmitt, C. T.-W. Chu, E. W. Olson, S. B. Sheppard, J. B. McCullen, J. B. Higgins, J. L. Schlenker, *J. Am. Chem Soc* **1992**, *114*, 10834.

85. S. Inagaki, Y. Fukushima, K. Kuroda, *J. Chem. Soc., Chem Commun.* **1993**, 680.

86 A. D. McNaught, A. Wilkinson, *IUPAC. Compendium of Chemical Terminology, The Gold Book*, 2nd Edn; Blackwell Scientific Publications; Oxford, 1997.

87. D. W. Bruce, D. O'Hare, R. I. Walton (Eds), *Porous Materials*; John Wiley & Sons: Chichester, 2011.

88. F. Schüth, *Angew. Chem. Int. Ed.* **2003**, *42*, 3604.

89. A. Taguchi, F. Schüth, *Microporous Mesoporous Mater.* **2005**, *77*, 1.

90. F. Jiao, P. G. Bruce, *Adv. Mater.*, **2007**, *19*, 657.

91. F. Jiao, J. Bao, A. H. Hill, P. G. Bruce, *Angew. Chem. Int. Ed.* **2008**, *47*, 9711.

92. S. Jun, S. H. Joo, R. Ryoo, M. Kruk, M. Jaroniec, Z. Liu, T. Ohsuna, O. Terasaki, *J. Am. Chem. Soc.*, 2000, **122**, 10712-10713.

93. J. Roggenbuck, T. Waitz, M. Tiemann, *Micropor. Mesopor. Mat.* **2008**, *113*, 575-582.

94. N. Dahal, I. A. Ibarra, S. M. Humphrey, *J. Mater. Chem.* **2012**, *22*, 12675-12681.

95. P. Yang, D. Zhao, D. I. Margolese, B. F. Chmelka, G. D. Stucky, *Nature*, **1998**, *396*, 152.

96. P. Yang, D. Zhao, D. I. Margolese, B. F. Chmelka, G. D. Stucky, *Chem. Mater.* **1999**, *11*, 2813.

97. D. Zhao, J. Feng, Q. Huo, N. Melosh, G. H. Fredrickson, B. F. Chmelka, G. D. Stucky, *Science*, 1998, **279**, 548-552.

98. T.-W. Kim, F. Kleitz, B. Paul, R. Ryoo, *J. Am. Chem. Soc.* **2005**, *127*, 7601-7610.

99. D. W. Bruce, D. O'Hare, I. Richard, *Gas Sorption in the Analysis of Nanoporous Solids*, In *Multi Length-scale Characterization*; Wiley & Sons: Chichester, 2013.

100. P. B. Balbuena, K. E. Gubbins, *Langmuir*, **1993**, *9*, 1801-1814.

101. S. Brunauer, P. H. Emmett, E. Teller, *J. Am. Chem. Soc.*, 1938, **60**, 309-319.

102. E. P. Barrett, L. G. Joyner, P. P. Halenda, *J. Am. Chem. Soc.*, 1951, **73**, 373-380.

103. K. An, G. A. Somorjai, *Catal. Lett.* **2015**, *145*, 233-248.

104. P. Simon, Y. Gogotsi, *Nature Mater.*, 2008, **7**, 845-854.

105. J.-Y. Luo, J.-J. Zhang, Y.-Y. Xia, *Chem. Mater.* **2006**, *18*, 5618.

Chapter Two: Charge Storage in Mesoporous $LaMnO_3$-SiO_2 Composites

Mesoporous $LaMnO_3$ with bulk surface areas in the range 225–300 m^2 g^{-1} were prepared by direct overgrowth around the short-channel version of SBA-15 silica. The extent of $LaMnO_3$ growth was found to be affected by the polarity of solvent system used to impregnate the SBA-15 with La^{3+} and Mn^{2+} precursors. The resulting $LaMnO_3$-SiO_2 composites were stable in refluxing NaOH, suggesting that the SiO_2 was fully encapsulated. The composites were structurally characterized using a range of techniques including 2-D elemental mapping and Raman spectroscopy. The electrochemical behaviour of the composites were tested for their pseudocapacitance, which revealed normalized specific capacitances over 200 F g^{-1}.

NB: The contents of this chapter were previously published as G. W. Piburn, J. T. Mefford, N. Zinni, K. J. Stevenson, S. M. Humphrey, *Dalton Trans.* **2017**, *46*, 977. My contribution includes everything in this chapter except the electrochemical experiments and analysis.

INTRODUCTION

Efficient energy storage is a critical challenge facing modern technologies. Current electrolytic batteries have high energy densities, but tend to be slow to charge and discharge due to their reliance on slow redox reactions.[1-3] On the other hand, tradition capacitors can provide greater power density, but are unable to store as much total charge.[2] Pseudocapacitor materials represent an attractive middle ground between these two extremes.[4-6] The energy storage mechanisms common to pseudocapacitors rely

on the adsorption and rapid intercalation of ions and are less limited by potential thermodynamic phase transformations than those of battery materials, which allows pseudocapacitors to have greater power densities than batteries while maintaining superior energy densities to capacitors.[7-12] This rapid and reversible intercalation of ions is promoted by materials that can maintain overall charge balance thanks to the presence of metal ions that can easily access multiple oxidation states.[13-15] These intercalation-redox processes occur predominantly at the metal oxide surfaces. Unfortunately, most examples investigated thus far have been hampered by practical limitations, including higher synthesis costs and lower overall energy densities.[16-18] However, it has recently been shown that $LaMnO_3$, a mixed-metal oxide that conforms to the perovskite ABO_3 class, exhibits excellent energy density as well as fast charging and discharging rates.[19]

ABO_3-type perovskites, in which metal A is a lanthanide or alkaline earth metal ion and B is a transition metal ion, have attracted interest in recent decades for a variety of applications.[20-22] The B-site metal commonly supports multiple oxidation states, and ABO_3 lattices commonly contain oxygen vacancies. Therefore, such perovskites may exhibit catalytic activity for a variety of reactions, including CO and hydrocarbon oxidation, bifunctional oxygen electrocatalysis, and NO_x reduction.[20,23-25] The oxide vacancies have been shown to play an important role in these processes; in $LaMnO_3$, they also provide the basis for anion-based electrochemical charge storage.[19] It has been proposed that in alkaline solution, hydroxide ions can adsorb to the surface of $LaMnO_3$, which forces resident oxide ions to shift within the lattice in order to fill the oxide vacancies.[19] This intercalation of OH^- leads to the oxidation of local Mn^{2+} ions to Mn^{3+} and then Mn^{4+}. Incorporation of OH^- ions also encourages further Mn^{4+} ions to migrate toward the surfaces, leading to crystals with oxygen superstoichiometry.[19]

Since the processes described above that contribute to increased pseudocapacitance are surface-dependent, it is logical that the preparation of perovskites with increased accessible surface areas should be beneficial. As such, there have been an increased number of recent attempts to produce porous perovskites *via* adaptation of established solution-phase methods that have traditionally been used to prepare high-surface area silicas and transition metal oxides.[26-31] Notably, a direct soft-templated method using lauric acid as a structure-directing element has given $LaMnO_3$ with cylindrical pores *ca.* 2–2.5 nm in diameter and a surface area of 400 $m^2\ g^{-1}$.[26]

Nanocasting has become a popular alternative method for the synthesis of mesostructured metal oxides with ordered mesopores (Scheme 1, top).[32-36] Nanocasting is particularly useful for the formation of mesostructured metal oxides (*e.g.*, $LaMnO_3$) that cannot be easily obtained directly using soft (micellar) templates, for example in situations where the temperature required to convert molecular precursors into the desired oxide phase is incompatible with micellar stability. The carbon-based material CMK-3 generated by sucrose impregnation and carbonisation inside the mesoporous silica material SBA-15[37] has become a commonly used secondary hard template in nanocasting.[38] CMK-3 consists of bundles of cylindrical rods that can ultimately be used as a sacrificial scaffold for the formation of metal oxides with bulk structures that mimic the original SBA-15 hard templates (Scheme 2.1(ii)).[39-42] However, in comparison to direct soft-templated synthesis of mesostructured metal oxides, nanocasting involves arduous syntheses that can take days or weeks, and which are not easily scalable. Hard templates such as CMK-3 are also not ideally suited to impregnation with molecular precursors because their surfaces are primarily apolar, resulting in a lower affinity for impregnation with ionic species. Incomplete filling of templates commonly results in the formation of low surface area nanoparticles, due to the significant volumetric contraction

associated with the metal oxide formation step (Scheme 2.1(iii)). mesoporous materials by a number of nanocasting routes. However, most of these materials exhibit relatively low surface areas in comparison to the surface areas of the precursors templates.[34,43-45]

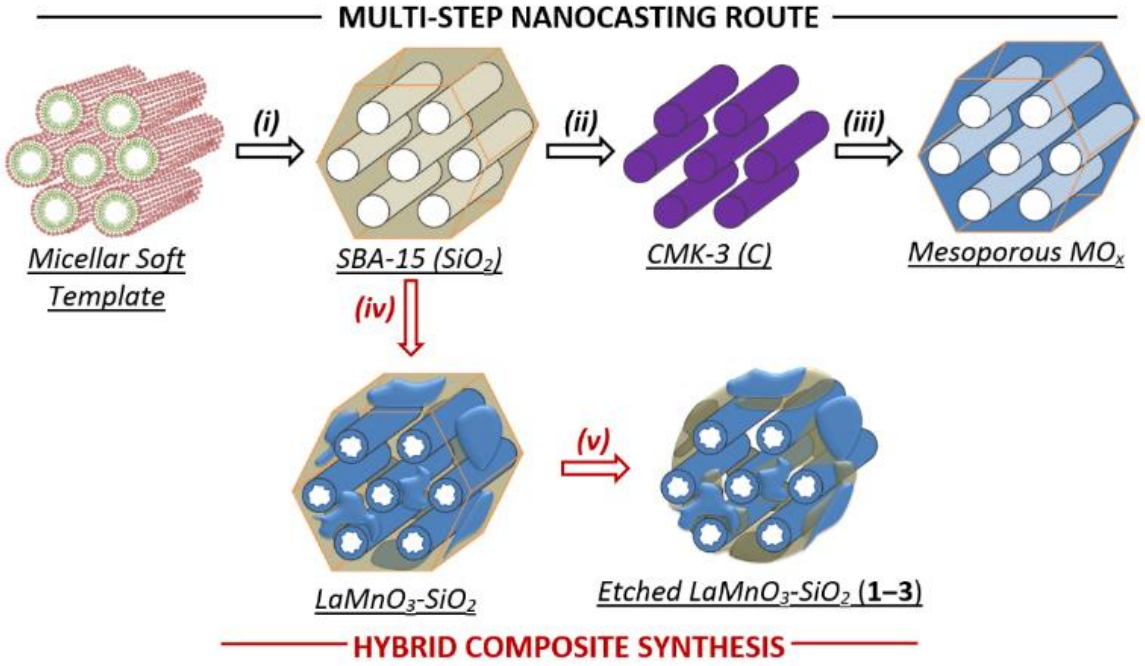

Specifically for $LaMnO_3$, recent attempts have been made to synthesize

Scheme 2.1. **Top:** example of a multi-step nanocasting method for the synthesis of mesoporous metal oxides: ***(i)*** formation of SBA-15 hard templates by gelling of $SiOR_4$ precursors and subsequent removal of surfactant template by calcination; ***(ii)*** CMK-3 amorphous carbon hard template with inverse SBA-15 structure, obtained by sucrose impregnation inside SBA-15 and subsequent SiO_2 removal by NaOH or HF treatment; ***(iii)*** formation of SBA-15-like mesoporous metal oxides by precursor impregnation around CMK-3 and subsequent calcination to remove the carbon template.

Bottom: synthetic route employed in this work: ***(iv)*** formation of $LaMnO_3$ over-layers around SBA-15 SiO_2 templates by La^{3+} and Mn^{2+} nitrate impregnation in different solvents, followed by calcination; ***(v)*** removal of exposed SiO_2 by etching in NaOH to afford the final mesoporous $LaMnO_3$-SiO_2 composites, **1**–**3**.

Reported materials have specific surface areas of no more than 100 m^2 g^{-1} and the materials lack long-range ordering of their pore structures, suggesting that template removal also results in partial structural collapse.[30-31,44]

In an attempt to circumvent the above synthetic issues, we decided to use short-channel (SC) SBA-15 as a sacrificial template for the synthesis of $LaMnO_3$ with nanorod-type structure. Ultimately, we discovered that $LaMnO_3$ could be formed around SC-SBA-15, using the latter as a physical support, to generate a mesostructured composite (Scheme 1, bottom). This approach represents an interesting hybrid between supporting $LaMnO_3$ nanoparticles on silica and the more arduous nanocasting of mesoporous $LaMnO_3$. Importantly, the hybrid mesoporous $LaMnO_3$-SiO_2 composites obtained have competitive surface areas in the range 200–300 m^2 g^{-1}, and demonstrate good pseudocapacitative characteristics through anion-based charge storage.

RESULTS AND DISCUSSION

Synthesis and Bulk Textural Properties

Initially, we attempted a simple synthesis strategy, to assess whether $LaMnO_3$ could be controllably grown around SBA-15, or whether rod-like aggregates were formed by complete pore filling (Scheme 2.1). The first step in the synthesis of the composites involved loading La^{3+} and Mn^{2+} precursor species inside the cylindrical pores of SC-SBA-15. Compared to the aforementioned inherent problems related to the use of CMK-3 as a hard template, the impregnation process is much easier for SC-SBA-15, primarily because the interior pore surfaces consist of polar silanol groups that form favourable weak interactions toward charged ions. In addition, the use of the short-channel variant

of SBA-15 further favours complete loading, because pore diffusion distances are significantly shorter and there are a higher proportion of pore openings per unit volume.

The loading and gelling processes were conveniently achieved in ethanol/water mixtures at 40 °C in SC-SBA-15 (Scheme 2.1(iv); SC-SBA-15 gas sorption data included in ESI). In this work, gelling was initiated by removal of excess solvents by evaporation from the composite mixture at 80 °C. The resulting colourless gel was slowly ramped to a temperature of 700 °C, at which point it was converted into the target mixed-metal oxide, confirmed by PXRD analysis and Raman spectroscopy (*vide infra*). Upon isolation of the dark brown $LaMnO_3$-SiO_2 composite, any excess SiO_2 that was exposed (*i.e.*, not fully encapsulated in a base-resistant $LaMnO_3$ overlayer) was removed by refluxing in a 2 M NaOH methanol-water solution (Scheme 2.1(v)). Different mixtures of methanol, ethanol, and water were tested in this step, and the effect of different alkali metal hydroxides was also assessed; no significant change in the extent of SiO_2 removal was observed. Meanwhile, second and third cycles of hydroxide treatment did not result in the removal of any further SiO_2, indicated by the percent mass loss and EDXS analysis (See Figure 2.11 at the end of this chapter).

Initial TEM analysis of the NaOH-treated product **1** obtained *via* the water-ethanol precursor impregnation route revealed micron-sized particles with ordered pore structures similar to the initial SC-SBA-15 templates (For SC-SBA-15 N_2 sorption data, see Figure 2.9 at the end of this chapter). The bulk textural properties of **1** were assessed using N_2 as a probe adsorbate. The adsorption-desorption isotherm (78 K; p/p_0 = 0–0.95) was type-IV with a narrow but symmetric hysteresis over the range p/p_0 = 0.6–0.9, indicative of bulk mesoporosity with regular cylindrical-shaped pores (Figure 2.1). This assumption is supported by the BJH pore size distribution plot (obtained using the entire desorption isotherm data),[46] which indicates a single pore size with a narrow size

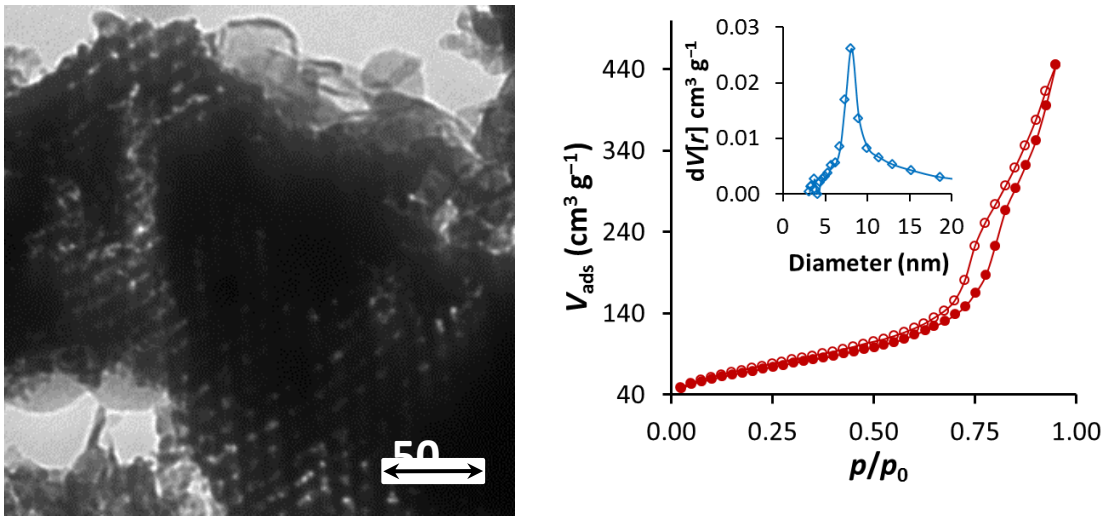

Figure 2.1. TEM image (left), N_2 sorption isotherm (right), and BJH plot (right, inset) for composite **1**.

distribution, *ca.* 8.1 nm. By comparison, the average pore size of the precursor SC-SBA-15 was 10.1 nm, while the average pore size in CMK-3 (actually the distance between individual rods) is in the range 2.0 – 3.8 nm (Figures 2.9 and 2.10). The BET[47] surface area of composite **1** was 245 m^2 g^{-1}, which compares favourably to other high surface area $LaMnO_3$ materials.[26,34] The inability to remove all SiO_2 after refluxing in NaOH as determined by EDS and XPS (Figures 2.5 and 2.7) further support the BET and TEM studies, and suggest that the $LaMnO_3$ had encapsulated the SiO_2 templates.

One reasonable explanation for the apparent growth of $LaMnO_3$ around the SC-SBA-15 is that insufficient La^{3+} and Mn^{2+} precursors were loaded inside the pores to form continuous rods akin to CMK-3, yet favourable interactions between the precursor ions and the $Si(OH)_x$-terminated SC-SBA-15 pore surfaces resulted in formation of continuous $LaMnO_3$ structures as depicted in Scheme 2.1(iv). To further probe this theory, we next decided to explore similar syntheses in less polar solvent mixtures. Yen *et al.*[48] recently showed that high surface area metal oxides could be obtained by grinding

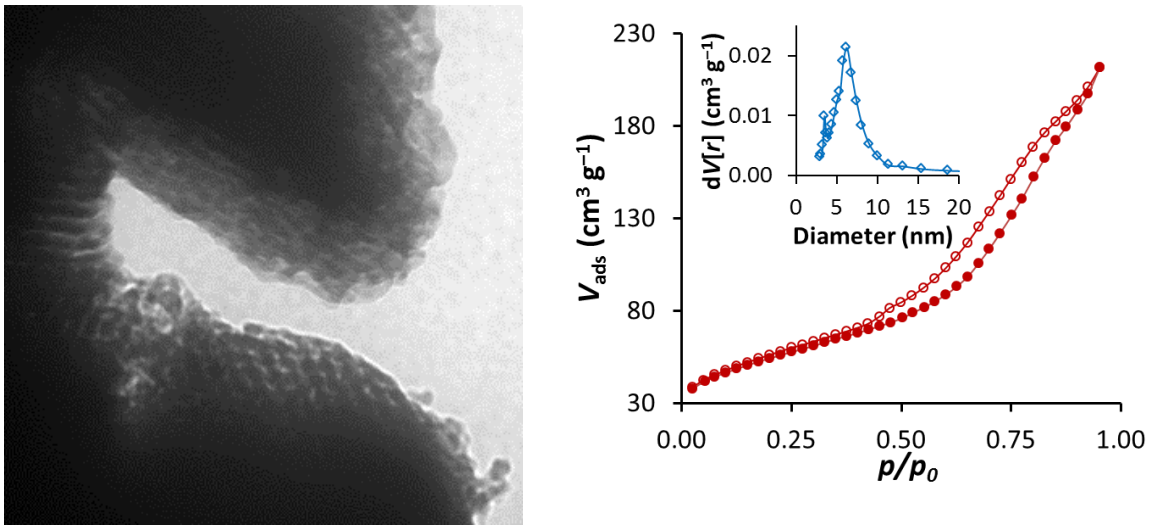

Figure 2.2. TEM image (left), N_2 sorption isotherm (right), and BJH plot (right, inset) for composite **2**.

metal nitrate precursors together with SBA-15 templates and then refluxing the mixture in *n*-hexanes. They obtained more effective precursor impregnation, presumably because apolar solvents cause the charged precursor ions to become partitioned inside the polar SBA-15 pores. We experimented with a number of apolar organic solvents and found that cyclohexene gave the most consistent results.

Under our conditions, after NaOH treatment, the cyclohexene impregnation method produced a dark brown composite material **2**, which appeared to have a denser structure than **1** (Figure 2). The composite **2** displayed only a slightly lower surface area than **1** (S^{BET} = 224 m^2 g^{-1}), but the desorption hysteresis was more slanted and skewed to lower pressure, which can be indicative of a broader range of pore sizes. The average BJH pore size was correspondingly much broader with a main peak *ca.* 6.3 nm accompanied by a second peak at 3.8 nm. This data indicates that that cyclohexene impregnation method gave a material in which the SC-SBA-15 templates were more effectively filled with the precursors, resulting in growth of thicker $LaMnO_3$ overlayers

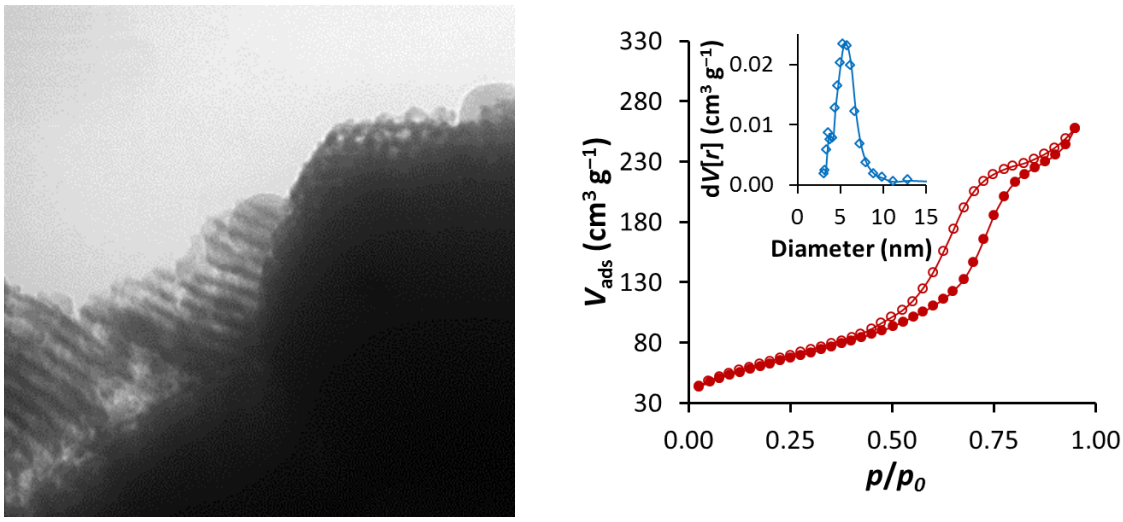

Figure 2.3. TEM image (left), N_2 sorption isotherm (right), and BJH plot (right, inset) for composite **3**.

and correspondingly smaller pores. The smaller peak in the BJH size distribution plot of **2** is well matched with what is expected for a CMK-3 type material, suggesting that a minority of the NaOH-etched **2** contained some free standing rod-like bundles, in addition to SiO_2-supported $LaMnO_3$.

A third hybrid approach was then stu died, in which the La^{3+} and Mn^{2+} nitrate precursors were dissolved in a minimal amount of water to promote wetting and even distribution in the SC-SBA-15 pores. The loaded templates were then refluxed in cyclohexene in an attempt to maximize precursor impregnation. After gelling, calcination and NaOH etching steps identical to the previous syntheses, a brown composite **3** was obtained. The resulting material appeared to have a highly-ordered SC-SBA-15-type structure, with a symmetric hysteresis closely related to SC-SBA-15 and the highest surface area of all three synthesis methods (S^{BET} = 296 m^2 g^{-1}). The average pore size in **3** was symmetrically distributed around 5.4 nm, which corresponds to uniform $LaMnO_3$ overgrowth inside the SBA-15 pores (Figure 2.3).

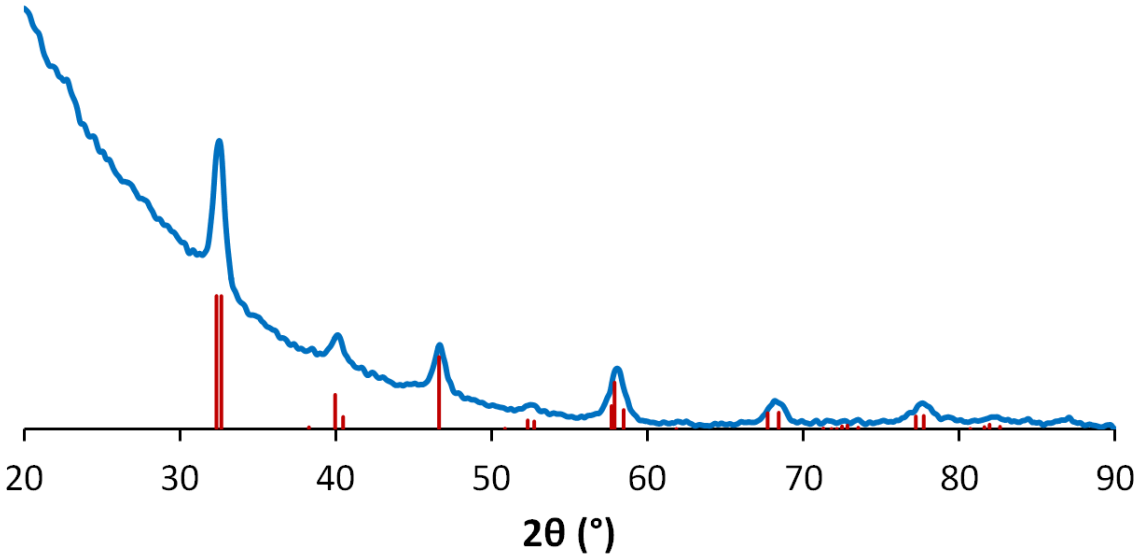

Figure 2.4. XRPD pattern of composite **3**.

Structural Characterization

Commonly, mesoporous materials such as SBA-15 give rather weak diffraction patterns, due to polycrystallinity and small ordered domains. In this work, the composites **1**–**3** did show bulk diffraction, even though the SC-SBA-15 precursor templates did not. Importantly, the PXRD patterns obtained were well indexed to the target $LaMnO_3$ phase[49] and did not show any evidence of other single metal oxide phases. Composite **3** showed the strongest diffraction (Figure 2.4); the large rise in the background centred below 20° 2θ is indicative of the amorphous silica phase remaining in the composite.

To further characterize the structure of the materials, EDX spectroscopy of 1–3 revealed the presence of O, Si, Mn and La in all particles (Figure 2.5). 2-D elemental mapping by HAADF-STEM was performed on selected honeycomb-like sections of the structurally most superior composite, 3 (Figure 2.6). As can be seen from the individual

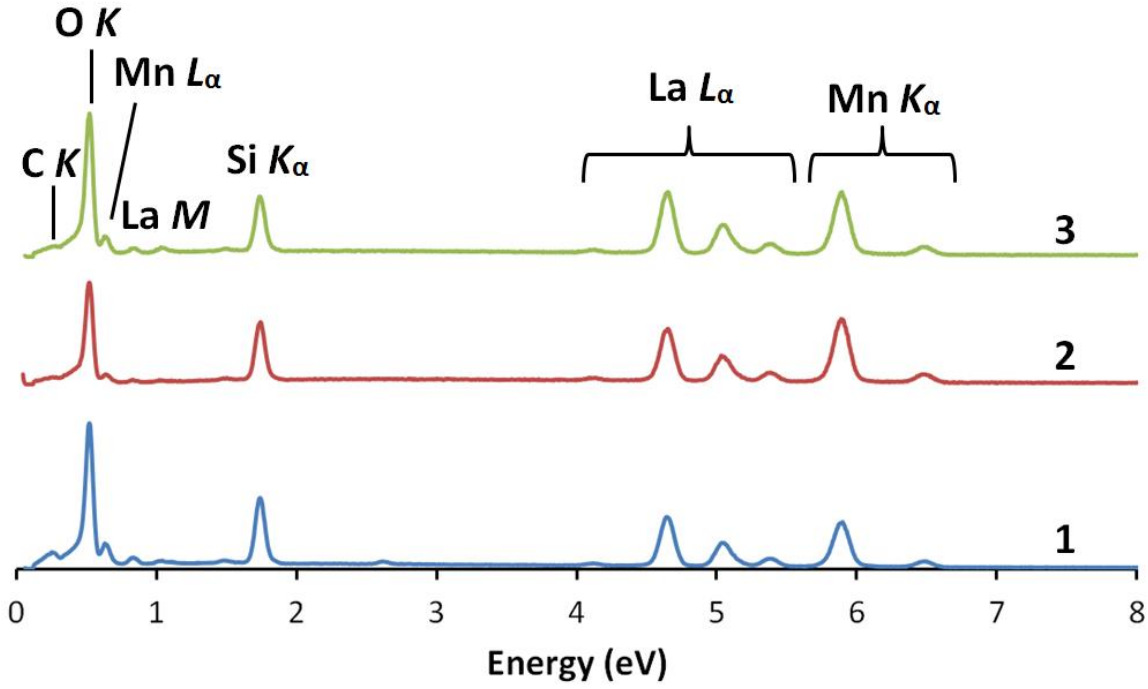

Figure 2.5. EDX spectra of composites **1**, **2**, and **3**.

maps for O, Si, Mn, and La, and the combined overlay (Figure 2.6, insets), all four elements were detected uniformly throughout the structure, indicating the presence of a mixed metal oxide on top of the SC-SBA-15 SiO_2.

XPS spectra were collected for each of the three composites (Figure 2.7). A 1:1 La:Mn ratio is expected for ordered $LaMnO_3$ that is not contaminated by other metal oxide phases. Composite **1** was found to have a slightly La-rich ratio (1.35) while **2** and **3** had La:Mn = 0.817 and 0.702, respectively. It is also possible to assess the distribution of Mn oxidation states in the composites, which is of interest to their application in pseudocapacitance. In general, only Mn^{3+} is expected in pure $LaMnO_3$, but Mn^{4+} is detected when excess oxide is intercalated, as a consequence of charge-balance. The Mn^{3+}:Mn^{4+} ratios for **1**–**3** were found to be 2.25, 1.05 and 1.61, respectively. These numbers indicate that reactions conducted in more apolar solvent environments resulted

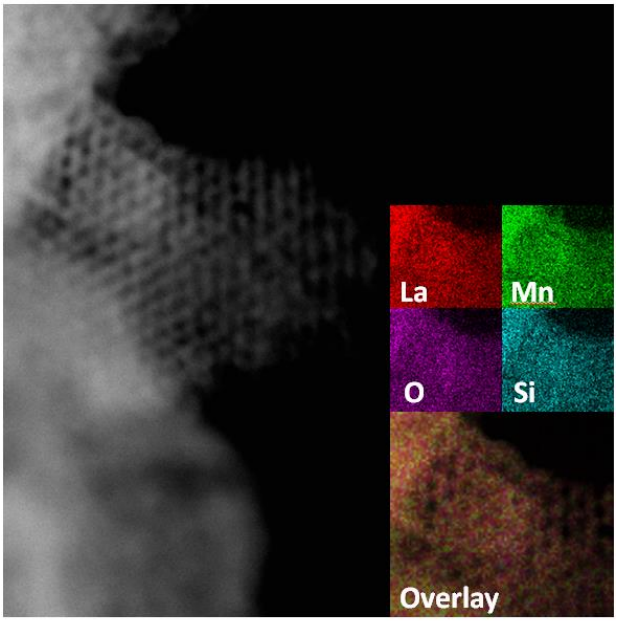

Figure 2.6. HAADF-STEM image and EDX maps (insets) of composite **3**.

in the formation of $LaMnO_3$ with a higher proportion of excess oxides. XPS also permits pseudo-quantitative assessment of the amount of SiO_2 retained in the composites. The highest percent of remaining silica by mass was found in **1** (20.4 wt%) while composites 2 and 3 had 15.6 and 18.5 wt% SiO_2, respectively.

While the XPS data suggests the formation of mixed metal oxides with variable Mn oxidation states, it should be noted that the desired $LaMnO_3$ perovskite phase is not always present at the very surface, as proven in this work by Raman spectroscopy, which is useful for selectively probing surface composition (Figure 8, left). Specifically, composite **2** showed Raman peaks characteristic of Mn_3O_4 (278 cm^{-1}, 344 cm^{-1}, A_{1g}: 636 cm^{-1}) rather than $LaMnO_3$.[50] The other materials (1 & 3) showed peaks associated with LaMnO3 (A_g: 497 cm^{-1}, A_g: 561 cm^{-1}, B_{1g}: 636 cm^{-1}), but the width of the peaks also suggests the materials may not be well ordered, i.e. made up of polycrystalline

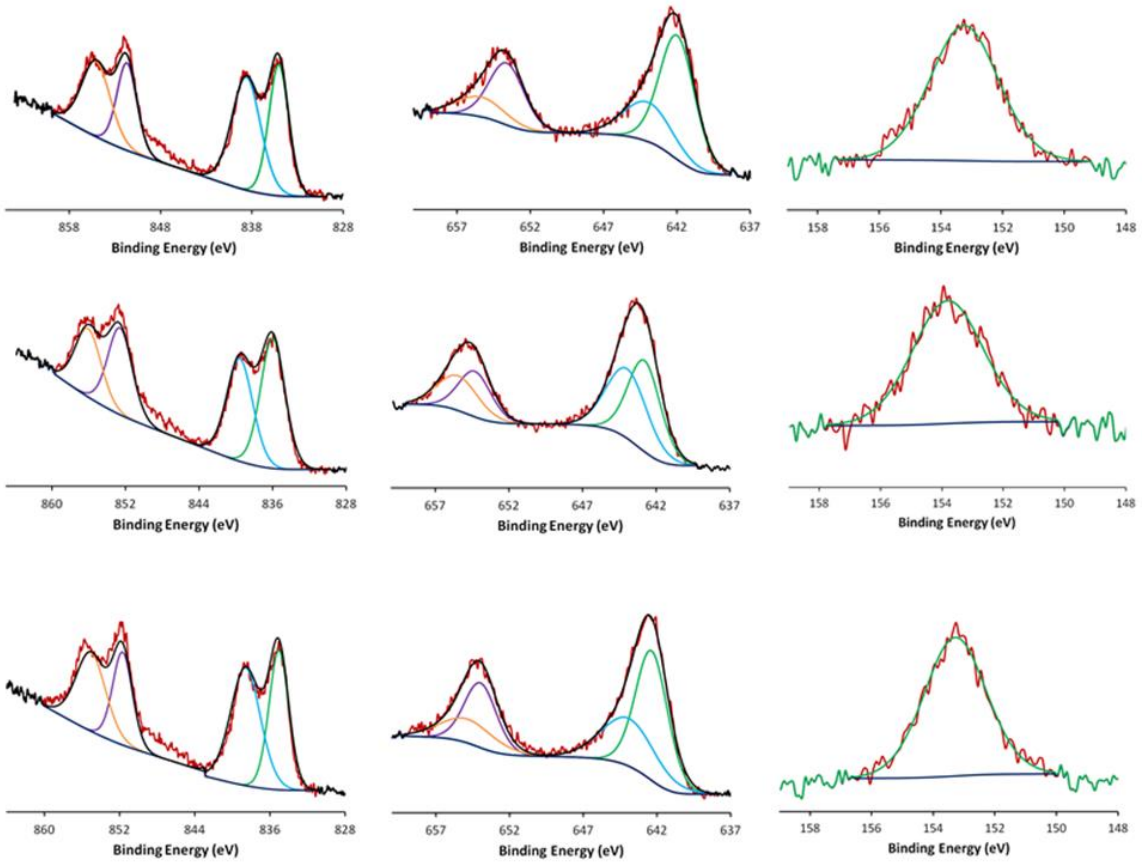

Figure 2.7. La 3d (Left), Mn 2p (center), and Si 2s (right) regions of the XPS spectra of Composites **1** (top), **2** (middle), and **3** (bottom)

domains; this is in direct agreement with the relatively weak diffraction observed by PXRD.[51]

Charge Storage Studies

Cyclic voltammetry was conducted in Ar-saturated 1 M KOH to test whether any of the three composites exhibited anion-based pseudocapacitance (Figure 8, right). All of the composites were mixed with Vulcan carbon to improve the conductivity of the

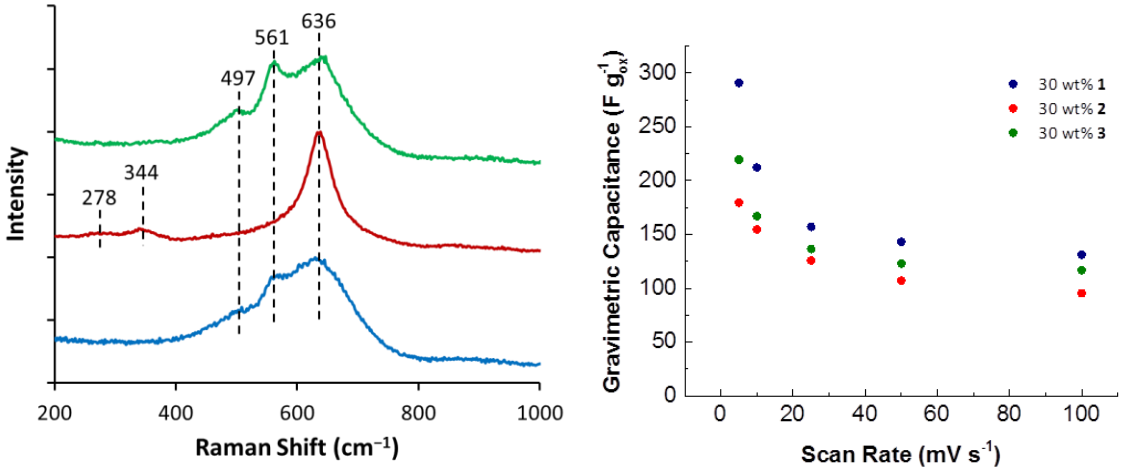

Figure 2.8. Raman spectra (left) and gravimetric capacitances (right) for composites **1**, **2**, and **3**.

electrodes; 30 wt% composite was found to give an optimal balance the conductivity of the carbon and the capacitive abilities of the composite materials. All three composites exhibited the same reversible redox wave at –0.3 V, which has previously been attributed to the conversion between Mn^{3+} and Mn^{4+} in pseudocapacitive studies of $LaMnO_3$; CVs of each material at all scan rates studied are included as Figure 11 at the end of the chapter.[19]

As shown in Figure 8, the pseudocapacitance of the **1**–**3** followed the trend **1** > **3** > **2** at every scan rate. This is contrary to what would be expected from the measured surface areas, which follow the trend **3** > **1** > **2**; therefore, surface area and transport distance into the material may not be the primary factors in determining specific capacitance in this system. Given the disordered nature of the surface, it is more likely that the most important factor is the quality of $LaMnO_3$ at (or near) the surfaces. This is supported by the predominance of Mn_3O_4 in the Raman spectrum of **2**, which consistently had the worst pseudocapacitance. The key difference between **1** and **3** may be the proportion of Mn^{3+} *versus* Mn^{4+}, which is key to the previously proposed mechanism for

pseudocapacitance in $LaMnO_3$, especially if the pre-existing Mn^{4+} is not part of a perovskite-type environment and therefore cannot be reversibly reduced to Mn3+ during cycling. The $LaMnO_3$-SiO_2 composite materials exhibit capacitances on par with MnO_2 (≈100 to 300 F g_{ox}^{-1}),[52-54] but are lower than the previously documented performance of $LaMnO_3$ nanoparticles (586 F g^{-1})[19] and ultra-thin MnO_2 materials (~700 F g^{-1}).[55] It is also possible that the morphology of the $LaMnO_3$-SiO_2 composites prepared in this work may not interface optimally with the conductive carbon additive, which would result in less efficient utilization of the active phase.

CONCLUSIONS

This work shows that a simple synthetic approach can be employed to prepare high surface area mesoporous $LaMnO_3$, supported on a sacrificial scaffold of SBA-15. Readily-available La^{3+} and Mn^{2+} nitrate precursors can be converted into the target perovskite phase using simple synthetic techniques; the polarity of the solvent used in the impregnation step was found to have an effect on the extent of precursor loading. It is not a necessity to employ more time-consuming, multi-step routes to prepare silica-free mesostructured metal oxides, if the desired properties of the composite material are not perturbed by the presence of SiO_2. In this instance, we have shown that $LaMnO_3$-SiO_2 composites act as effective pseudocapacitors.

EXPERIMENTAL DATA

General

$La(NO_3)_3 \cdot 6H_2O$ (Alfa Aesar; 99.999%), $Mn(NO_3)_2 \cdot xH_2O$ (Aldrich; 98%), Pluronic P-123 (Aldrich; M.W. = 5,800), tetraethoxysilane (Alfa Aesar; 98%), *n*-decane

(Alfa Aesar; ≥99%), ammonium fluoride (Alfa Aesar; 96%), sodium hydroxide (Aldrich; ≥98%), and hydrochloric acid (Fisher; 12 M) were used as received. All solvents were purchased at reagent grade and used without any further purification.

Gas Sorption Isotherms

Adsorption-desorption isotherms were recorded using a Quantachrome Autosorb-1 system, using ultra-high purity (≥99.995%) N_2 purchased from Praxair. Specific surface areas were calculated using the Brauner-Emmet-Teller (BET) method[47] using adsorption data points in range p/p_o = 0.05–0.30. Pore size distributions were calculated using the

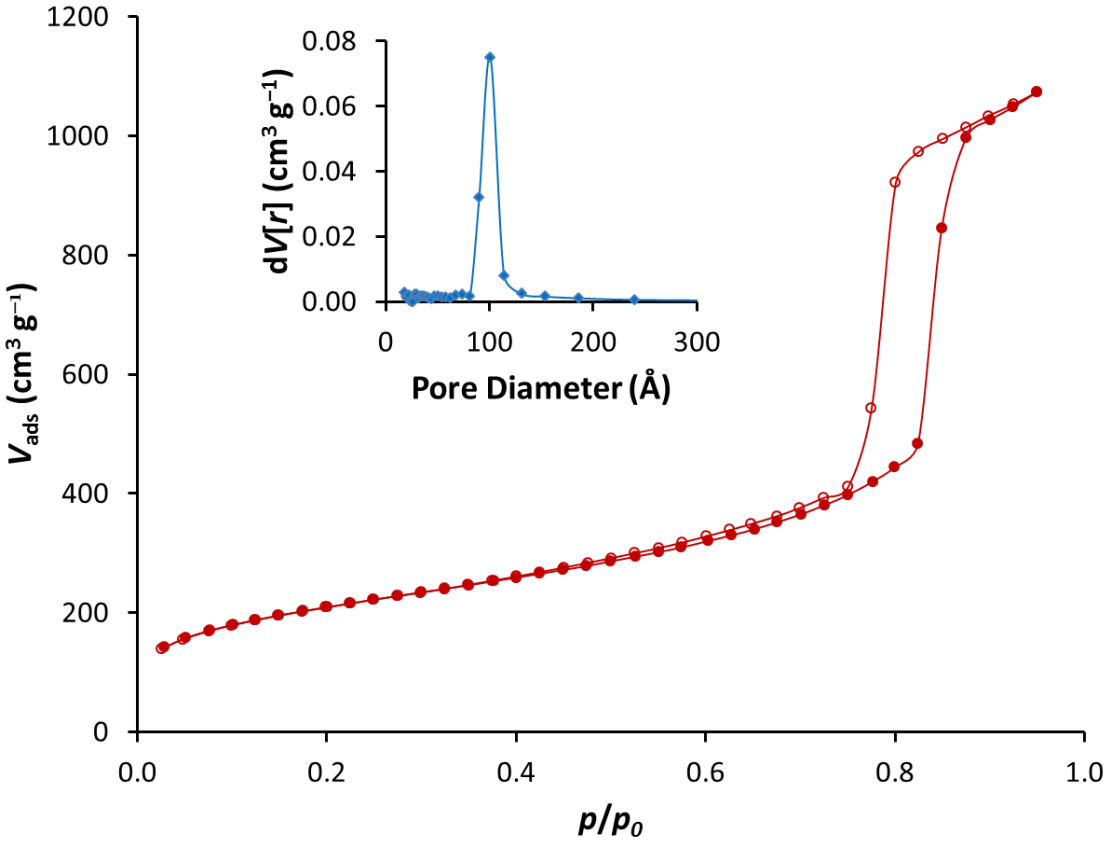

Figure 2.9. N_2 sorption isotherm and BJH plot (inset) for SC-SBA-15.

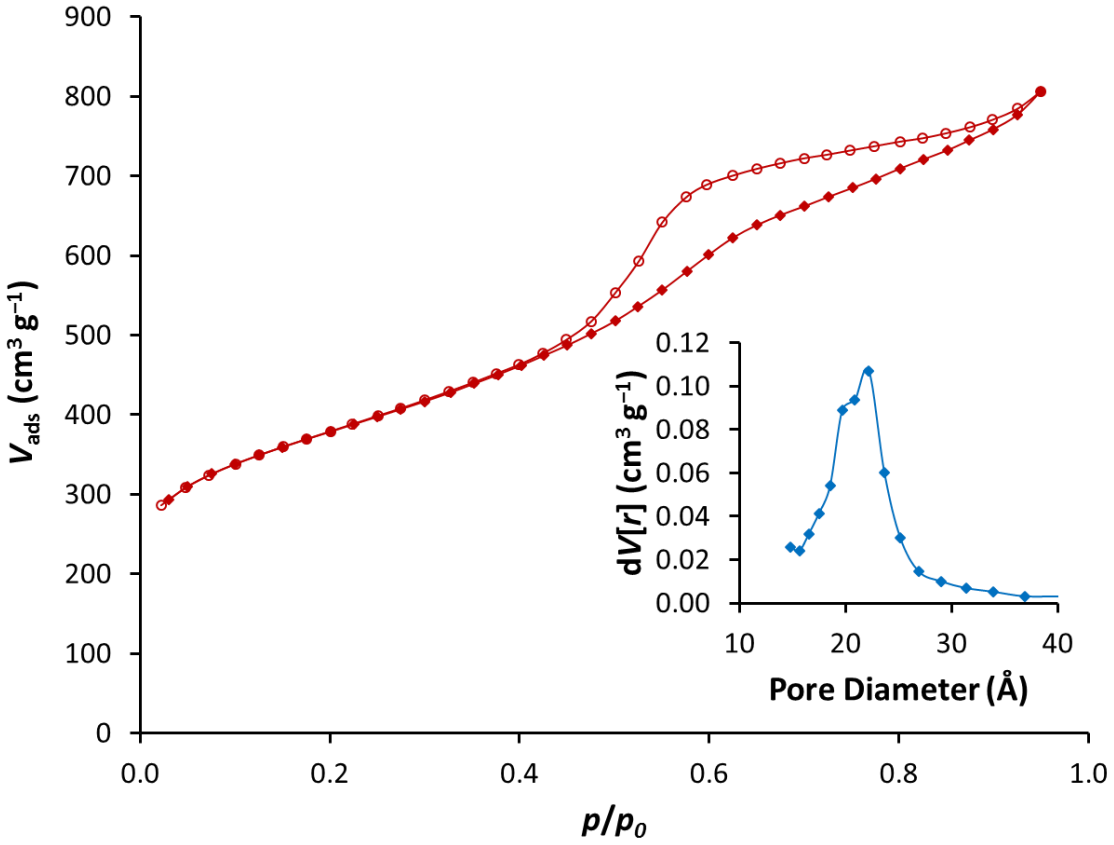

Figure 2.10. N_2 sorption isotherm and BJH plot (inset) for CMK-3.

Barrett-Joyner-Halenda (BJH)[46] equation using desorption data between p/p_o = 0.95–0.05.

Electron Microscopy and Energy-dispersive X-ray Spectroscopy

Transmission electron microscopy (TEM) images were obtained using an FEI Technai microscope with an operating potential of 80 kV. Samples were prepared by sonicating a few grains of the composite powder in ~3 cm^3 of acetone, then drop-casting the resulting suspension onto 200 mesh Cu/Formvar grids (Ted Pella, Inc.) and allowing the droplet to evaporate dry in air.

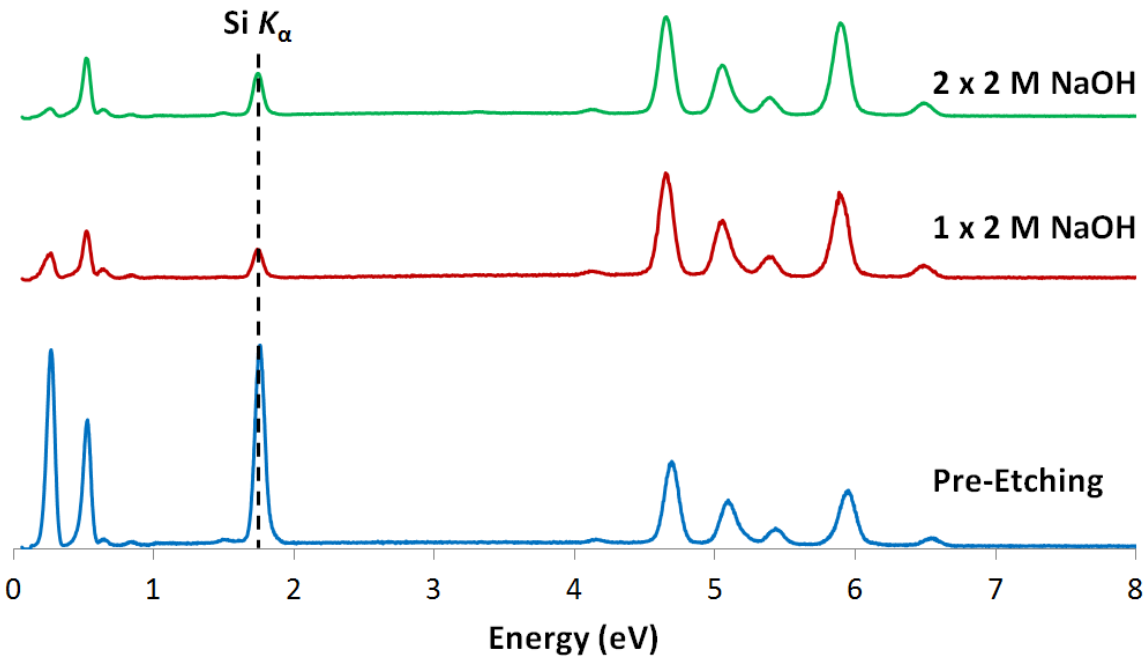

Figure 2.11. EDX spectra of pre-etched, singly-etched, and doubly-etched composites. While there is a significant reduction in the intensity of the Si peak from the pre-etched to the etched samples, there is no such reduction from the first etch to the second.

High-angle annular dark-field (HAADF) scanning transmission electron microscopy (STEM) and energy-dispersive X-ray spectroscopy (EDXS) mapping were performed using a JEOL 2010F TEM equipped with an Oxford X-MaxN 80TLE detector, and 200 kV electron source using a Schottky field-emission gun. EDXS analysis of the bulk materials was performed using a Hitachi S-5500 scanning electron microscope (SEM) operated at 20 kV. Samples used for STEM were the same as for TEM, above; SEM-based analyses were performed on composite powder affixed to the sample holder with graphite tape.

X-ray Powder Diffraction

Powder X-ray diffraction (PXRD) was performed using a Rigaku R-Axis Spider with a Cu K_α source (1.5418 Å) operating at 40 kV and 40 mA. Diffraction patterns were collected using a sample rotation speed of 10° s^{-1} and a step width of 0.01° 2θ.

X-ray Photoelectron Spectroscopy

X-ray photoelectron spectroscopy (XPS) spectra were collected using a Kratos Axis Ultra Photoelectron Spectrometer employing a monochromated Al K_α X-ray source (1486.5 eV) fitted with hybrid optics (*i.e.*, using both magnetic and electrostatic lenses) and a multi-channel plate coupled to a hemispherical photoelectron kinetic analyser. The samples used in the analyses were compacted to prevent dispersion of the powder under reduced pressure. Spectra were recorded with a pass energy of 20 eV, step size of 0.1eV and an aperture slot of 300x700 μm; dwell times varied depending on the signal strength from the element in question. To minimize sample charging and any resulting band distortion, a Kratos charge neutralizer (20 eV electrons) was used and the sample stage was left ungrounded. Casa XPS analysis software was used for peak deconvolution and the corrected peak areas were used in conjunction with the appropriate Kratos sensitivity factors for each element to determine the stoichiometry of the sample.

Raman Spectroscopy

Raman spectra were obtained from neat $LaMnO_3$ samples using a 50X objective on a confocal Raman microscope spectrophotometer (Renishaw InVia, controlled by Wire v.4.0 software). Typically, laser power reached 15 mW at full intensity. Measurements were taken at 5% total power using a 514.5 nm Ar^+ excitation source, by

restricting both the laser tube power and using neutral density filters within the instrument. All spectra were obtained using a 10 minute accumulation time in the region 200–1400 cm^{-1}. Data analysis was performed using OriginPro 9.0 to remove the fluorescence background from all samples.

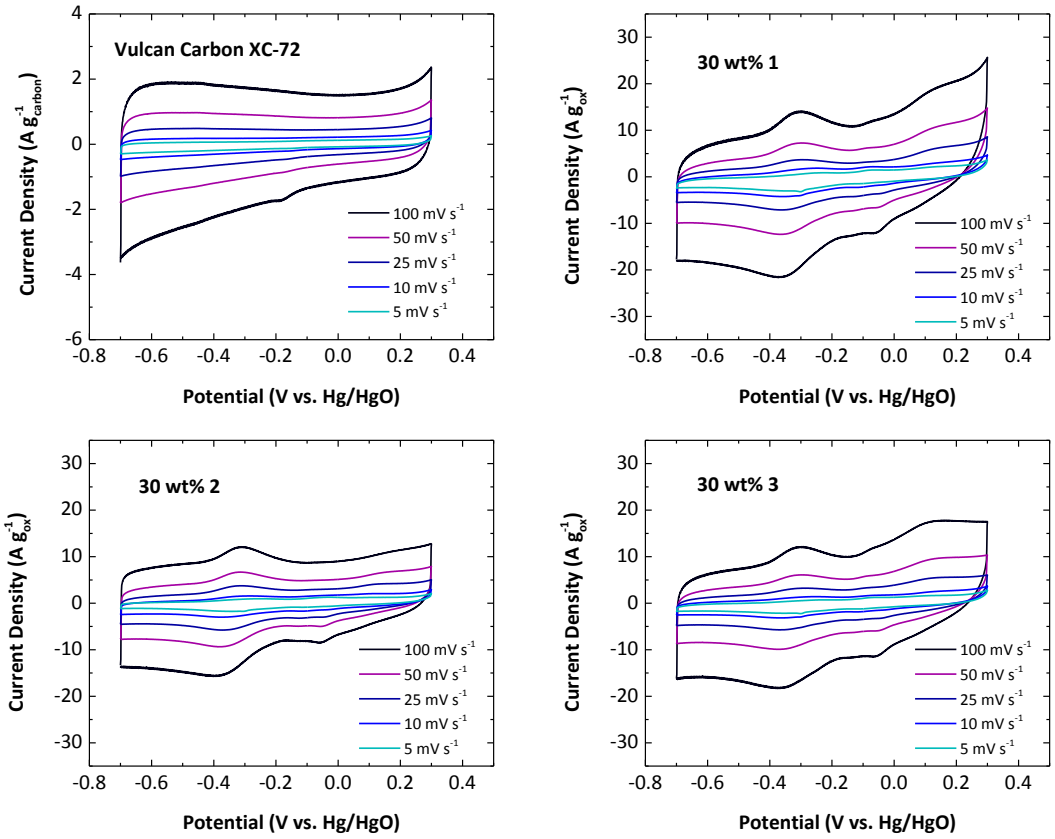

Figure 2.12. Cyclic voltammagrams of Vulcan Carbon (top left) and mixtures of Vulcan Carbon with 30 wt% of composites **1** (top right), **2** (bottom left), and **3** (bottom right) at scan rates ranging from 5 to 100 mV s^{-1}.

Electrochemical Testing

Each composite was mixed with Vulcan Carbon (XC-72, Cabot Corp.) by ball milling for 3 min (composite loading = 30 wt%). The solid mixtures were then dispersed in ethanol with 0.1 wt% Na-substituted Nafion at a concentration of 2 mg cm^{-3}. A total of 0.1 mg cm^{-2} of each mixture were then deposited on glassy carbon electrodes (Pine Instruments, 0.196 cm^2). The pseudocapacitance of the three composites were then tested by cyclic voltammetry in Ar-saturated KOH (1.0 M) at scan rates of 100, 50, 25, 10, and 5 mV s^{-1}. Capacitance values were calculated using eqn. [1] where C is the capacitance, m is the mass loading, v is the scan rate, V_A and V_C are the anodic and cathodic terminal potentials, respectively, and $i(V)$ is the current at potential V.

$$C = \frac{1}{mv|V_A - V_C|}\int_{V_C}^{V_A} i(V)dV \qquad [1]$$

Synthesis of SC-SBA-15

Short-channel SBA-15 was synthesized based on a previously published method.[56] Pluronic P-123 (2.40 g) was dissolved in HCl (85 cm^3, 1.03 M) in a 250 cm^3 Erlenmeyer flask under magnetic stirring. *n*-Decane (17.0 cm^3, 87.2 mmol) was then added slowly to serve as a swelling agent; the mixture was allowed to stir for 1-2 hours until the P-123 had completely emulsified the decane. Ammonium fluoride (28 mg, 0.76 mmol) was dissolved in the reaction mixture as a hydrolysis catalyst before tetraethoxysilane (5.6 cm^3, 25.2 mmol) was added drop-wise. The mixture was then stirred at 40 °C for 20 h, resulting in thickening of the opaque white slurry. The mixture was transferred to a 200 cm^3 Nalgene bottle which was sealed and heated at 100 °C for 48 h in a convection oven. The resulting white gel was recovered by vacuum filtration

and washed with copious amounts of H_2O and 95% ethanol. After drying in air, the solid was calcined in a ceramic crucible by heating at 550 ^{0}C for 5h (temperature ramp rate = 1.5 °C min^{-1}).

Synthesis of meso-$LaMnO_3$-SiO_2 by Ethanolic Water Impregnation (1)

$Mn(NO_3)_2{\cdot}xH_2O$ (0.8 mmol) and $La(NO_3)_3{\cdot}6H_2O$ (0.8 mmol) were dissolved together in an ethanol:water mixture (3:1, 5 cm^3). SC-SBA-15 templates (200 mg) in a 20 cm^3 scintillation vial were wetted with the manganese(II) nitrate solution by drop-wise addition until all of the powder was damp. The slurry was briefly sonicated (30–60 s, or until the sample appeared homogeneous) and the remainder of the precursor solution was then added. The vial was sonicated further to ensure full dispersion of the templates throughout the solution, then sealed with screw cap and the mixture was magnetically stirred overnight in an oil bath held at 40 °C. Next, the vial cap was loosened and the vial was moved to an oven at 80 °C for 24 h to aid in solvent evaporation. The resulting colourless gel was transferred to a ceramic crucible in a box furnace and heated to 700 °C (ramp rate = 1.0 °C min^{-1}) with continued heating for 5 h. After slow cooling (*ca.* 4 h), a 150 mg portion of the solid was stirred in a refluxing solution of NaOH in methanol:water (2.0 M, 2:1) for 3 h to etch away any exposed SiO_2. A fine brown solid of the target $LaMnO_3$-SiO_2 composite (**1**) was recovered by filtration and dried at 120 °C overnight in a convection oven.

Synthesis of meso-$LaMnO_3$-SiO_2 by Cyclohexene-assisted Impregnation (2)

$Mn(NO_3)_2{\cdot}xH_2O$ (0.95 mmol) and $La(NO_3)_3{\cdot}6H_2O$ (0.95 mmol) were ground together in an agate mortar with 200 mg of SC-SBA-15 and cyclohexene (10 cm^3) to

produce a colourless paste. The paste was transferred into a 100 cm^3 round-bottom flask charged with additional cyclohexene (30 cm^3) and the mixture was magnetically stirred at reflux overnight. The resulting brown solid was isolated by vacuum filtration and washed with excess hexanes before being moved to a ceramic crucible and heated in a furnace at 700 °C for 5 h (ramp rate = 1.0 °C min^{-1}). Accessible external SiO_2 was removed from the resulting $LaMnO_3$-SiO_2 product (**2**) as described for **1** above.

Synthesis of meso-$LaMnO_3$-SiO_2 by Wet Cyclohexene-assisted Impregnation (3)

To assess the effect of added water on the above synthesis, the Mn(II) precursors were dissolved in 0.3 cm^3 of deionised H_2O; this volume was chosen because it is approximately equal to the volume within the pores of 200 mg of the SC-SBA-15 hard templates. SC-SBA-15 (200 mg) was dispersed in cyclohexene (40 cm^3) with stirring, and 0.3 cm^3 of the swollen precursor solution was added drop-wise. The mixture was stirred at reflux overnight. The resulting solid was separated by filtration and washed with excess hexanes before heating in a furnace to 700 °C (ramp rate = 1.0 °C min^{-1}) and held for 5 h. The external SiO_2 was subsequently removed from the $LaMnO_3$-SiO_2 composite (**3**) as described for **1** and **2** above.

REFERENCES

1. B. E. Conway, *Electrochemical Supercapacitors: Scientific and Technological Applications*; Springer: Berlin, 2013.
2. A.S. Arico, P. Bruce, B. Scrosati, J. Tarascon, W. Van Schalkwijk, *Nature Mater.*, 2005, **4**, 366-377.
3. Mcdowall J., *Lithium battery technology* — Saft. Winter StatBatt Technical Sessions. StatBatt Technical Sessions. http://www.ewh.iee.org/cmte/PES-SBC, 2004.

4. P. Simon, Y. Gogotsi, *Nature Mater.*, **2008**, *7*, 845-854.

5. M. F. El-Kady, V. Strong, S. Dubin, R. B. Kaner, *Science*, **2012**, *335*, 1326-1330.

6. S. Chen, J. Zhu, X. Wu, Q. Han, X. Wang, *ACS Nano*, **2010**, *4*, 2822-2830.

7. G. Wang, L. Zhang, J. Zhang, *Chem. Soc. Rev.*, **2012**, *41*, 797-828.

8. J. Jiang, Y. Li, J. Liu, X. Huang, C. Yuan, X. W. Lou, *Adv. Mater.*, **2012**, *24*, 5166-5180.

9. X. Lang, A. Hirata, T. Fujita, M. Chen, *Nature Nanotechnol.*, **2011**, *6*, 232-236.

10. M. Zhi, C. Xiang, J. Li, M. Li, N. Wu, *Nanoscale*, **2013**, *5*, 72-88.

11. J. Liu, J. Jiang, C. Cheng, H. Li, J. Zhang, H. Gong, H. J. Fan, *Adv. Mater.*, **2011**, *23*, 2076-2081.

12. S. Bag, C. R. Raj, *J. Mater. Chem. A*, **2016**, *4*, 8384-8394.

13. B. E. Conway, V. Birss, J. Wojtowicz, *J. Power Sources*, **1997**, *66*, 1-14.

14. H. Y. Lee, J. B. Goodenough, *J. Solid State Chem.*, **1999**, *148*, 81-84.

15. S.-L. Kuo, N.-L. Wu, *J. Electrochem. Soc.*, **2006**, *153*, A1317-A1324.

16. J. P. Zheng, T. R. Jow, *J. Electrochem. Soc.*, **1995**, *142*, 6-8.

17. M. N. Patel, X. Wang, D. A. Slanac, D. A Ferrer, S. Dai, K. P. Johnston, K. J. Stevenson, *J. Mater. Chem.*, **2012**, *22*, 3160-3169.

18. H. Wang, H. S. Casalongue, Y. Liang, H. Dai, *J. Am. Chem. Soc.*, **2010**, *132*, 7472-7477.

19. J. T. Mefford, W. G. Hardin, S. Dai, K. P. Johnston and K. J. Stevenson, *Nature Mater.*, **2014**, *13*, 726–732.

20. M. A. Peña, J. L. G. Fierro, *Chem. Rev.*, **2001**, *101*, 1981-2018.

21. S. Jin, T. H. Tiefel, M. McCormack, R. A. Fastnacht, R. Ramesh, L. H. Chen, *Science*, **1994**, *264*, 413-415.

22. A. Sawa, *Mater. Today*, **2008**, *11*, 28-36.

23. L. G. Tejuca, J. L. G. Fierro, *Adv. Catal.*, **1989**, *36*, 237-328.

24. W. G. Hardin, D. A. Slanac, X. Wang, S. Dai, K. P. Johnston, K. J. Stevenson, *Phys. Chem. Lett.*, **2013**, *4*, 1254-1259.

25. W. G. Hardin, J. T. Mefford, D. A. Slanac, B. B. Patel, X. Wang, S. Dai, X. Zhao, R. S. Ruoff, K. P. Johnston, K. J. Stevenson, *Chem. Mater.*, **2014**, *26*, 3368-3376.

26. M. Nandi, K. Sarkar, M. Seikh, A. Bhaumik, *Micropor Mesopor. Mat.*, **2011**, *143*, 392-397.

27. Y. Wang, J. Ren, Y. Wang, F. Zhang, X. Liu, Y. Guo, G. Lu, *J. Phys. Chem. C*, **2008**, *112*, 15293-15298.

28. H. Arandiyan, H. Dai, J. Deng, Y. Liu, B. Bai, Y. Wang, X. Li, S. Xie, J. Li, *J. Catal.*, **2013**, *307*, 327-339.

29. D. Grosso, C. Boissière, B. Smarsly, T. Brezesinski, N. Pinna, P. A. Albouy, H. Amenitsch, M. Antonietti, C. Sanchez, *Nat. Mater.*, **2004**, *3*, 787-792.

30. Y. Liu, H. Dai, Y. Du, J. Deng, L. Zhang, Z. Zhao, C. T. Au, *J. Catal.*, **2012**, *287*, 149-160.

31. R. Chao, R. Munprom, R. Petrova, K. Gerdes, J. R. Kitchin, P. A. Salvador, *J. Am. Ceram. Soc.*, **2012**, *95*, 2339-2346.

32. H. Yang, D. Zhao, *J. Mater. Chem.*, **2005**, *15*, 1217-1231.

33. D. Gu, F. Schüth, *Chem. Soc. Rev.*, **2014**, *43*, 313-344.

34. M. M. Nair, F. Kleitz, S. Kaliaguine, *ChemCatChem*, **2012**, *4*, 387-394.

35. Y. Shi, B. Guo, S. A. Corr, Q. Shi, Y.-S. Hu, K R. Heier, L. Chen, R. Seshadri, G. D. Stucky, *Nano Lett.*, **2009**, *9*, 4215-4220.

36. V. K. Tomer, S. Duhan, *J. Mater. Chem. A*, **2016**, *4*, 1033-1043.

37. D. Zhao, J. Feng, Q. Huo, N. Melosh, G. H. Fredrickson, B. F. Chmelka, G. D. Stucky, *Science*, **1998**, *279*, 548-552.

38. S. Jun, S. H. Joo, R. Ryoo, M. Kruk, M. Jaroniec, Z. Liu, T. Ohsuna, O. Terasaki, *J. Am. Chem. Soc.*, **2000**, *122*, 10712-10713.

39. X. Lai, W. Li, W. Geng, J. Tu, J. Li, S. Qiu, *Angew. Chem. Int. Ed.*, **2006**, *46*, 738-741.

40. P. Półrolniczak, S. Kowalak, *J. Porous. Mat.*, **2010**, *18*, 703-706.

41. J. Roggenbuck, H. Schäfer, T. Tsoncheva, C. Minchev, J. Hanss, M. Tiemann, *Micropor. Mesopor. Mat.*, **2007**, *101*, 335-341.

42. X. Lai, H. Wang, D. Mao, N. Yang, J. Yao, C. Xing, D. Wang, X. Li, *Mater. Lett.*, **2008**, *62*, 3868-3871.

43. M. Sadakane, T. Horiuchi, N. Kato, C. Takahashi, W. Ueda, *Chem. Mater.*, **2007**, *19*, 5779-5785.

44. Y. Liu, H. Dai, Y. Du, J. Deng, L. Zhang, Z. Zhao, *Appl. Catal. B*, **2012**, *119*, 20-31.

45. M. M. Nair, F. Kleitz, S. Kaliaguine, *Chin. J. Catal.*, **2016**, *37*, 32-42.

46. E. P. Barrett, L. G. Joyner, P. P. Halenda, *J. Am. Chem. Soc.*, **1951**, *73*, 373-380.

47. S. Brunauer, P. H. Emmett, E. Teller, *J. Am. Chem. Soc.*, **1938**, *60*, 309-319.

48. H. Yen, Y. Seo, R. Guillet-Nicolas, S. Kaliaguine, F. Kleitz, *Chem. Commun.*, **2011**, *47*, 10473-10475.

49. Y.-Q. Quo, X.-H. Zhang, R. Waeppling, *J. Alloys Compds.*, **2000**, *306*, 133-140.

50. H. Xu, S. Xu, H. Wang, H. Yan, *J. Electrochem. Soc.*, **2005**, *152*, C803-C807.

51. N. N. Kovaleva, O. E. Kusmartseva, K. I. Kugel, A. A. Maksimov, D. Nuzhnyy, A. M. Balbashov, E. I. Demikhov, A. Dejneka, V. A. Trepakov, F. V. Kusmartsev, A. M. Stoneham, *J. Phys.: Condens. Matter*, **2013**, *25*, 155602.

52. C. Ramirez-Castro, O. Crosnier, L. Athouël, R. Retoux, D. Bélanger, T. Brousse, *J. Electrochem. Soc.*, **2015**, *162*, A5179-A5184.

53. Y. Chabre, J. Pannetier, *Progress in Solid State Chemistry*, **1995**, *23*, 1-130.

54. A. E. Fischer, K. A. Pettigrew, D. R. Rolison, R. M. Stroud, J. W. Long, *Nano Lett.*, **2007**, *7*, 281-286.

55. S.-C. Pang, M. A. Anderson, T. W. Chapman, *J. Electrochem. Soc.*, **2000**, *147*, 444-450.

56. H. Zhang, J. Sun, D. Ma, X. Bao, A. Klein-Hoffmann, G. Weinberg, D. Su, R. Schlögl, *J. Am. Chem. Soc.*, **2004**, *126*, 7440-7441.

Chapter Three: Rapidly Synthesized RhPd Alloy Nanoparticles as Hydrogenation Catalysts

RhPd alloy nanoparticles were synthesized by both microwave-assisted and oil bath heating with reaction times ranging from 30 seconds to 3 hours. These nanoparticles were found to be highly monodisperse by TEM, and were further characterized by XRPD, XPS, and EDS mapping to ensure the particles were random alloys. When applied to the gas-phase hydrogenation of cyclohexene, the RhPd particles made with the shortest reaction times were revealed to be the most catalytically active. DFT calculations were performed to model the hydrogenation of cyclohexene on pure Rh, pure Pd, and randomized 1:1 RhPd surfaces, and their respective catalytic activities were predicted based on a combination of their respective hydrogen and cyclohexene binding energies. The empirical results of the catalytic study proved to be in excellent agreement with the calculated prediction of catalytic activity increasing in the order Pd<RhPd<Rh.

INTRODUCTION

Noble metals are widely used as catalysts in a variety of key industrial processes. In particular, rhodium is used to catalyse the reduction of NO_x to N_2 and O_2, as well as the conversion of synthesis gas to more highly oxygenated hydrocarbons.[1,2] Palladium can perform carbon-carbon coupling reactions such as the Suzuki reaction as well as oxidations relevant to three-way catalytic converters.[1-3] Both rhodium and palladium are also capable hydrogenation catalysts.[4-7] However, because of their scarcity in the Earth's crust, these metals can be very expensive to procure.[8] While myriad efforts are underway to replace noble metals with cheaper transition metal catalysts, heterogeneous noble metal catalysts can be made more efficient by designing their structures to suit the

application at hand. Nanoparticle (NP) catalysts offer a significant improvement in atom efficiency over their bulk-metal counterparts because a far greater proportion of the metal atoms are at the surface of the material.[9] So-called "bottom-up" synthesis methods allow for a great deal of control over the size and shape of the resulting nanoparticles, which can impact the number and activity of the active sites.[10-13] In addition to the morphology of the particles, the composition of the material can be tailored to better suit the desired reaction. Alloying two or more metals has been shown to adjust the binding energy between the surface and the substrates, which can lead to an increase in reactivity even if one metal is unable to carry out the catalysis on its own (e.g. RhAu or RhAg).[14,15]

This study focuses on the synthesis of RhPd alloy nanoparticles and their activity toward cyclohexene hydrogenation. In the bulk phase, RhPd alloys can only be made by quenching mixtures of the two metals from over 1000 °C, and even those are only metastable and tend to segregate into the component metals upon such stimuli as the adsorption and desorption of hydrogen.[16-19] However, previous work by Kobayashi et al. has demonstrated that RhPd nanoparticles can be made at much lower temperatures (95 °C) and do not segregate upon the uptake or release of hydrogen.[20] The ability of the alloy to store hydride makes it an intriguing candidate for hydrogenation catalysis.

In addition to forming a RhPd alloy, this study also examined the importance of reaction time and heating mechanism. Once reduction of the precursor metal salts begins, the resulting metal atoms start to agglomerate and coalesce into nanoparticles; the nanoparticles continue to grow in this fashion until colloidal stability is achieved.[21] The chosen heating method can play an important part in this process; microwave heating (MwH) has previously been shown to increase reaction rates, as well as produce more monodisperse and crystalline nanoparticles compared to conventional, oil-bath heating

under otherwise comparable conditions.[22] In this study, we explore the effects these factors have on the structure and catalytic activity of RhPd nanoparticles.

RESULTS AND DISCUSSION

Synthesis and Structure Analysis

Transmission electron microscope (TEM) imaging was used to study the morphology of the synthesized RhPd particles. For each set of conditions, a total of at least 300 particles from images of two or more positions on the grid were measured to analyze the distribution of particle diameters. Representative TEM images and particle size distributions for the nanoparticles synthesized under microwave irradiation are

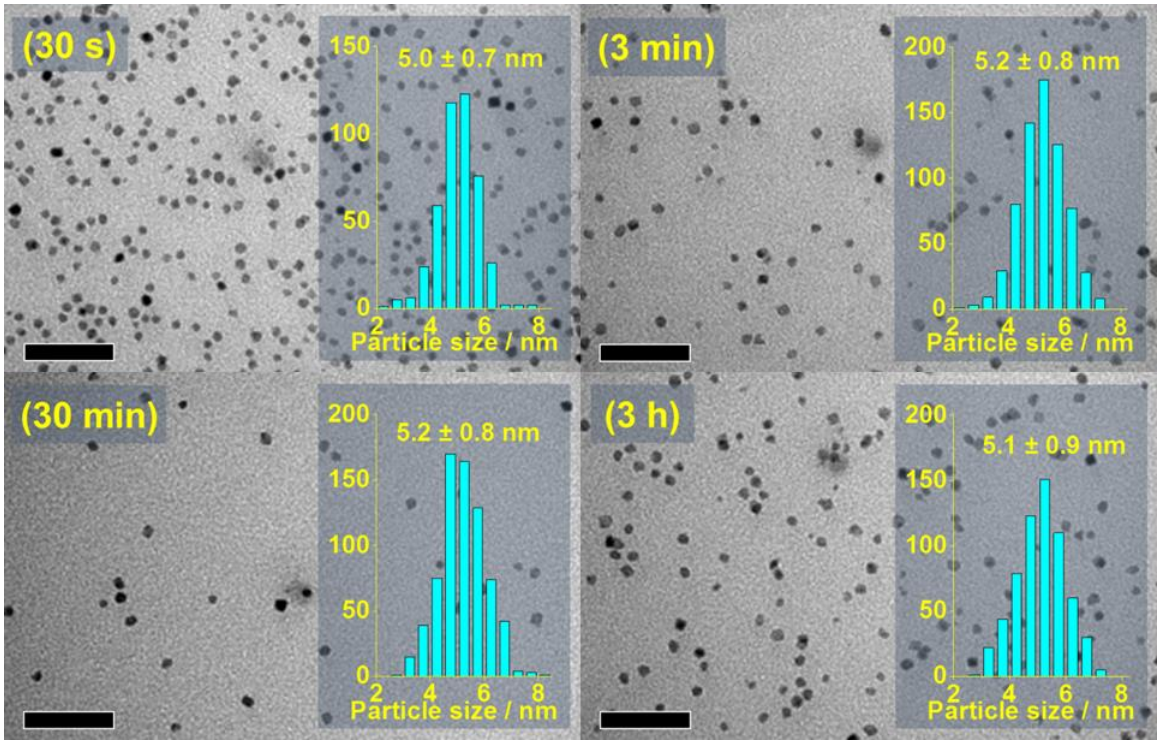

Figure 3.1. TEM images and size distributions of RhPd nanoparticles made with microwave heating and different reaction times.

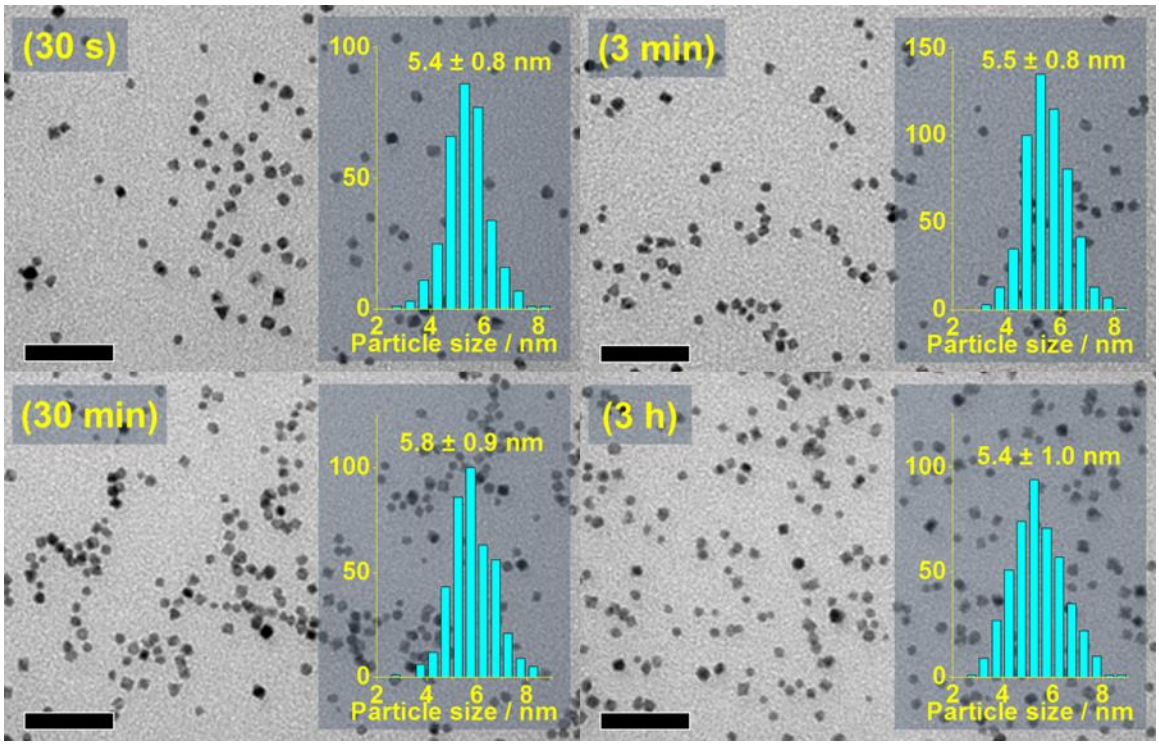

Figure 3.2. TEM images and size distributions of RhPd nanoparticles made with conventional oil bath heating and different reaction times.

presented in Figure 3.1. In each case, most particles resembled spheres or cubes, and the diameters exhibited relatively narrow normal distributions. Nanoparticles made with reaction times ranging from 30 s to 3 h all had very similar mean diameters slightly above 5 nm, with standard deviations under 1 nm. This level of monodispersity is consistent with previous syntheses of noble metal nanoparticles under microwave irradiation.[22] The lack of significant growth is unexpected for PVP-capped, Rh-containing particles made in ethylene glycol, but is consistent with observations of Pd nanoparticles made under similar conditions by Xiong, *et al.*[22,23] RhPd nanoparticles synthesized using conventional heating were larger on average than their microwave-heated counterparts at each reaction time, though the differences were well within the respective standard

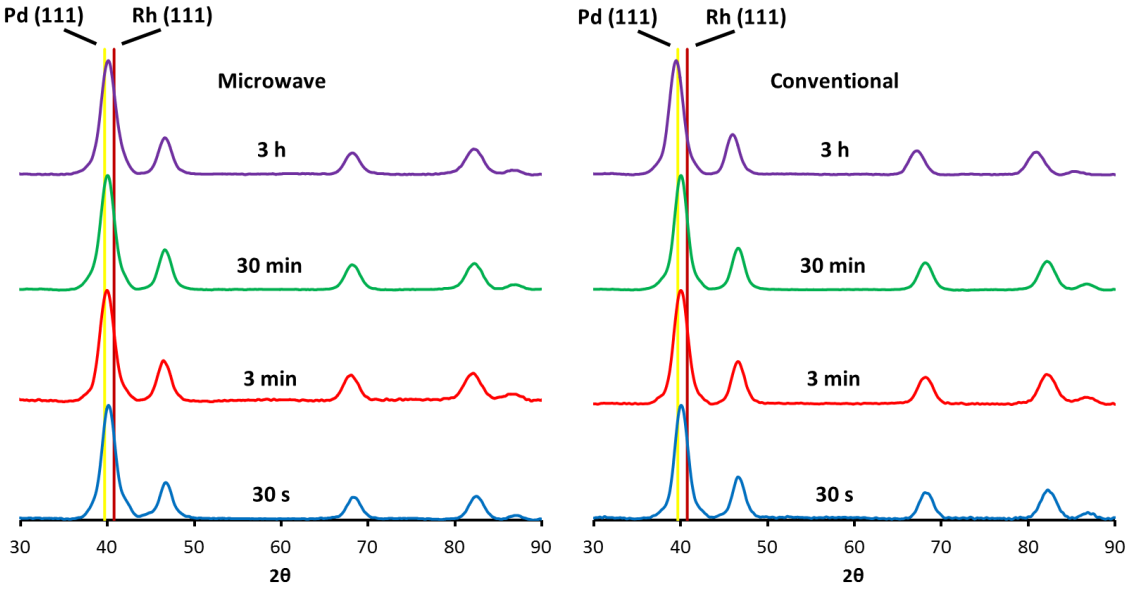

Figure 3.3. X-ray powder diffraction patterns of RhPd nanoparticles made by microwave (left) and conventional (right) heating at each tested reaction time. Lines corresponding to the (111) peaks of pure Rh and Pd particles are included for comparison.

deviations. The distributions of diameters are slightly wider as well, but still approximate a normal curve (Figure 3.2).

X-ray powder diffraction (XRPD) was used to analyse the crystal structure of the RhPd nanoparticles. Particles from all eight reaction conditions produced spectra matching a basic fcc lattice, and the peaks from seven were positioned in between the corresponding reference peaks for pure rhodium and palladium, as would be predicted from Vegard's law (Figure 3.3). The exception was the conventional reaction heated for the longest time, suggesting that under those conditions the dominant diffraction was from a Pd-rich core and that Rh had been segregated toward the surface. In addition, applying the Scherrer equation to the 111 peak in each spectrum and using a shape factor of 0.9 results in crystallite size estimates that are consistently smaller than the measured

average diameters by about 0.5 to 1 nm (Table 3.2, at the end of this chapter). The 30 s samples for each heating method had the smallest discrepancies between the Scherrer estimate and the measured average, and the discrepancies were larger for the conventionally heated samples than the microwave heated ones.

To further confirm the elemental makeup of the synthesized nanoparticles, the RhPd alloys were studied by XPS, ICP-OES, and EDS. XPS showed the MwH NP samples contained both metals in comparable amounts, often with a slight excess of Pd (Figure 3.4, Table 3.1). The proportion of Rh (I) was lowest in the sample heated for only 30 s (25%), and increased to *ca.* 56% after 3 h. In contrast, the 30 s sample had one of the highest proportions of Pd (II) (66%), and that value decreased over time to 45% after 3 h (Table 3.1); this may be indicative of the surface becoming enriched in rhodium at longer reaction times. The elemental compositions provided by ICP-OES were generally in good agreement with their XPS counterparts and also indicated a small excess of Pd in most cases (Table 3.3, at the end of this chapter). The discrepancies between these two techniques likely result from the ability of ICP-OES to analyze the NPs in their entirety, whereas XPS can only interrogate the top *ca*. 10 nm of the NP-PVP film. This difference can cause the XPS results to favor the species found at the surface of the particles. To provide further evidence that both metals were present in the same nanoparticles, EDS mapping was performed on samples of MwH 30 s and 3 h NPs while investigating them by HAADF-STEM (Figure 3.5). Both rhodium and palladium signals were detected in every particle tested, and both were distributed throughout each particle. This was especially true in the map of the 30 s NPs, which shows even, random distribution throughout the entire particle. The map of the 3 h NPs suggests the Rh present has moved preferentially toward the surface of the particle, as suggested by XPS, but Rh still appears distributed broadly enough to be considered an alloy.

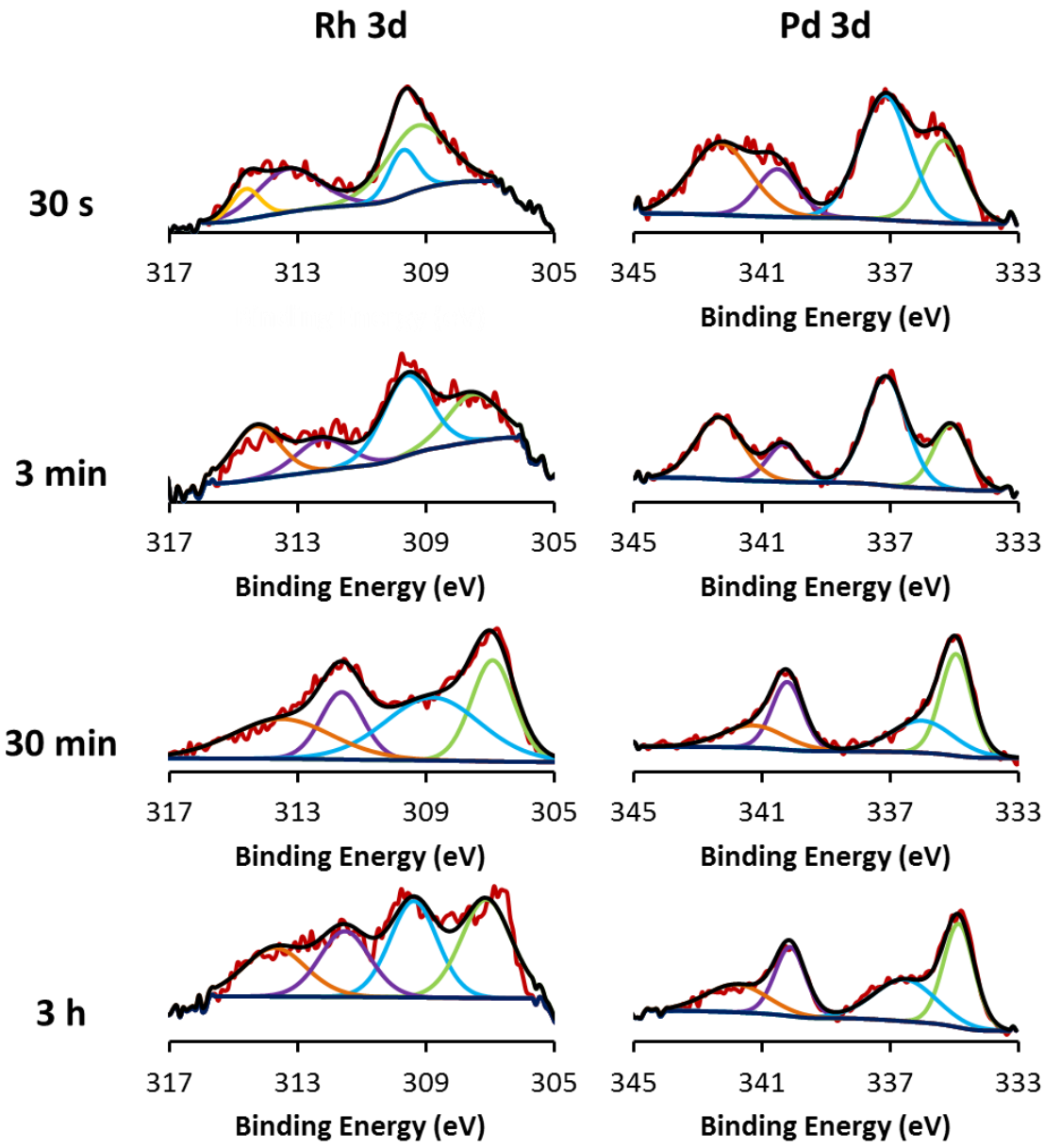

Figure 3.4. Rh 3d (left) and Pd 3d (right) portions of the XPS spectra of RhPd nanoparticles synthesized by microwave heating using each reaction time tested.

	Reaction Time			
	30 s	3 min	30 min	3 h
Rh %	**42.82%**	**41.18%**	**45.28%**	**52.48%**
Rh (0)	75.45%	39.23%	42.33%	43.68%
Rh (I)	24.55%	60.77%	57.67%	56.32%
Pd %	**57.18%**	**58.82%**	**54.72%**	**47.52%**
Pd (0)	33.90%	32.00%	60.66%	55.25%
Pd (II)	66.10%	68.00%	39.34%	44.75%

Table 3.1. Percentages of Rh and Pd, as well as each individual oxidation state within microwave-synthesized RhPd nanoparticles made with various reaction times.

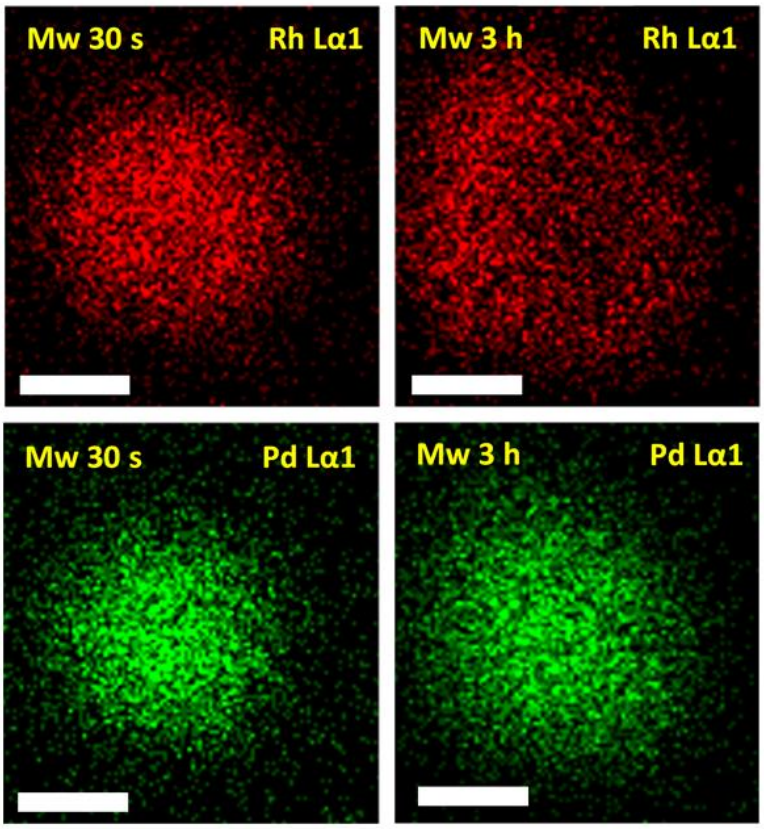

Figure 3.5. EDX maps of the distributions of Rh (top) and Pd (bottom) within representative particles synthesized using 30 s (left) and 3 h (right) of microwave heating.

Hydrogenation Catalysis

The hydrogenation of cyclohexene was used as a test reaction to explore the catalytic activity of the RhPd nanoparticles. The nanoparticles were supported on amorphous silica produced in-house, and the resulting composite was mixed thoroughly with sand before loading the catalyst material into a fixed-bed reactor setup (see Scheme 3.2 at the end of this chapter). Because early results indicated that RhPd particles were vulnerable to poisoning by atmospheric O_2 under reaction conditions, care was taken to degas the catalysis line and the cyclohexene bubbler before activating the catalyst under flowing H_2/He for 30 minutes. After activation, the catalyst was closed off and cyclohexene was allowed to blow through the rest of the line for 25 minutes to ensure consistency in the cyclohexene flow and complete sparging of the cyclohexene supply. Having done this, the catalyst was opened to the flow of cyclohexene, and the reaction was allowed to continue for 6 h.

Key catalysis results at 25 °C are presented in Figure 3.6; for full results from both the MwH and CvH NPs, see Figure 3.8 at the end of this chapter. After 5 h, the MwH 30 s RhPd NPs retained a turnover frequency (TOF) of 8.5 s^{-1}, slightly above that of the MwH 3 h RhPd NPs (8.2 s^{-1}). Both sets of particles show remarkably stable activity under reaction conditions, retaining *ca*. 73% of their initial TOF. The corresponding conventionally heated RhPd NPs both displayed higher initial TOFs, but they decayed much more rapidly, falling below their MwH counterparts in less than 150 min. When compared with MwH NPs of the individual metals, The MwH RhPd NPs were more active than pure Pd (TOF = 7.1 s^{-1} after 5 h), but not as active as pure Rh (TOF = 13.6 s^{-1} after 5 h). However, the pure Rh NPs did not exhibit a TOF that was nearly as stable as the RhPd or pure Pd NPs; only 41% of the Rh NPs original TOF

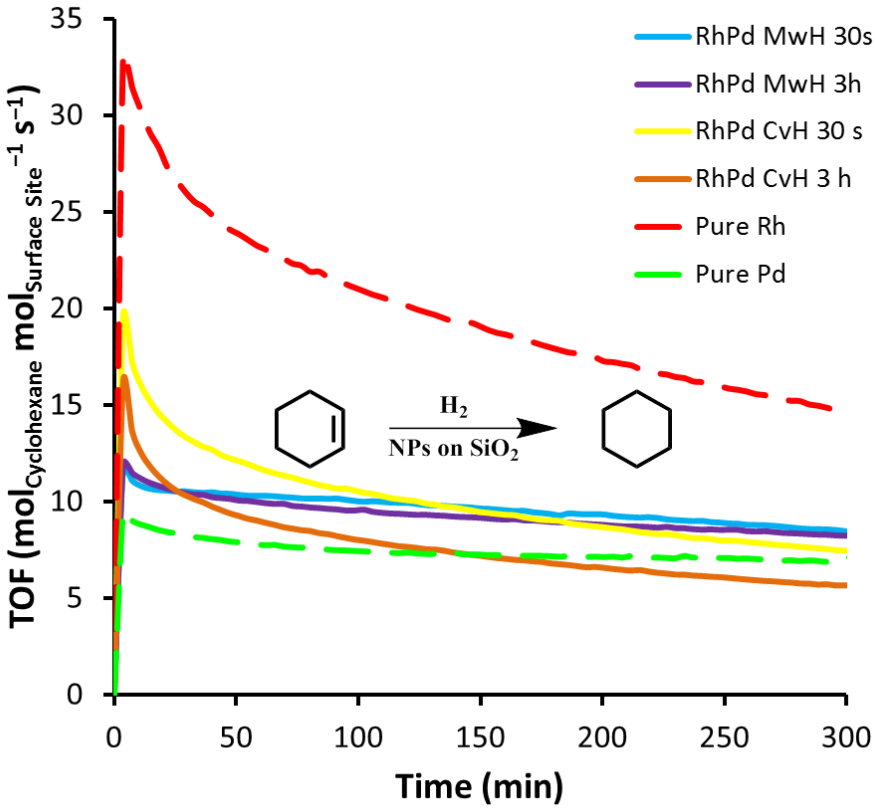

Figure 3.6. Key hydrogenation catalysis results featuring RhPd nanoparticles synthesized by several different means, as well as microwave-synthesized Rh and Pd nanoparticles.

remains after 5 h. Rhodium catalysts are known to be far more vulnerable to deactivation by coking than palladium ones. It therefore seems possible that the presence of Pd in the alloy NPs protects them from deactivation to some extent. However, this only seems to be the case with microwave-heated samples, and even then intermediate reaction times do not produce this effect. No agglomeration of the particles was observed by TEM for any of the catalysts after 6 h of use (see Figure 3.9 at the end of this chapter).

The recyclabilities of the two RhPd catalysts on opposite ends of the reaction time range were also tested (Table 3.4, at the end of this chapter). Although the 30 s particles lost more of their reactivity in percentage terms from cycle to cycle, they were

consistently more reactive than the 3 h particles over the course of the study. Variable-temperature studies were also conducted to enable the calculation of activation energies; the Arrhenius plots for the various catalysts are presented in Figures 3.10 and 3.11 at the end of this chapter. Although there is some fluctuation in the calculated activation energies (Table 3.5, at the end of this chapter), the activation energies for the microwave-heated catalysts tend to be slightly lower than their conventionally heated counterparts, and the various alloy catalysts have activation energies between those of the two pure metals.

DFT Calculations

Previously, we reported that H and cyclohexene (CHE) binding energies can be used as descriptors to evaluate the catalytic performance of CHE hydrogenation catalysts.[14] A volcano-shaped activity plot shows that both the H binding energies of Rh(111) and Pd(111) are too strong to reach the highest TOF activity.[14,24] To understand the experimental results of this study, DFT calculations were performed to calculate the H and CHE binding energies on Rh(111), Pd(111) and RhPd random alloy surfaces. Details of the calculations are provided at the end of the chapter. Figure 4a shows the calculated average H binding energies at four triatomic ensembles (Rh_3, Rh_2Pd_1, Rh_1Pd_2 and Pd_3) on $Rh_{0.50}Pd_{0.50}$, while Figure 4b shows the calculated average CHE binding energies at five additional binding sites (Rh_1, Rh_2, RhPd, Pd_1 and Pd_2). The results indicate that the binding of CHE is strongest to Rh, weakest to Pd, and changes roughly linearly with binding site composition in the $Rh_{0.50}Pd_{0.50}$ alloy. The binding of H is somewhat more complicated; it is stronger on the Pd(111) surface than Rh(111). In the $Rh_{0.50}Pd_{0.50}$ alloy, however, H binding is stronger to Rh atoms and weaker to Pd. This

somewhat counter-intuitive result can be explained by the electronic or ligand effect where Pd atoms around the Rh-rich sites increase H binding and Rh atoms around the Pd-rich sites decrease binding as a result of charge transfer from Rh to Pd in the alloy.[25] Additional calculations demonstrating the correlation between binding site composition and H binding energy are shown in Figure 3.12 at the end of this chapter.

The H binding energy of Rh is closer to the top of the volcano than Pd, as shown in Figure 3.7 (bottom).[14,24] While Pd has a more suitable binding for CHE, the overall predicted hydrogenation activity is lower than Rh. The average binding energy of H and CHE on the $Rh_{0.50}Pd_{0.50}$ alloy is found to be intermediate between Rh and Pd, as one would expect from the trends in Figure 3.7 (middle). These theoretical results are consistent with the experiments showing that the CHE hydrogenation activity are in the order Rh> $Rh_{0.50}Pd_{0.50}$ > Pd.

CONCLUSIONS

PVP-capped RhPd alloy nanoparticles can be prepared by either microwave-assisted or conventional oil bath heating using ethylene glycol as both the solvent and the reducing agent. These particles were shown to catalyse the gas phase hydrogenation of cyclohexene, and nanoparticles made with short reaction times were at least as effective as those heated for longer times. The catalytic activity of the RhPd NPs as compared to Rh and Pd NPs is in good agreement with DFT calculations based on hydrogen and cyclohexene binding energies, further demonstrating the utility of this approach to the study of nanoparticle catalysts.

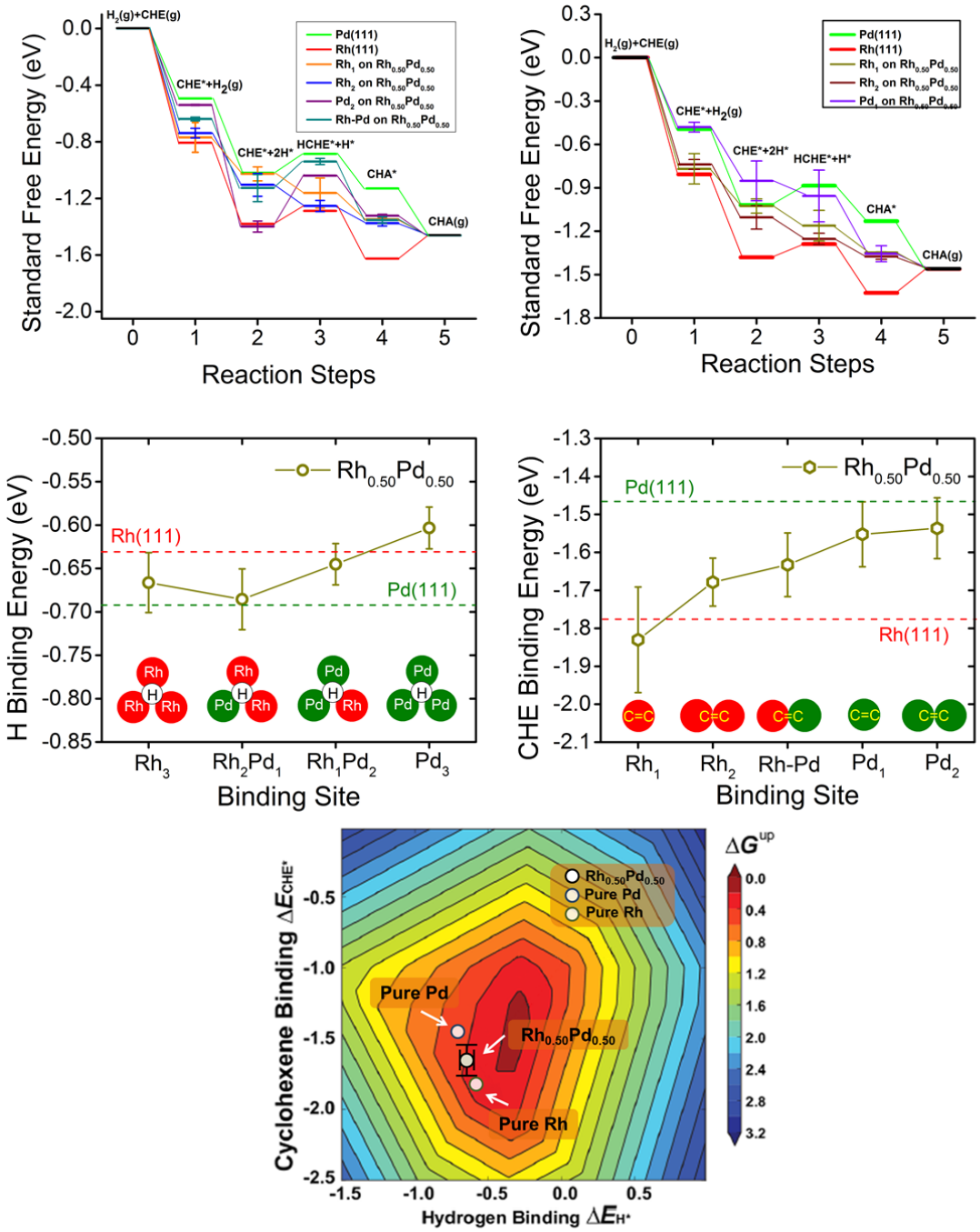

Figure 3.7. Results of DFT calculations: variation of the energetic pathway of hydrogenation by cyclohexene binding site (top), differences in H and cyclohexene binding energies by binding site (middle left and right, respectively), and a volcano plot showing the predicted range of RhPd reactivity given the above calculations.

EXPERIMENTAL DATA

General

All of the RhPd, Rh, and Pd NPs were synthesized using the polyol method, utilizing $RhCl_3 \cdot xH_2O$ (Strem Chemicals, 38-41% Rh) and K_2PdCl_4 (Strem Chemicals, 99%) as the metal precursors, poly(vinylpyrrolidone) (PVP; Alfa Aesar, MW = 58K, ~18 mol monomer/mol metal) as the capping agent, and ethylene glycol (Fischer Scientific, 99.8%) as the solvent and reducing agent. Cyclohexene (Acros Organics, 99%) was used in the catalytic studies. Hydrogen and helium gases were obtained in 99.9995% purity from Praxair. These chemicals and all other solvents (analytical grade) were used as received.

Microwave Synthesis Setup

Microwave-heated reactions were carried out in a MARS 5 microwave reactor (CEM Corp.) with 1600 W (2.45 GHz) maximum available power. A RTP-300+ fiber-optic temperature sensor was submerged in 17.5 mL ethylene glycol to monitor and control the temperature within the reaction chamber. Due to evaporation at longer reaction times, the temperature standard was kept in a 50 mL round-bottom flask connected to a reflux condenser. A large beaker was used to contain the flask, and a taut string was run in through the hole in the top of the reactor to stabilize the top of the condenser. An external temperature standard was used rather than putting the probe directly into the reaction solution because of the risk of arcing presented by accumulation of solid metal on the sensor. To prevent excessive evaporation during longer reaction times, the ethylene glycol standard was put in a round-bottom flask connected to a reflux condenser instead of a beaker. The reaction itself was performed in a 50 mL round-

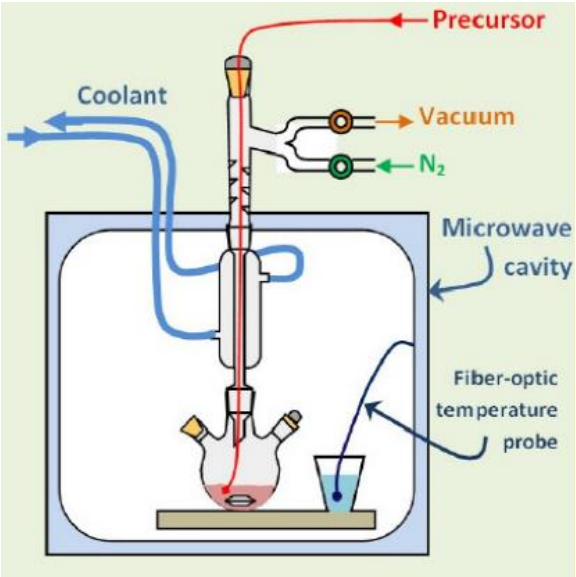

Scheme 3.1. Diagram of the setup used for the microwave-heated nanoparticle syntheses.

bottom flask attached to a water-cooled reflux condenser. The flask initially contained a solution of 200 mg PVP in 15 mL ethylene glycol, which was heated with magnetic stirring to 165 °C over the course of 6 min. The metal precursors were dissolved separately in 2.5 mL of ethylene glycol, and the resulting solution was loaded into a 10 mL syringe mounted in an Aladdin programmable syringe pump (WPI, Inc.). Teflon tubing was run from the needle of the syringe through a hole in the top of the microwave reactor and down through the condenser to the reaction flask, with its lower end approximately 1 cm above the level of the solution.

Electron Microscopy

Transmission electron microscopy (TEM) images were produced using an FEI Technai microscope with an operating potential of 80 kV. Samples were prepared by drop-casting a dilute solution of nanoparticles in ethanol onto 200 mesh Cu/Formvar

grids (Ted Pella, Inc.) and allowing the grid to air dry. The diameters of the nanoparticles were found by using the line tool in Image-J (http://rsbweb.nih.gov/ij) to measure the shortest distance across each particle that included the center of the particle. Over 300 particles across at least two images from different grid coordinates were measured for each set of reaction conditions. High-resolution TEM (HR-TEM) images and energy-dispersive X-ray spectroscopy (EDX) lines scans were obtained using a JEOL 2010F transmission electron microscope operating at 200 keV with a field-emission gun with 0.19 nm point-to-point resolution.

X-ray Powder Diffraction

X-ray powder diffraction was performed using a Rigaku R-Axis Spider with a Cu Kα source (1.5418 Å) operating at 40 kV and 40 mA. X-ray spectra were collected using a sample rotation speed of 10° s^{-1} and a step width of 0.01° 2θ. Scherrer Equation:

$$\tau = \frac{K\lambda}{\beta \cos\theta}$$

where τ is the mean crystallite diameter, K is the shape factor; λ is the X-ray wavelength, β is the peak width at half the maximum intensity of the 111 peak (FWHM), expressed in radians, and θ is the Bragg angle of the peak. The calculations for this work used the typical assumption of 0.9 for the K factor. Cu Kα radiation has a wavelength of 0.15418 nm.

	Microwave		Conventional	
Rxn Time	τ (nm)	d_{TEM} (nm)	τ (nm)	d_{TEM} (nm)
30 s	4.50	5.81	4.61	5.42
3 min	4.19	5.21	4.38	5.26
30 min	4.38	5.6	4.74	5.86
3 h	4.19	5.48	4.40	5.39

Table 3.2. Comparison of the mean crystallite diameters calculated using the Scherrer equation (τ) and the mean diameters based on TEM measurements (d_{TEM}) for the RhPd alloys made by each of the eight synthetic conditions tested.

X-ray Photoelectron Spectroscopy

X-ray photoelectron spectroscopy (XPS) spectra were collected using a Kratos Axis Ultra Photoelectron Spectrometer, which employs a monochromated Al Kα X-ray source (1486.5 eV), hybrid optics (i.e., using both magnetic and electrostatic lenses) and a multi-channel plate coupled to a hemispherical photoelectron kinetic analyzer. The samples used in the analysis were simply square pieces of the NP-PVP composite film cut into squares approximately 3 mm on a side. Spectra were recorded with a pass energy of 20 eV, a step size of 0.1eV, an aperture slot of 300 x 700 μm, a dwell time of 1800 ms, and four sweeps so the data could be averaged. To minimize sample charging and any resulting band distortion, a Kratos charge neutralizer (20 eV electrons) was used and the sample stage was left ungrounded. Casa XPS analysis software was used for peak deconvolution and the corrected peak areas were used in conjunction with the appropriate Kratos sensitivity factors for each element to determine the stoichiometry of the sample.

Sample	wt% Rh	wt% Pd	mol% Rh	mol% Pd
RhPd Mw30s	0.518%	0.857%	38.5%	61.5%
RhPd Mw3min	0.295%	0.357%	46.1%	53.9%
RhPd Mw30min	0.301%	0.396%	44.0%	56.0%
RhPd Mw3h	0.621%	0.791%	44.8%	55.2%
RhPd Cv30s	0.343%	0.389%	47.7%	52.3%
RhPd Cv3min	0.315%	0.276%	54.1%	45.9%
RhPd Cv30min	1.060%	0.960%	53.3%	46.7%
RhPd Cv3h	0.305%	0.495%	38.9%	61.1%
Rh Mw	0.823%			
Rh Cv	0.459%			
Pd Mw		0.669%		
Pd Cv		0.740%		
Rh+Pd Mw	1.556%	1.099%		
Rh+Pd Cv	1.021%	1.761%		

Table 3.3. Weight percent of Rh and Pd in each of the catalysts tested, and the fraction of the total metal that was Rh and Pd in each of the alloy catalysts.

Inductively Coupled Plasma Optical Emission Spectrometry

Inductively coupled plasma mass spectrometry (ICP-MS) was performed using a Perkin Elmer DRCII ICP-MS with a quadrupole spectrometer. Samples were prepared by digesting

ca. 5 mg of supported nanoparticle catalyst in aqua regia in Easy-Prep microwave pressure vessels at 175 °C for 3 h. Aliquots of these digest solutions were diluted with 2% HNO_3 to achieve predicted metal concentrations near 1000 ppb. Calibration standards were prepared using the precursor chloride salts in 2% HNO_3.

Catalyst Preparation

Amorphous silica (120 mg) and PVP-nanoparticle film (8 mg) were weighed into a 20 mL scintillation vial. A 1:1 mixture of ethanol and water was added to the vial, dissolving the film. The vial was swirled with sonication to disperse the silica throughout the solution, then sonicated an additional 25 min to support the nanoparticles on the silica. The catalyst was recovered by filtering the suspension through a D-frit and dried overnight in an oven at 70 °C. Noble metal loadings varied between 0.42 and 1.71 wt%, as judged by ICP-OES.

Catalytic Studies

For each catalytic trial, about 3-5 mg of previously prepared NP-silica composite was thoroughly mixed with 125 mg of acid-washed, calcined sand and loaded into a custom-made quartz U-tube, resting on a D3-porosity frit. The catalyst was held at 25 °C using a water bath and a circulating chiller. The in-line, fritted cyclohexene bubbler was cycled between vacuum and the reactant gas mixture (H_2/He 1:1) three times, and the rest of the reactor line (quartz, heated to 90 °C with heating tape) was evacuated for 20 minutes before each run to remove air from the line. The reactant gas mixture was then passed over the catalyst for 30 minutes with the cyclohexene bubbler closed to activate the nanoparticles. The opening of the bubbler introduced cyclohexene vapor into the reactant gas mixture, initiating the catalysis trial. Data was collected *via* automated, pneumatically gated sampling of the exhaust stream into an HP Agilent 6890 GC with a 15 m Restek Stabilwax column and tandem FID and TCD detectors. Collection was continued for 6 h.

To facilitate the calculation of activation energies, one variable temperature experiment was performed on each catalyst. After the usual 6 h experiment at 25 °C, the temperature of the catalyst bath was increased to 30 °C and data collection continued as

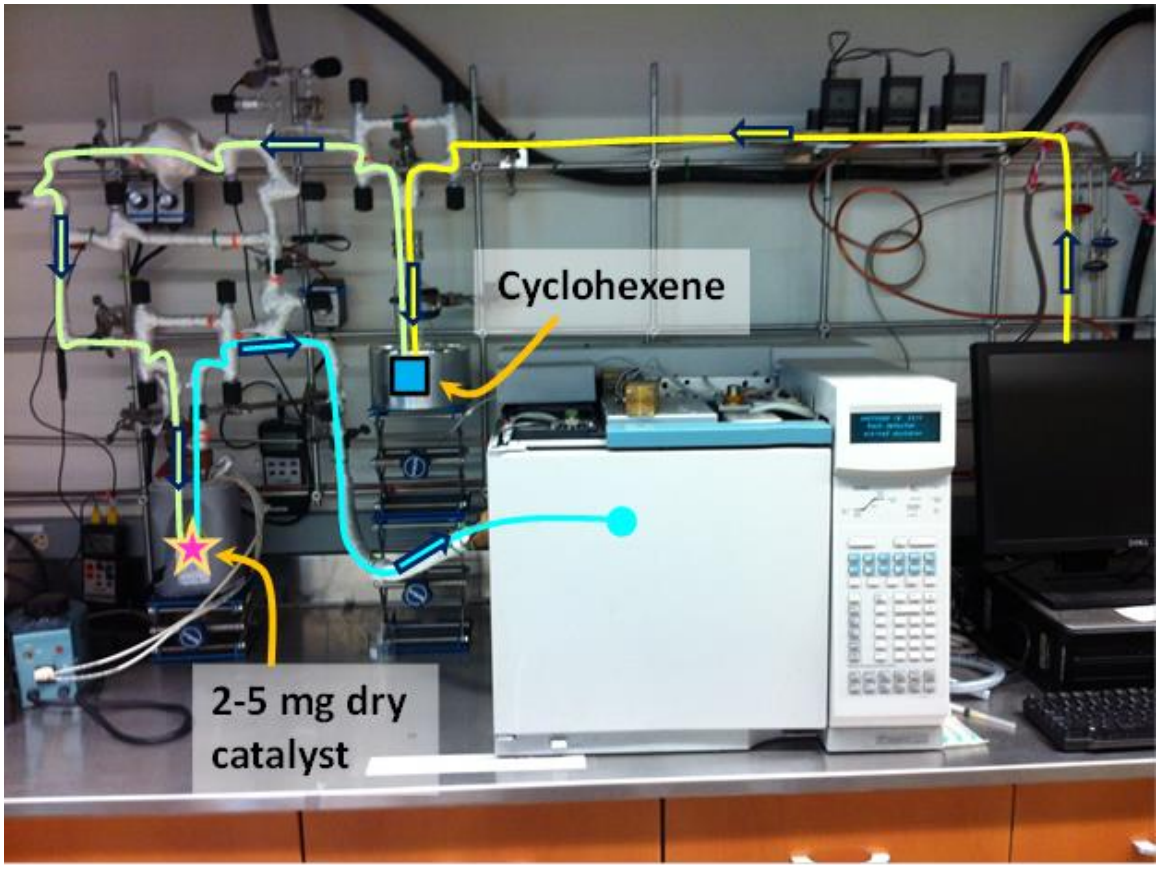

Scheme 3.2. Diagram of the gas phase hydrogenation setup. The flow of H_2/He (yellow) picks up cyclohexene vapors in the ice bath-cooled bubbler, and the reactant gas mixture (yellow and blue) continues to the catalyst bed (star). The product mixture (blue) then enters the GC for analysis.

the temperature of the catalyst re-equilibrated. After five consistent conversion measurements had been collected (usually after *ca.* 45 – 60 min), the temperature of the bath was decreased by five degrees; this process was repeated until data had been collected for the temperature range from 10 – 30 °C.

Recyclability studies were performed by reactivating the catalyst under flow of H_2/He at room temperature for 6 h after the end of the initial run, then resuming data collection for a further 6 h. This process was repeated to get a total of three runs.

Catalytic Data Analysis

Activities and turnover frequencies (TOFs) were calculated using surface area-to-volume ratios estimated from the diameters obtained from TEM and assuming all NPs were perfect cuboctahedra. To calculate the activity of a catalyst, the flow rate of the reactant (cyclohexene, in μmol min^{-1}) was multiplied by the percent conversion of cyclohexene into cyclohexane. The conversion percent was itself calculated by normalizing the peak areas (GC data) for cyclohexene and cyclohexane with respect to their molecular weights, then dividing the normalized area of the cyclohexane peak by the sum of the normalized cyclohexene and cyclohexane peaks. Finally, this value was divided by the mass of the catalyst used to give activity in $mol_{cyclohexane}\ g_{catalyst}^{-1}\ s^{-1}$.

$$\frac{mol\ \text{cyclohexene}}{s} \times \left[\frac{\dfrac{\text{Area Count}_{\text{Cyclohexane}}}{\text{MW}_{\text{Cyclohexane}}}}{\dfrac{\text{Area Count}_{\text{Cyclohexene}}}{\text{MW}_{\text{Cyclohexene}}} + \dfrac{\text{Area Count}_{\text{Cyclohexane}}}{\text{MW}_{\text{Cyclohexane}}}} \right] \times \frac{1}{g\ \text{catalyst}}$$

Turnover frequencies were calculated by converting the mass units in the activity to the number of moles of surface metal atoms. To do this, the activity was divided by the sum of the weight percents of rhodium and palladium as determined by ICP-OES, each of which was divided by its respective molar mass. This converted the mass of the total catalyst into the number of moles of metal; the two metals were counted together because both Rh and Pd are active for hydrogenation. This was further refined to surface atoms by dividing by the fraction of the metal atoms that would be exposed in a perfect cuboctahedron of comparable size (PME, percent metal exposed).

$$\frac{\text{Activity } (mol\ g^{-1}s^{-1})}{\left[\frac{\text{wt\% Rh}}{\text{MW}_{\text{Rh}}} + \frac{\text{wt\% Pd}}{\text{MW}_{\text{Pd}}}\right] \times \text{PME}}$$

Activation energies were found using the steady-state activities at five different temperatures from 10 to 30 °C to construct an Arrhenius plot.

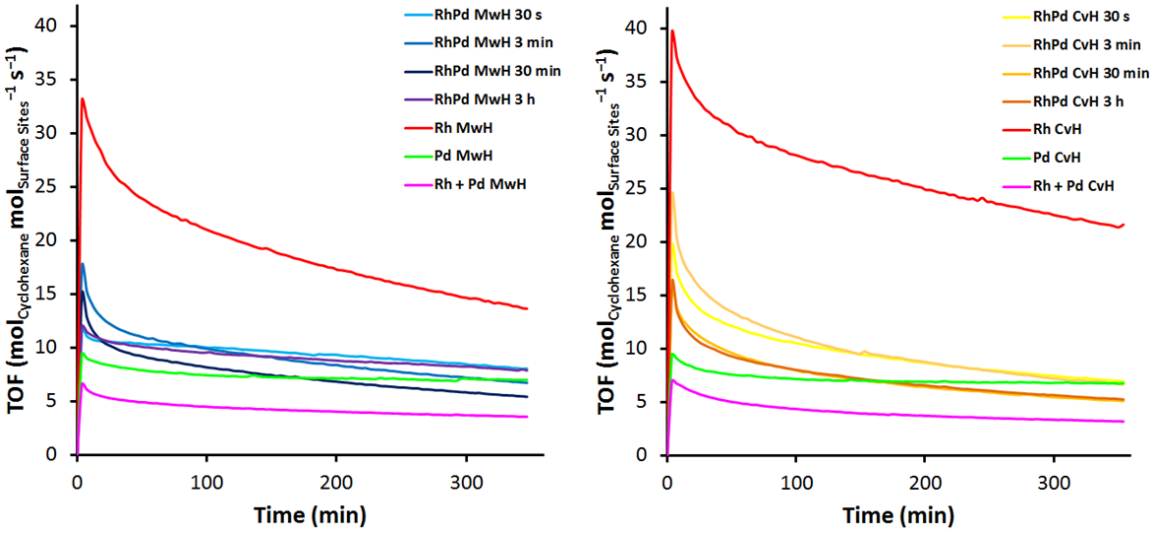

Figure 3.8. Hydrogenation results for each catalyst tested, both microwave heated (left) and conventionally heated (right).

	RhPd, MwH 30 s		RhPd, MwH 3 h	
	SS TOF	% Loss	SS TOF	% Loss
Run 1	14.76		9.70	
Run 2	10.72	37.69	7.58	21.86
Run 3	8.85	21.13	6.19	18.34

Table 3.4. Comparison of the steady-state TOF values of microwave-heated RhPd nanoparticles with reaction times of 30 s and 3 h over the course of the recyclability study.

30 seconds

3 minutes

30 minutes

3 hours

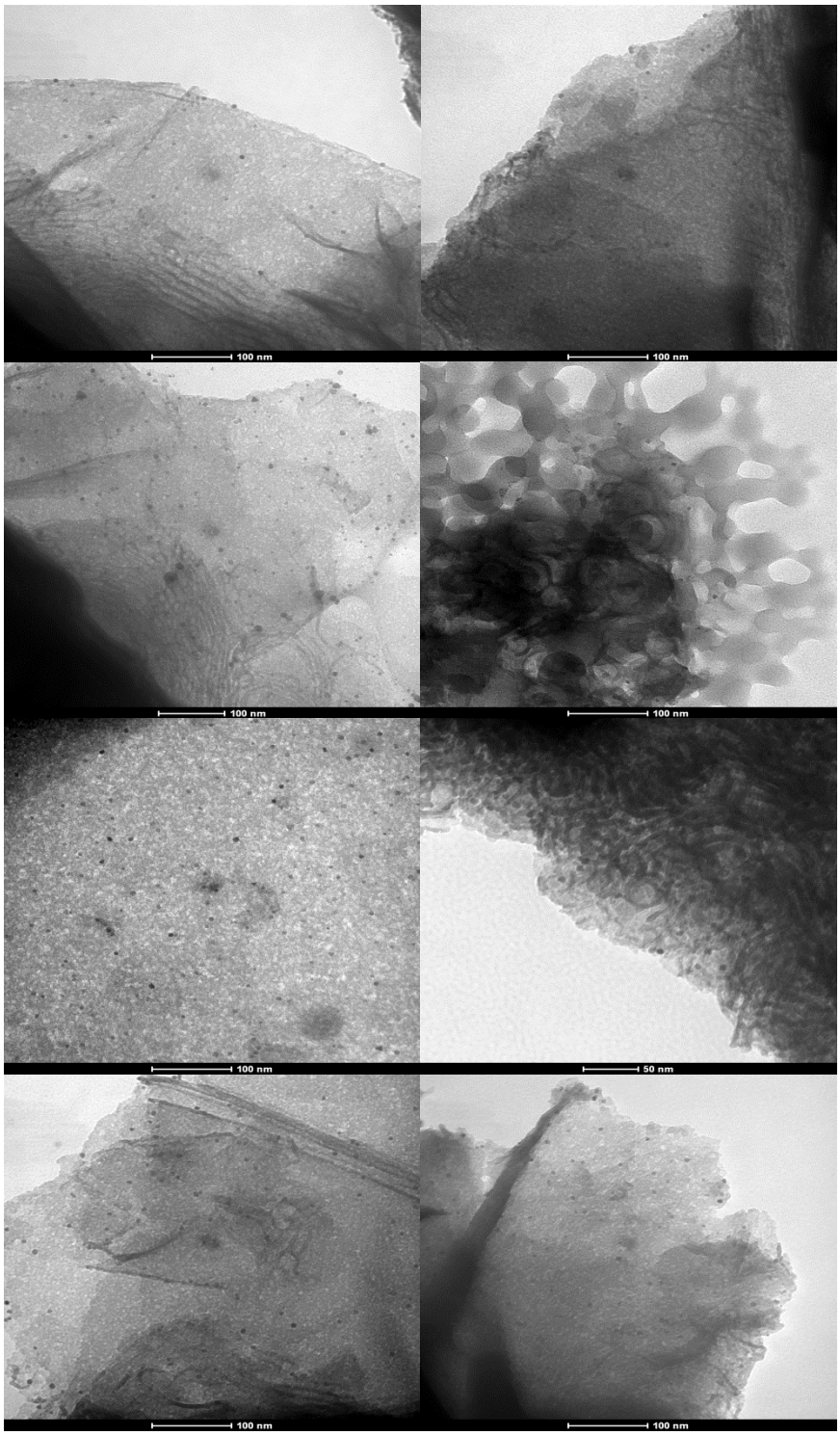

Figure 3.9. TEM images of the microwave-heated RhPd catalysts before (left) and after (right) use.

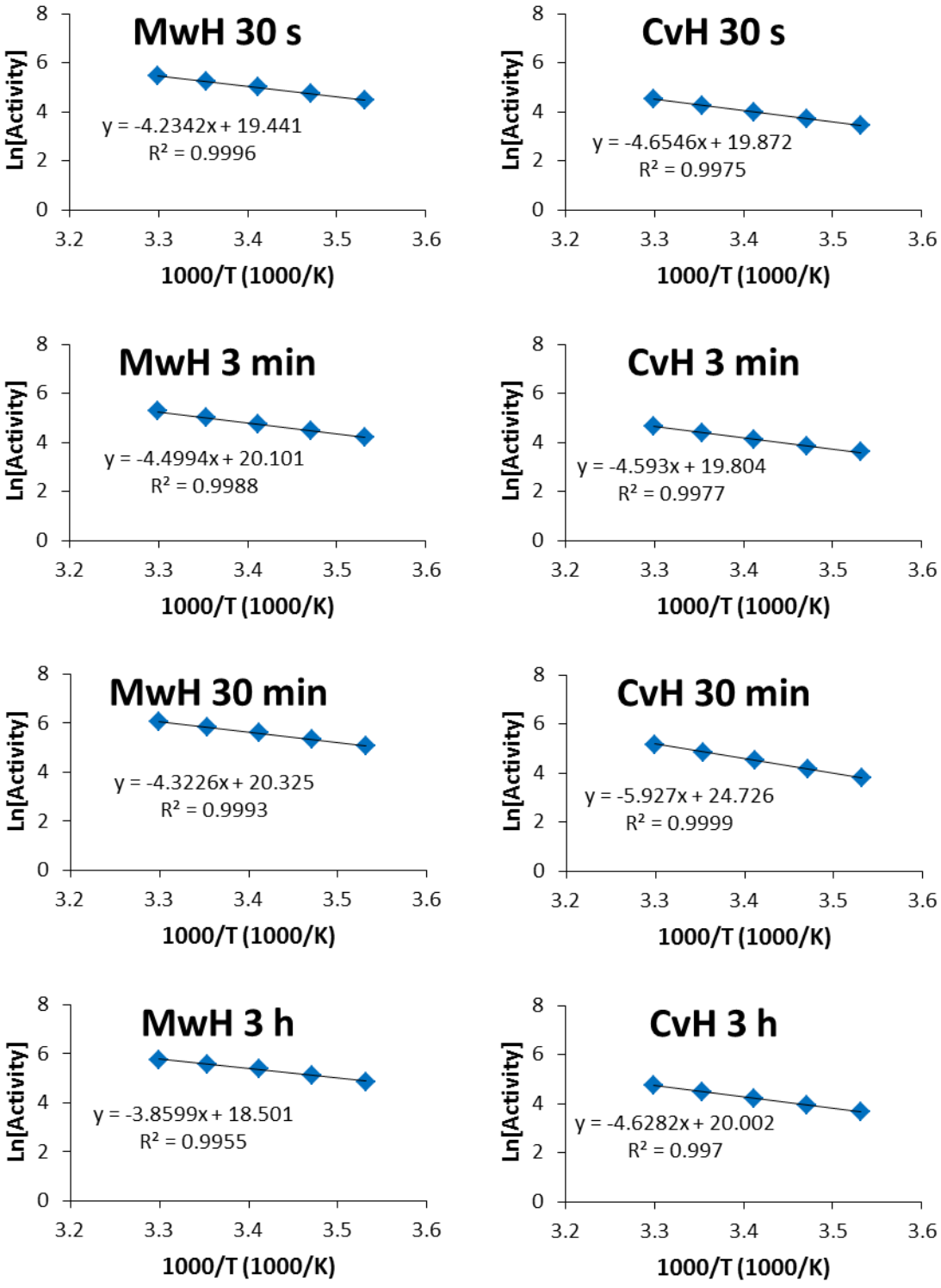

Figure 3.10. Arrhenius plots for RhPd nanoparticles made by all eight methods.

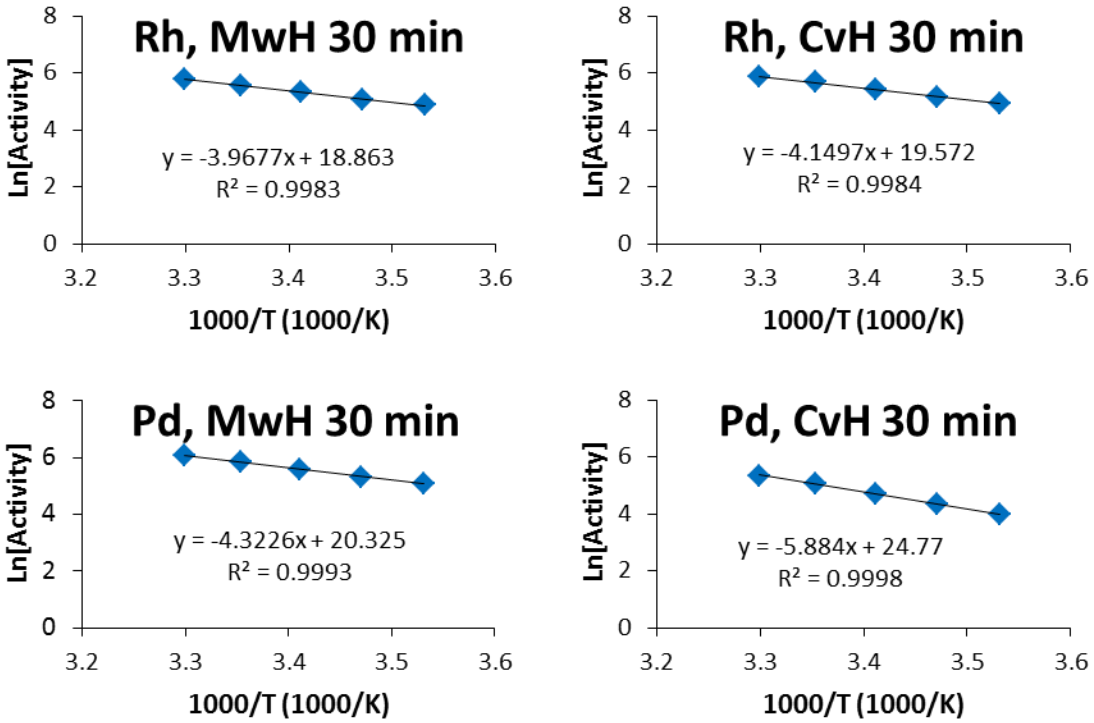

Figure 3.11. Arrhenius plots for pure Rh and Pd nanoparticles made by both microwave and conventional heating.

	Activation Energy (kJ mol^{-1})	
Catalyst	**MwH**	**CvH**
RhPd, 30 s	35.2	31.6
RhPd, 3 min	37.4	38.2
RhPd, 30 min	35.9	36.4
RhPd, 3 h	32.1	38.5
Rh, 30 min	33.0	34.5
Pd, 30 min	49.3	48.9

Table 3.5. Activation energies for all RhPd, Rh, and Pd nanoparticles tested.

Computational Methods

Hydrogen binding energies on pure Rh, Pd and Rh-Pd alloy surfaces were calculated using density functional theory (DFT) as implemented in the Vienna *Ab initio* Simulation Package.[26] Core electrons were described with the projector augmented-wave method.[27,28] Electron correlation was evaluated with the Perdew−Burke−Ernzerhof functional.[29] For the valence electrons, Kohn−Sham wave functions were expanded in a plane wave basis set[30,31] with an energy cutoff of 400 eV. Geometries were considered optimized when the force on every atom was lower than 0.05 eV/Å. The Brillouin zone was sampled with a 3×3×1 Monkhorst−Pack *k*-point mesh.[32,33]

All H binding energies were calculated at the fcc hollow site on the (111) surface of a four-layer (4×4) slab. The bottom two layers of the slab were fixed in bulk positions; the top two layers were allowed to relax. To model the $Rh_{0.50}Pd_{0.50}$ alloy, ten random alloy configurations were generated so that the H binding energies could be calculated at four different triatomic ensembles, including Rh_3, Rh_1Pd_2, Rh_2Pd_1 and Pd_3. From these random configurations, ten H binding were calculated for each ensemble. The H_2 molecule was used as the reference state for the H binding calculations.

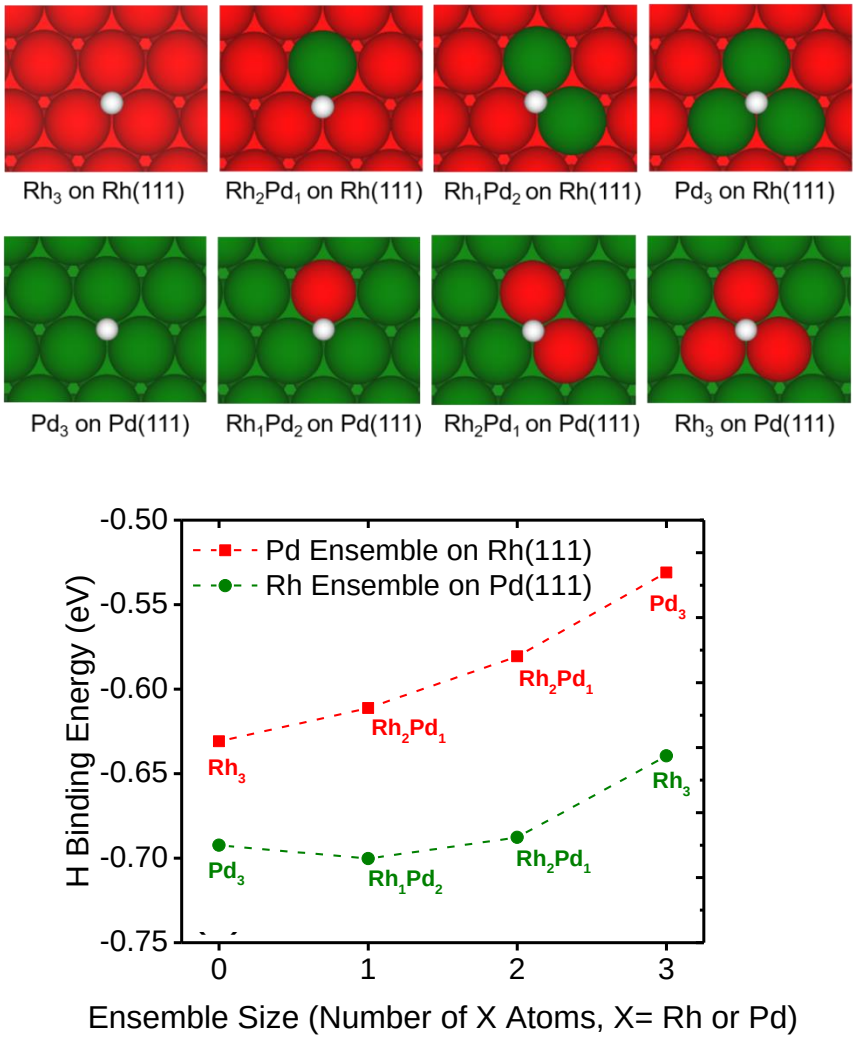

Figure 3.12. Illustration of the different triatomic ensembles binding H on (top) Rh(111) and (middle) Pd(111). The red spheres represent Rh atoms, green are Pd, and white are H atoms. Bottom: Calculated H binding energies at the different atomic ensembles shown in the illustrations above.

Synthesis of RhPd Alloy Nanoparticles

RhPd alloy nanoparticles were synthesized using a modified version of the method reported by García, *et al.*[14] 10 mg of $RhCl_3 \cdot xH_2O$ was dissolved in 2.5 mL of ethylene glycol in a scintillation vial. The solution was transferred to a separate vial with 15 mg of K_2PdCl_4 to dissolve the second precursor. The precursor solution was then loaded into a 10 mL syringe. Meanwhile, 200 mg of PVP was dissolved in 15 mL of ethylene glycol in a 50 mL round-bottom flask. A magnetic stir bar was added to the flask, and the flask was attached to a water-cooled reflux condenser inside a CEM MARS 5 programmable microwave chamber. The syringe with the precursor solution was loaded into a programmable syringe pump. PTFE tubing was threaded down the condenser into the round-bottom flask and secured to the syringe needle with PTFE tape. Once the PVP solution had been heated to 165 °C (6 min ramp), the precursor solution was injected at 320 mL h^{-1}. Once the injection was complete, the solution was stirred at 165 °C for a set time (30 s, 3 min, 30 min, or 3 h) before the flask was transferred to an ice bath to quench the reaction. Once the solution was cold, it was evenly distributed between two 50 mL centrifuge tubes. Each half was diluted to 40 mL with acetone and centrifuged at 5500 rpm for 5 min to precipitate the nanoparticles. The clear supernatant was discarded. The dark, viscous fluid containing the nanoparticles was dispersed in 5 mL of ethanol per tube with the aid of sonication. The particles were re-precipitated by adding 30 mL of hexanes to each tube and centrifuging at 5500 rpm for 5 min. This ethanol-hexanes wash was performed a total of two times. The product was dried in a vacuum desiccator overnight to yield a black film.

For comparison, RhPd NPs were also made by conventional oil bath heating. The conditions used were identical to those used for the microwave synthesis; only the heating method was changed. The temperature of the oil bath was monitored with a

thermometer, and the reaction flask was allowed 30 minutes to equilibrate at 165 °C prior to precursor injection.

Synthesis of Pure Rh and Pd Nanoparticles

Monometallic Rh and Pd NPs were synthesized as controls using the method reported by Dahal, *et al*.[22] To ensure comparably sized particles from both MwH and CvH in each case, a secondary injection of Rh precursor was performed in the CvH Rh synthesis, but the initial seeding injections were deemed sufficient for the other three. All post-injection heating times were 30 min for the monometallic particles.

REFERENCES

1. J. D. Burrington, *Industrial Catalysis: Chemistry and Mechanism*, Imperial College Press, London, **2016**.
2. K. C. Taylor, *Catal. Rev.* **1993**, *35*, 457-481.
3. L. Yin, J. Liebscher, *Chem. Rev.* **2007**, *107*, 133-173.
4. N. R. Shiju, V. V. Guliants, *Appl. Catal. A*. **2009**, *356*, 1-17.
5. B. Yoon, C. M. Wai, *J. Am. Chem. Soc.* **2005**, *127*, 17174-17175.
6. X.-R. Ye, Y. Lin, C. Wang, M. H. Engelhard, Y. Wang, C. M. Wai, *J. Mater. Chem.* **2004**, *14*, 908-913.
7. R. Schlögl, *Angew. Chem. Int. Ed.* **2015**, *54*, 3465-3520.
8. P. Fröhlich, T. Lorenz, G. Martin, B. Brett, M. Bertau, *Angew. Chem. Int. Ed.* **2017**, *56*, 2544-2480.
9. D. Astruc, F. Lu, J. R. Aranzaes, *Angew. Chem. Int. Ed.* **2005**, *44*, 7852-7872.
10. T. P. Bigioni, X. M. Lin, T. T. Nguyen, E. I. Corwin, T. A. Witten, H. M. Jaeger, *Nat. Mater.* **2006**, *5*, 265-270.
11. N. R. Jana, L. Gearheart, C. J. Murphy, *Chem. Mater.* **2001**, *13*, 2313-2322.
12. T. K. Sau, C. J. Murphy, *J. Am. Chem. Soc.* **2004**, *126*, 8648-8649.
13. Y. G. Sun, Y. N. Xia, *Science* **2002**, *298*, 2176-2179.

14. S. García, L. Zhang, G. W. Piburn, G. Henkelman, S. M. Humphrey, *ACS Nano* **2014**, *8*, 11512-11521.

15. H. Kobayashi, K. Kusada, H. Kitagawa, *Acc. Chem. Res.* **2015**, *48*, 1551-1559.

16. S. N. Tripathi, S. R. Bharadwqi, *J. Phase Equilib.* **1994**, 15, 208-212.

17. H. Noh, T. B. Flanagan, B. Cerundolo, A. Craft, *Scr. Metall. Mater.* **1991**, *25*, 225-230.

18. H. Noh, J. D. Clewley, T. B. Flanagan, A. P. Craft, *J. Alloy Compd.* **1996**, *240*, 235-248.

19. A. K. M. F. Kibria, Y. Sakamoto, *Int. J. Hydrogen Energy*, **2000**, *25*, 853-859.

20. H. Kobayashi, H. Morita, M. Yamauchi, R. Ikeda, H. Kitagawa, Y. Kubota, K. Kato, M. Takata, S. Toh, S. Matsumura, *J. Am. Chem. Soc.* **2012**, *134*, 12390-12393.

21. J. Polte, *CrystEngComm*, **2015**, *17*, 6809-6830.

22. N. Dahal, S. García, J. Zhou, S. M. Humphrey, *ACS Nano* **2012**, *6*, 9433-9446.

23. Y. Xiong, J. Chen, B., Wiley, Y. Xia, S. Aloni, Y. Yin, *J. Am. Chem. Soc.* **2005**, *127*, 7332-7333.

24. P. Kunal, H. Li, B. L. Dewing, L. Zhang, K. Jarvis, G. Henkelman, S. M. Humphrey, *ACS Catal.* **2016**, *6*, 4882-4893.

25. W. Tang, G. Henkelman, *J. Chem. Phys.* **2009**, *130*, 194504.

26. G. Kresse, J. Hafner, *Phys. Rev. B: Condens. Matter Mater. Phys.* **1993**, *47*, 558−561.

27. P. E. Blöchl, *Phys. Rev. B: Condens. Matter Mater. Phys.* **1994**, *50*, 17953−17979.

28. G. Kresse, D. Joubert, *Phys. Rev. B: Condens. Matter Mater. Phys.* **1999**, *59*, 1758−1775.

29. J. P. Perdew, K. Burke, M. Ernzerhof, *Phys. Rev. Lett.* **1996**, *77*, 3865−3868.

30. P. Hohenberg, W. Kohn, *Phys. Rev.* **1964**, *136*, B864−B871.

31. W. Kohn, L. J. Sham, *Phys. Rev.* **1965**, *140*, A1133−A1138.

32. H. J. Monkhorst, J. D. Pack, *Phys. Rev. B* **1976**, *13*, 5188−5192.

33. M. Methfessel, A. T. Paxton, *Phys. Rev. B: Condens. Matter Mater. Phys.* **1989**, *40*, 3616−3621.

Chapter Four: Trimetallic RhPdAg and RhPdAu Alloy Nanoparticles for Hydrogenation Catalysis Applications

Syntheses of the trimetallic alloy systems RhPdAg and RhPdAu were explored. RhPdAg was found to form a trimetallic alloy phase alongside a AgCl byproduct; however, efforts to remove the AgCl either proved unsuccessful or simultaneously resulted in the agglomeration of the existing metallic particles into chain-like structures. On the other hand, distinct RhPdAu nanoparticles were readily synthesized in a range of compositions. These RhPdAu nanoparticles have been characterized by TEM, XRPD, XPS, and EDX mapping. Hydrogenation catalysis studies of the RhPdAu particles are in preparation.

INTRODUCTION

As discussed in Chapter 3, the mixing of different metals to form an alloy can create a system that has markedly different properties from either of the component metals.[1,2] RuPd nanoparticles can take on the crystal structure of either of the component metals, and are more active toward CO oxidation than either one.[3] Mixing rhodium with either silver or gold makes an alloy that is a more active hydrogenation catalyst than pure rhodium, despite neither of the other two metals being catalytically active toward hydrogenation at room temperature.[4] By forming an alloy, the differing electronic states of each metal contribute to an entirely new energy profile for the material, thus greatly expanding the possibilities for functional nanomaterials.[3-8]

Indeed, the exploration of alloy nanoparticles need not stop at binary alloys. By including a third metal and forming a ternary alloy, the number of possible combinations expands tremendously; by adjusting the relative proportion of each element, the

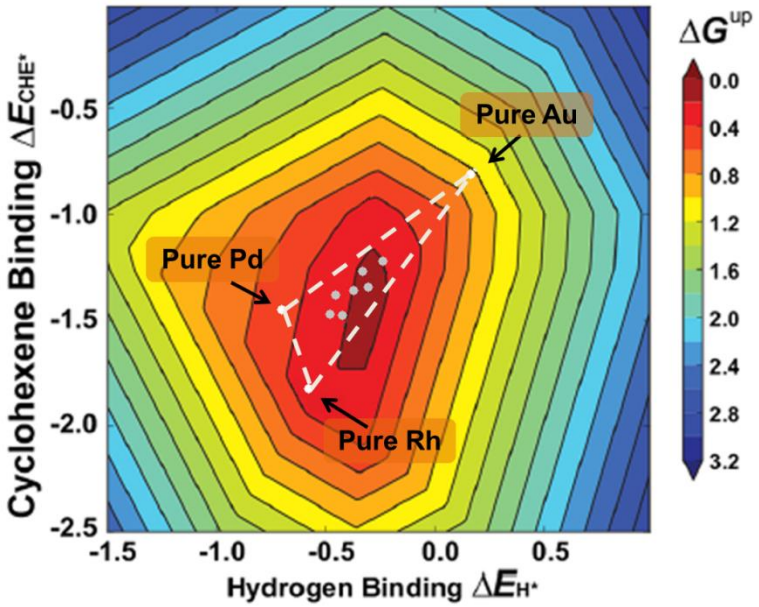

Figure 4.1. Volcano plot demonstrating the relationship between cyclohexene and hydrogen binding energies and the predicted hydrogenation activity of various metal catalysts. Pure Rh, Pd, and Au are represented as white dots connected by dashed lines that outline the possible combinations of the three metals. The compositions targeted in this study are marked in grey.

properties of the nanoparticles can be fine-tuned to suit the application at hand. In addition, as with the RhAg and RhAu examples, combinations that improve reactivity may also allow more expensive active metals like rhodium to be diluted with cheaper, more earth-abundant metals, enabling more efficient stewardship of scarce natural resources. The formation of more complex alloy systems also enables further exploration of the predictive methods previously used to understand the reactivity of RhAg, RhAu, RhPd, and PdAu.[4,9] To this end, a range of compositions are planned that will examine the space bounded by these three-metal combinations (Figure 4.1).

The two systems described in this chapter, RhPdAg and RhPdAu, represent extensions of the RhPd alloy system described in Chapter 3. By incorporating gold or silver into the alloy, the hydrogen and cyclohexene binding energies of the system are

predicted to more closely match the optimal values for the hydrogenation reaction. In addition, the production of these ternary alloy systems will allow detailed study of heretofore unreported materials. Several reports exist of alloys containing two of the three elements combined here,[10,11] typically platinum-containing systems like RhPtAu[12] or PdPtAu,[13,14] but this represents the first reported work on either RhPdAg or RhPdAu.

RESULTS AND DISCUSSION

RhPdAg Nanoparticles

The synthesis of RhPdAg nanoparticles was undertaken using the procedure for making RhAg nanoparticles as a starting point. Because silver chloride is insoluble in ethylene glycol and the most commonly used rhodium and palladium precursors are chloride salts, these two syntheses form some amount of silver chloride over the course of the synthesis; this AgCl byproduct must then be removed, or the accurate quantification of the composition of the alloy will be jeopardized. The reported method for AgCl removal is to add a post-synthesis ammonia wash to dissolve the byproduct amidst the other washes designed to remove excess capping agent.

Unfortunately, the removal of AgCl by concentrated ammonia consistently results in the aggregation of the remaining nanoparticles into structures that resemble beaded chains. X-ray powder diffraction patterns did show peak shifts in several of the targeted compositions suggestive of silver incorporation into the alloy phase, but TEM and EDX mapping revealed some of the silver had formed separate, monometallic particles (Figure 4.2). Within the group, the etching of silver out of an alloy and the formation of pure silver particles are known to be potential consequences of the ammonia wash. TEM of RhPdAg systems in the absence of an ammonia wash reveal distinct nanoparticles with a

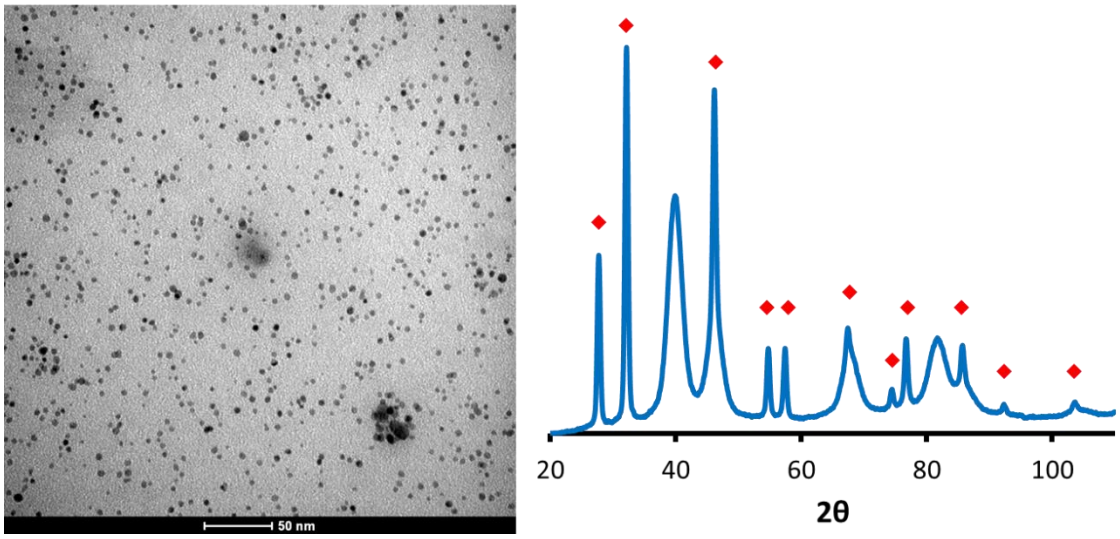

Figure 4.2. Analyses of nanoparticles with the overall composition $Rh_{25}Pd_{45}Ag_{30}$. Left: TEM image and XRPD pattern (overlay). Center: EDS map of an outlying particle showing only Ag metal and at least surface Cl^-. Right: EDS map of agglomerated particles showing all three metals, but predominantly Rh and Pd.

relatively monodisperse size distribution, but also larger AgCl structures. Attempts to remove the larger AgCl particles by centrifugation were only partially effective, and AgCl was still detectable in the XRPD pattern after several rounds of centrifugation (Figure 4.3). At the time of writing, these issues have not been resolved.

RhPdAu Nanoparticles

The synthesis of RhPdAu nanoparticles was patterned after the synthesis of RhAu alloy nanoparticles as described by García, *et al.*[4] The inclusion of gold does not present any new solubility concerns the way the inclusion of silver does, but gold must be reduced quickly to prevent the formation of large gold particles. To this end, $NaBH_4$ was incorporated into the synthesis by dissolving it in the capping agent solution immediately prior to the start of the heating method. All three metal precursor salts were dissolved

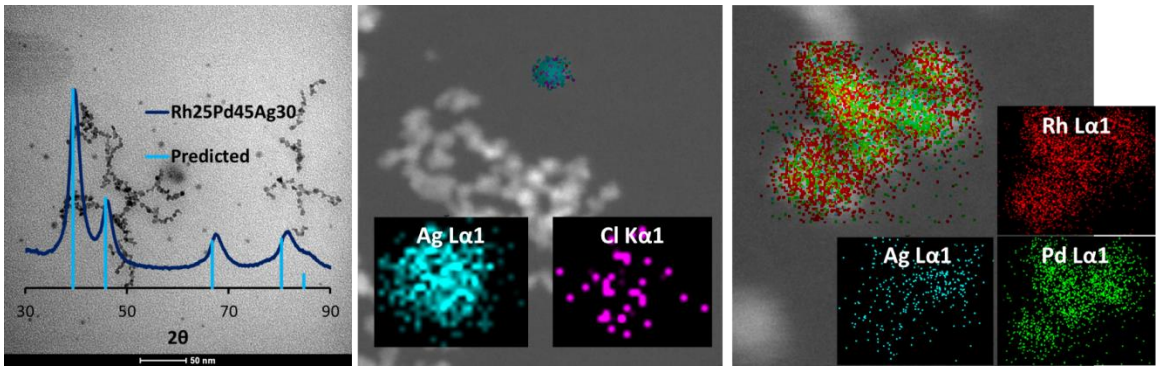

Figure 4.3. TEM image (left) and XRD pattern (right) of nanoparticles with the nominal composition $Rh_{35}Pd_{35}Ag_{30}$. The sharp diffraction peaks marked with red diamonds match the documented pattern of AgCl.

separately, then combined immediately prior to synthesis and injected together. The mole ratios between the three metals were varied as follows: one composition had all three metals equal (RhPdAu(1:1:1)), three had one metal twice as abundant as the other two (2:1:1, 1:2:1, 1:1:2), and three had one metal half as abundant as the other two (1:2:2, 2:1:2, 2:2:1). These seven compositions allow for a good sampling of the space between rhodium, palladium, and gold, while also maintaining at least 20% abundance of any given metal, which is expected to aid elemental quantification.

TEM analysis of the synthesized RhPdAu nanoparticles revealed a fairly monodisperse size distribution for each composition and average particle diameters from 3.0 – 4.0 nm (Figure 4.4). This size is noticeably smaller than the RhPd nanoparticles described in Chapter 3, but that is easily attributable to the presence of $NaBH_4$; the stronger reducing agent would produce a large population of small nanoparticles more quickly than would ethylene glycol alone, leaving less precursor available for each particle to grow. XRPD patterns of most of the compositions appear to have a single fcc phase, though the compositions more rhodium-rich or gold-poor than the "1:1:1" sample appears to show clearly segregated Au- and Rh-rich phases (Figure 4.5). The (111) peaks

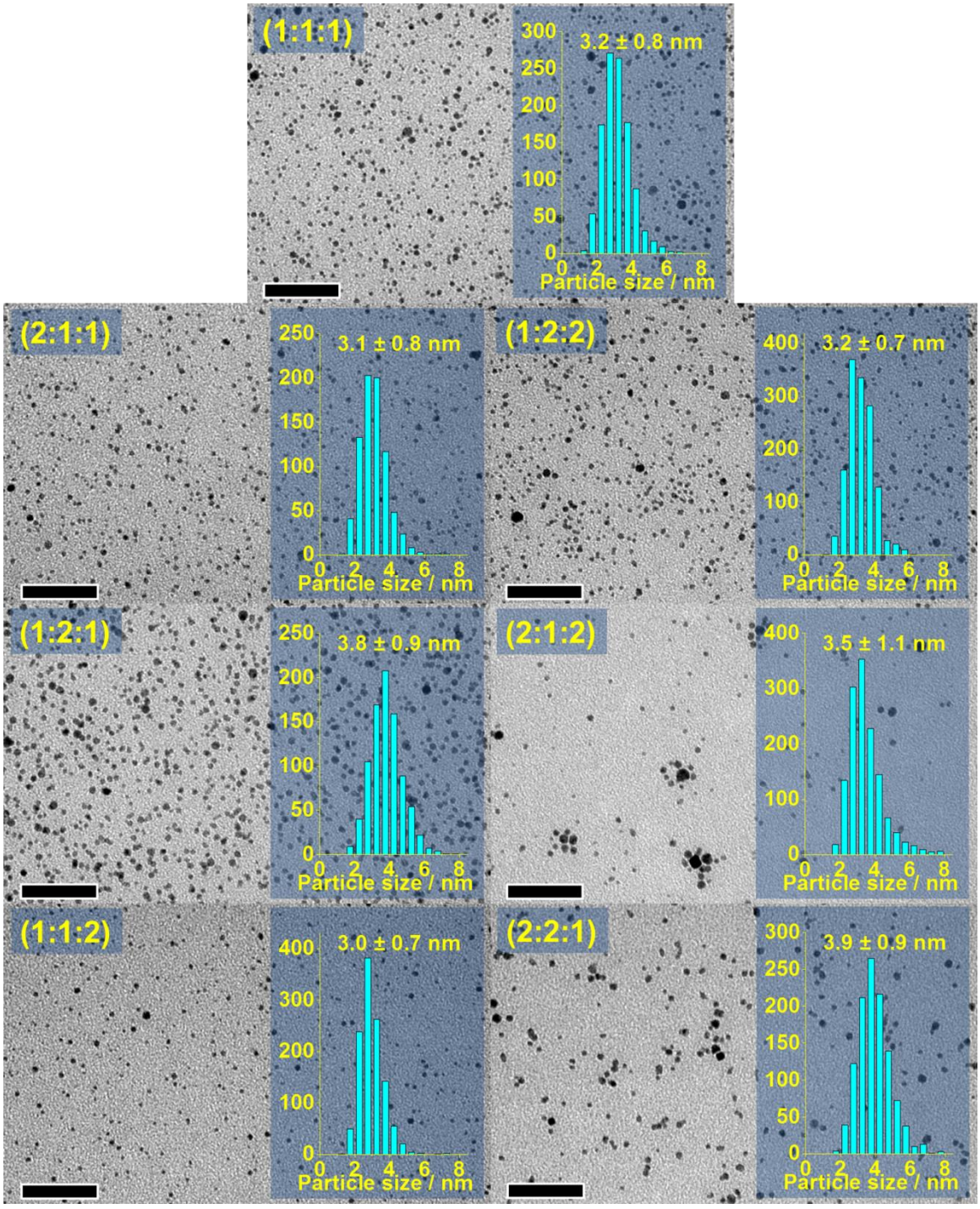

Figure 4.4. TEM images and size distributions of all seven RhPdAu compositions studied.

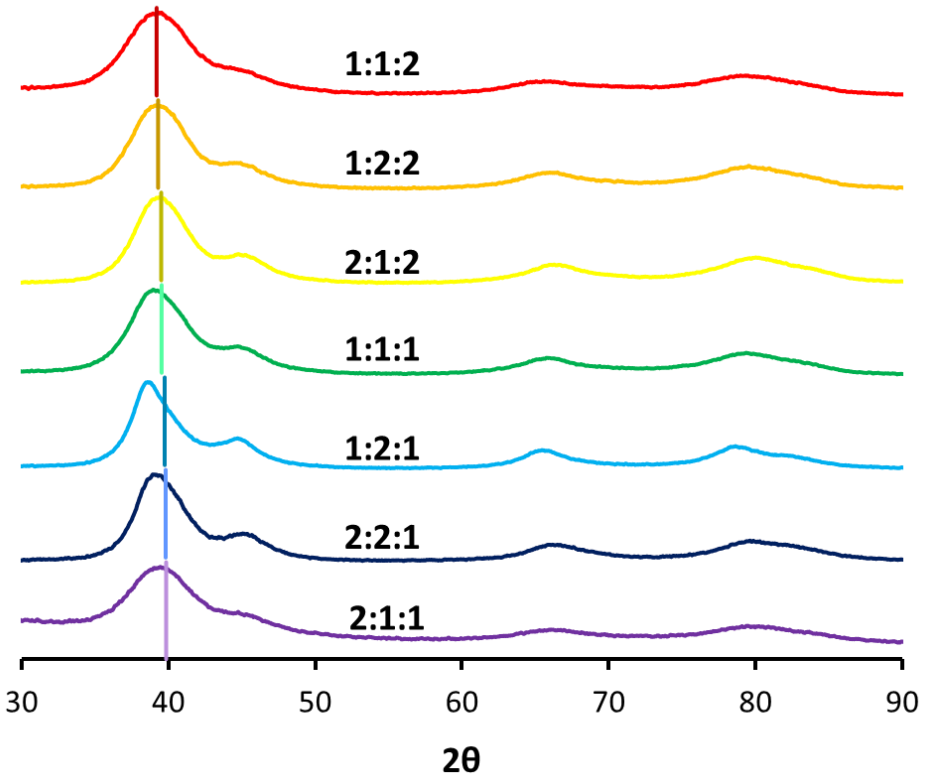

Figure 4.5. XRPD spectra of each of the RhPdAu compositions tested, with the predicted 2θ values of the (111) peaks marked.

of the other patterns appear to line up reasonably well with the 2θ values than would be predicted from a simple linear combination of the three pure metal peak positions, *a la* Vegard's law.

Elemental analysis by EDX mapping and XPS indicate that the more segregated compositions have gold-rich cores surrounded by rhodium-rich shells. The vast majority of particles mapped in each composition contained at least some of all three metals, though they were not always evenly distributed; EDX maps of each composition can be found in Figures 4.7 and 4.8 at the end of this chapter. The linescan in Figure 4.6

generated from the RhPdAu(1:1:1) map in Figure 4.7 makes this explicit: gold is clearly more abundant in the core than it is on the surface of the particle. The XPS spectra of the different compositions indicate unexpectedly rhodium-heavy and gold-poor elemental ratios; again using the 1:1:1 sample as an example, the rhodium abundance was determined to be 51% compared with 16% for gold (Table 4.1). Since XPS is highly surface sensitive and the top layers of the composite film are likely to be dominated by PVP, XPS analysis of PVP-capped nanoparticles tends to disproportionately sample the surface layers of the particles.[15] Furthermore, the oxidation state ratios indicate a large amount of rhodium has been oxidized to Rh(I), whereas the gold is almost exclusively Au(0). With this in mind, the XPS data can be seen to further support Rh-rich shells around Au-rich cores. Palladium, on the other hand, appears to be evenly distributed throughout the particle, which makes sense given that palladium is classically miscible with both of the other two elements, but Rh and Au are not classically miscible with each other.

	Composition						
	1:1:1	**1:1:2**	**1:2:1**	**2:1:1**	**1:2:2**	**2:1:2**	**2:2:1**
Rh mol%	**51.02%**	**52.99%**	**39.06%**	**47.58%**	**37.67%**	**39.59%**	**49.16%**
Rh(0)	30.45%	46.29%	15.53%	24.34%	18.87%	13.34%	32.93%
Rh(I)	69.55%	53.71%	84.47%	75.66%	81.14%	86.65%	67.08%
Pd mol%	**32.68%**	**23.33%**	**32.06%**	**30.61%**	**41.31%**	**27.92%**	**35.00%**
Pd(0)	85.92%	51.32%	78.65%	79.22%	67.58%	38.26%	71.29%
Pd(II)	14.09%	48.68%	21.34%	20.79%	32.42%	61.75%	28.70%
Au mol%	**16.30%**	**23.68%**	**28.90%**	**21.82%**	**21.02%**	**32.49%**	**15.84%**
Au(0)	82.16%	80.36%	81.49%	79.79%	75.53%	79.29%	72.59%
Au(I)	17.84%	19.63%	18.51%	20.21%	24.46%	20.71%	27.40%

Table 4.1. Elemental and oxidation state ratios for each nominal composition as determined by XPS

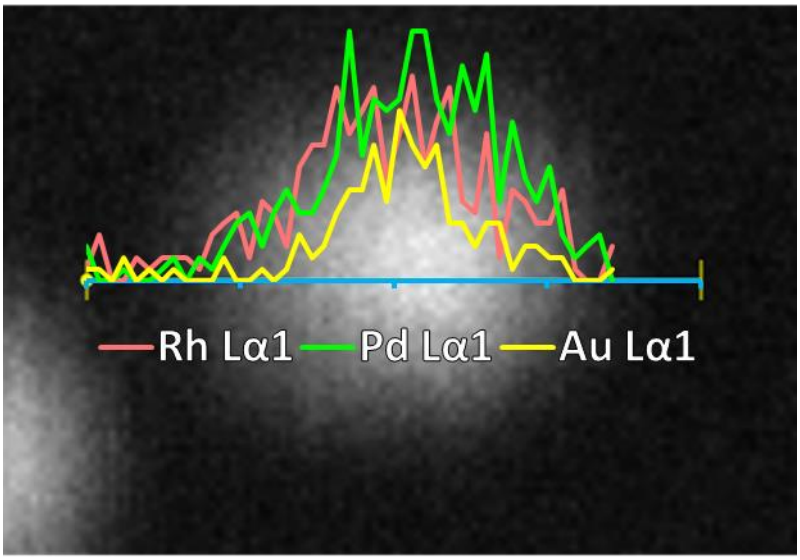

Figure 4.6. EDX linescan of a RhPdAu(1:1:1) nanoparticle.

FUTURE GOALS

Due to the apparent limitations of XPS, the actual elemental compositions of each RhPdAu alloy system must be determined by ICP-OES to compare with the nominal compositions. However, regardless of the immediate results of this measurement, two variables should be adjusted to try to encourage more homogenous alloying. First, the gold precursor should be dissolved only immediately before the reaction to rule out the formation of small gold clusters during the hour or more it takes the rhodium and palladium salts to dissolve. If tiny gold particles exist before the reaction is supposed to have started, that may be contributing to the abundance of gold in the core. On the other hand, re-oxidation of rhodium may be encouraging it to segregate toward the surface. The most likely culprit for oxidation would be the well-known O_2/Cl^- redox couple.[16] If this is the case, then performing the reaction under a nitrogen atmosphere and with degassed solvent may promote more even mixing of the metals.

Once the structure of the nanoparticles has been satisfactorily established, catalytic testing will commence. RhPdAu nanoparticles of each composition will first be supported on amorphous SiO_2 and tested for their ability to hydrogenate cyclohexene. This will feed into the established collaboration with the Henkelman Group and permit a valuable comparison between theoretical predictions and empirical fact for this previously unknown alloy system. These catalysts will then also be tested for their selectivity by applying them to the hydrogenation of crotonaldehyde. Finally, RhPdAu alloy nanoparticles will be supported on mesoporous Co_3O_4 to determine whether this reducible support can improve the selective hydrogenation of the crotonaldehyde carbonyl bond. The selective hydrogenation of crotonaldehyde to crotyl alcohol is discussed more fully in Chapter Five.

EXPERIMENTAL DETAILS

General

All of the RhPdAg and RhPdAu nanoparticles were synthesized using the polyol method, utilizing $RhCl_3 \cdot xH_2O$ (Strem Chemicals, 38-41% Rh) and K_2PdCl_4 (Strem Chemicals, 99%), $AgNO_3$ (Alfa Aesar, 99.9+% Ag), and $HAuCl_4$ (Strem Chemicals, 49% Au) as the metal precursors, poly(vinylpyrrolidone) (PVP; Alfa Aesar, MW = 58K, ~18 mol monomer/mol metal) as the capping agent, $NaBH_4$ (Alfa Aesar, 98%) as a supplementary reducing agent, and ethylene glycol (Fischer Scientific, 99.8%) as the solvent and reducing agent. These chemicals and all other solvents (analytical grade) were used as received. The microwave reactor was set up as described in Chapter 3, with the two exceptions that the temperature probe was placed in a beaker containing ethylene

glycol rather than a round-bottom flask, and the end of the injection tubing was submerged below the surface of the capping agent solution to prevent droplet formation.

Electron Microscopy

Transmission electron microscopy (TEM) images were produced using an FEI Technai microscope with an operating potential of 80 kV. Samples were prepared by drop-casting a dilute solution of nanoparticles in ethanol onto 200 mesh Cu/Formvar grids (Ted Pella, Inc.) and allowing the grid to air dry. The diameters of the nanoparticles were found by using the line tool in Image-J (http://rsbweb.nih.gov/ij) to measure the shortest distance across each particle that included the center of the particle. Over 300 particles across at least two images from different grid coordinates were measured for each set of reaction conditions. High-angle annular dark-field scanning TEM (HAADF-STEM) images and energy-dispersive X-ray spectroscopy (EDX) mapping and lines scans were obtained using a JEOL 2010F transmission electron microscope operating at 200 keV with a field-emission gun with 0.19 nm point-to-point resolution.

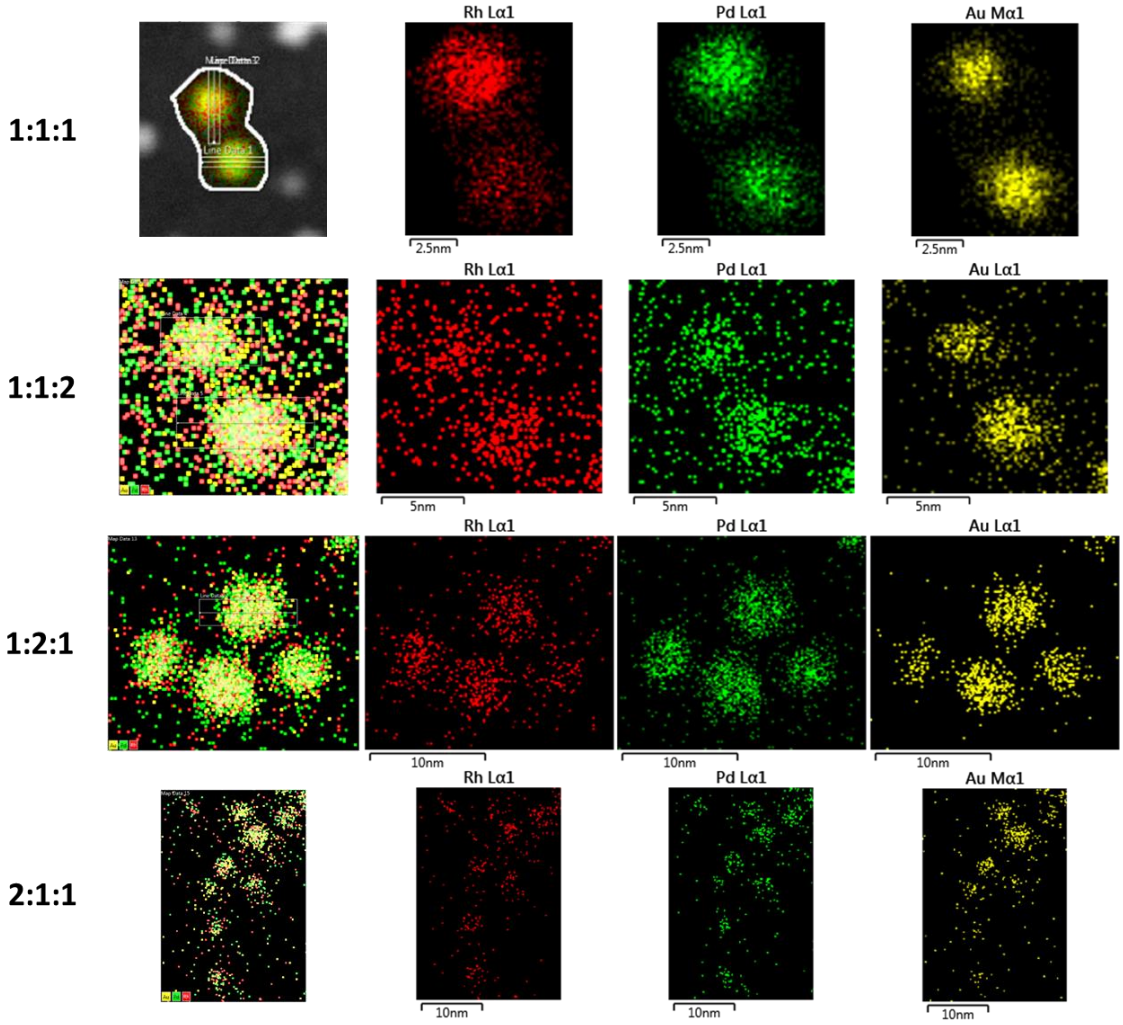

Figure 4.7. EDS maps of the 1:1:1, 1:1:2, 1:2:1, and 2:1:1 compositions, including overlay spectra (far left) and individual elemental maps.

X-ray Powder Diffraction

X-ray powder diffraction was performed using a Rigaku R-Axis Spider with a Cu Kα source (1.5418 Å) operating at 40 kV and 40 mA. X-ray spectra were collected using a sample rotation speed of 10° s^{-1} and a step width of 0.01° 2θ.

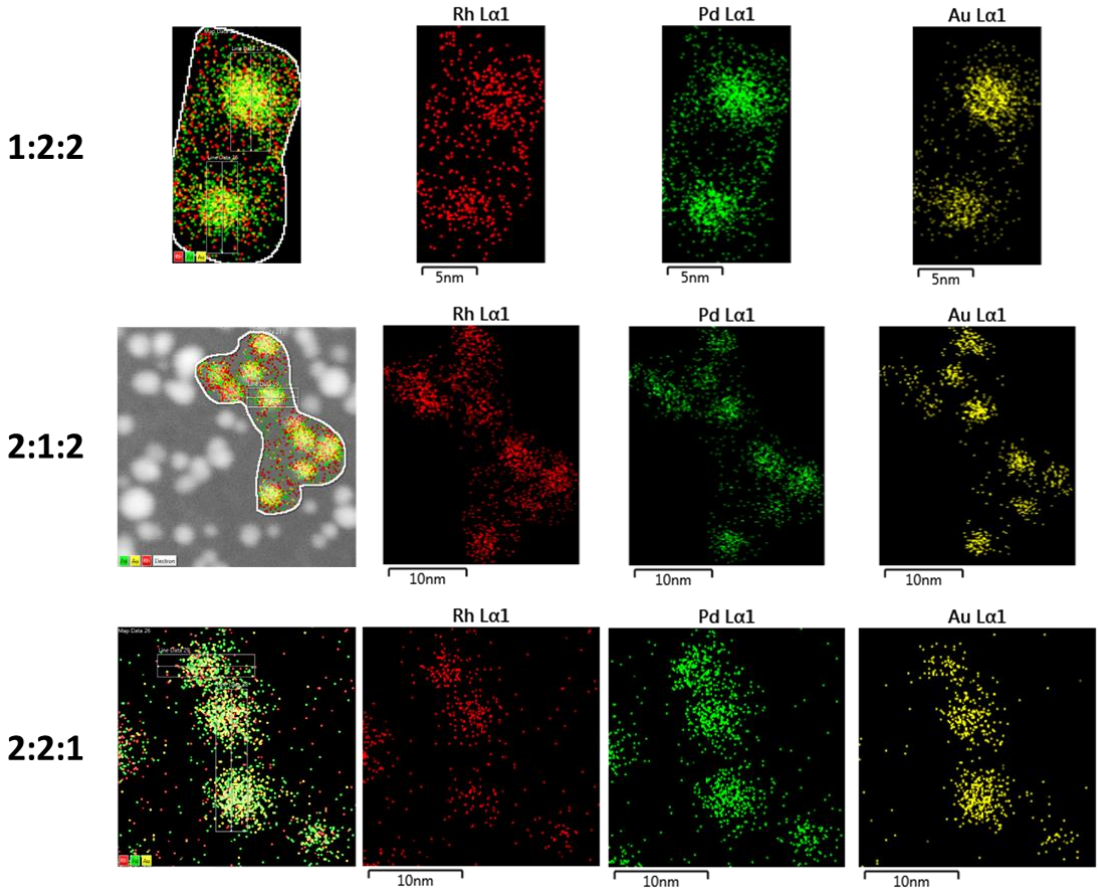

Figure 4.8. EDS maps of the 1:2:2, 2:1:2, and 2:2:1 compositions, including overlay spectra (far left) and individual elemental maps.

X-ray Photoelectron Spectroscopy

X-ray photoelectron spectroscopy (XPS) spectra were collected using a Kratos Axis Ultra Photoelectron Spectrometer, which employs a monochromated Al Kα X-ray source (1486.5 eV), hybrid optics (i.e., using both magnetic and electrostatic lenses) and a multi-channel plate coupled to a hemispherical photoelectron kinetic analyzer. The samples used in the analysis were prepared by drop-casting a concentrated solution of the PVP-capped nanoparticles onto clean glass plates measuring *ca.* 5 mm on each side; these solutions were allowed to air dry, and additional solution was drop-cast until the top of

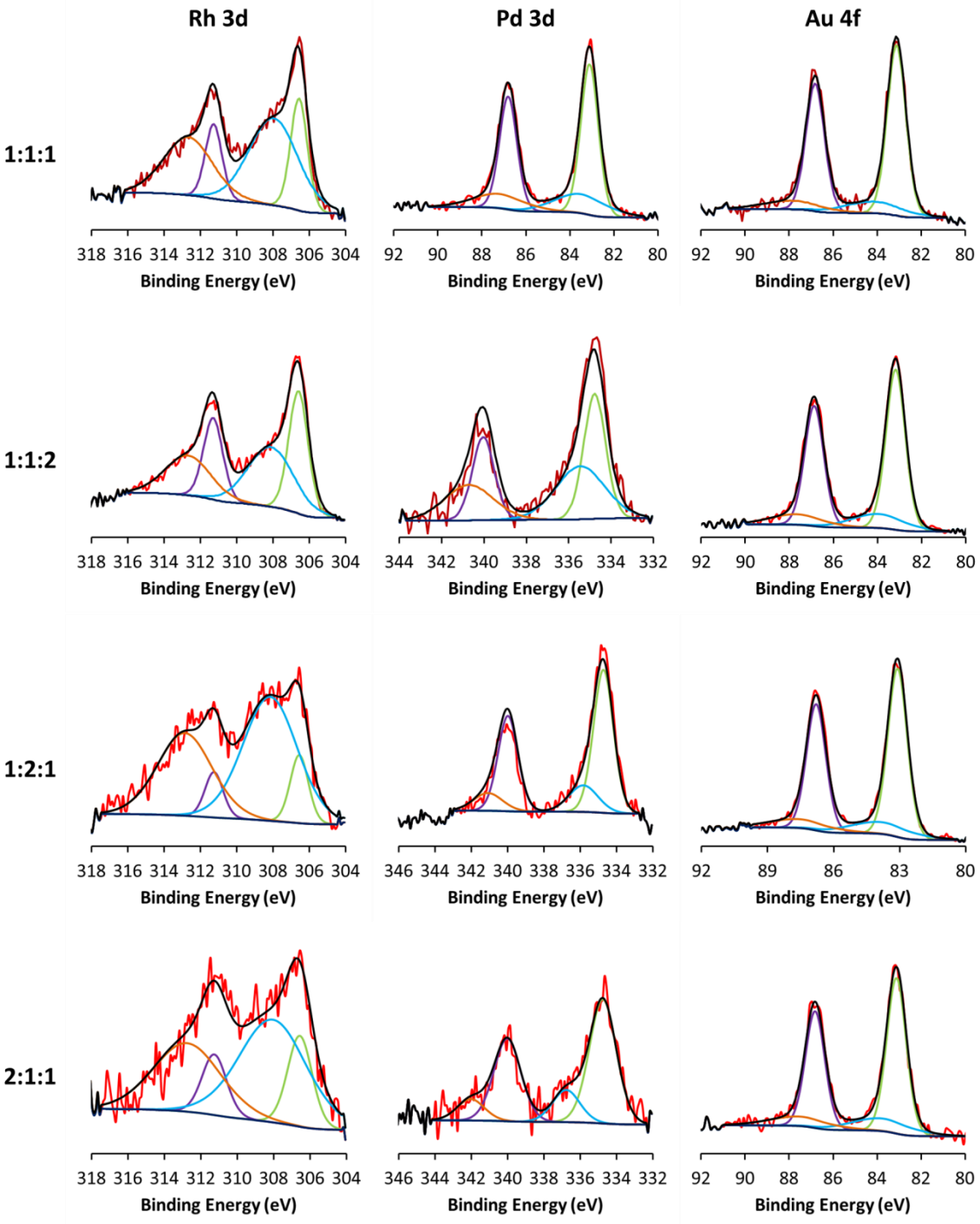

Figure 4.9. Rh 3d, Pd 3d, and Au 4f regions of the XPS spectra of the 1:1:1, 1:1:2, 1:2:1, 2:1:1 compositions.

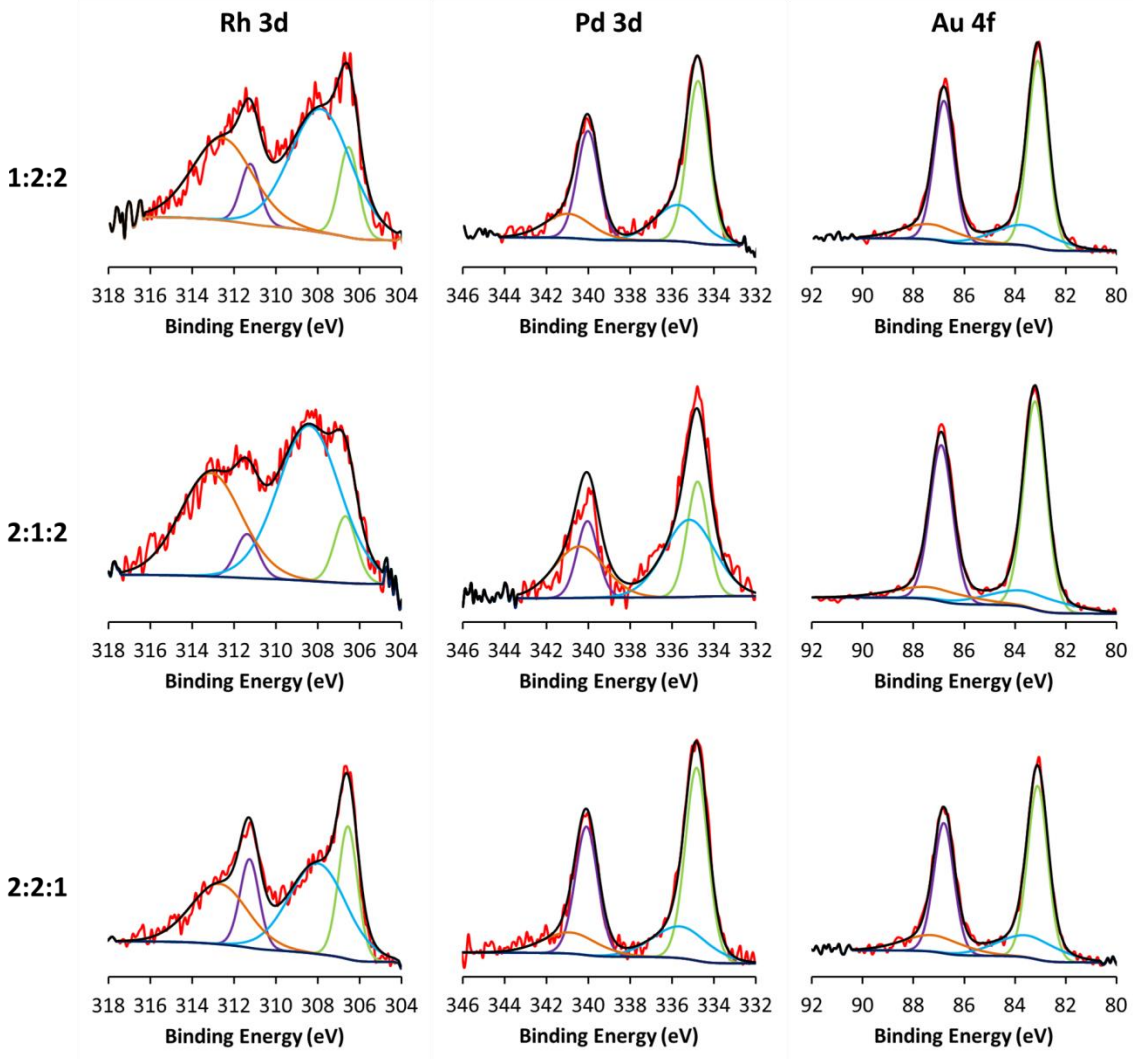

Figure 4.10. Rh 3d, Pd 3d, and Au 4f regions of the XPS spectra of the 1:2:2, 2:1:2, 2:2:1, 2:1:1 compositions.

the slide appeared dark. Spectra were recorded with a pass energy of 20 eV, a step size of 0.1eV, an aperture slot of 300 x 700 μm, dwell times of 2000 – 2500 ms, and four sweeps so the data could be averaged. To minimize sample charging and any resulting band distortion, a Kratos charge neutralizer (20 eV electrons) was used and the sample stage was left ungrounded. Casa XPS analysis software was used for peak deconvolution

and the corrected peak areas were used in conjunction with the appropriate Kratos sensitivity factors for each element to determine the stoichiometry of the sample.

Synthesis of RhPdAg Nanobeads

RhPdAg nanobeads were synthesized using a modified version of the method reported by García, *et al*.[4] $RhCl_3 \cdot xH_2O$, K_2PdCl_4, and $AgNO_3$ were weighed out into separate scintillation vials; the masses were determined based on the intended mole ratio and the total number of moles of metal (0.095 mmol). Each precursor was dissolved separately in ethylene glycol. The Rh and Pd precursor solutions (1.25 mL total) were then loaded into a single 10 mL syringe, while the Ag precursor solution (1.25 mL) was loaded into a separate syringe to prevent precipitation of AgCl before the reaction. Meanwhile, 200 mg of PVP was dissolved in 15 mL of ethylene glycol in a 50 mL round-bottom flask. A magnetic stir bar was added to the flask, and the flask was attached to a water-cooled reflux condenser inside a CEM MARS 5 programmable microwave chamber. The syringe with the precursor solution was loaded into a programmable syringe pump. PTFE tubing was threaded down the condenser into the round-bottom flask and secured to the syringe needle with PTFE tape. Once the PVP solution had been heated to 150 °C (6 min ramp), the precursor solution was injected at 300 mL h^{-1}. Once the injection was complete, the solution was stirred at 150 °C for 30 min before the flask was transferred to an ice bath to quench the reaction. Once the solution was cold, it was evenly distributed between two 50 mL centrifuge tubes. Each half was diluted to 40 mL with acetone and centrifuged at 5500 rpm for 5 min to precipitate the nanoparticles. The clear supernatant was discarded. The dark, viscous fluid containing the nanoparticles was dispersed in 5 mL of ethanol per tube with the aid of sonication. The particles were re-

precipitated by adding 30 mL of hexanes to each tube and centrifuging at 5500 rpm for 5 min. After discarding the supernatant, the nanoparticle-containing fluid was dispersed in 10 mL of DI water and 1 mL of concentrated ammonia was added to each tube to dissolve any AgCl. The tubes were agitated briefly, then centrifuged at 5500 rpm for 5 min. The aqueous supernatant was discarded, and the ethanol-hexanes wash was performed once more. The product was dried in a vacuum desiccator overnight to yield a black film.

Synthesis of RhPdAu Nanoparticles

RhPdAg nanobeads were also synthesized using a modified version of the method reported by García, *et al*.[4] $RhCl_3 \cdot xH_2O$, K_2PdCl_4, and $HAuCl_4$ were weighed out into separate scintillation vials; the masses were determined based on the intended mole ratio (1:1:1, 2:1:1, 1:2:1, 1:1:2, 1:2:2, 2:1:2, or 2:2:1) and the total number of moles of metal (0.095 mmol). Each precursor was dissolved separately in ethylene glycol, then loaded into a single 10 mL syringe. Meanwhile, 200 mg of PVP was dissolved in 15 mL of ethylene glycol in a 50 mL round-bottom flask. A magnetic stir bar was added to the flask, and the flask was attached to a water-cooled reflux condenser inside a CEM MARS 5 programmable microwave chamber. The syringe with the precursor solution was loaded into a programmable syringe pump. PTFE tubing was threaded down the condenser into the round-bottom flask and secured to the syringe needle with PTFE tape. Once the PVP solution had been heated to 150 °C (6 min ramp), the precursor solution was injected at 300 mL h^{-1}. Once the injection was complete, the solution was stirred at 150 °C for 30 min before the flask was transferred to an ice bath to quench the reaction. Once the solution was cold, it was evenly distributed between two 50 mL centrifuge

tubes. Each half was diluted to 40 mL with acetone and centrifuged at 5500 rpm for 5 min to precipitate the nanoparticles. The clear supernatant was discarded. The dark, viscous fluid containing the nanoparticles was dispersed in 5 mL of ethanol per tube with the aid of sonication. The particles were re-precipitated by adding 30 mL of hexanes to each tube and centrifuging at 5500 rpm for 5 min. This ethanol-hexanes wash was performed a total of two times. The product was dried in a vacuum desiccator overnight to yield a black film.

REFERENCES

1. R. Ferrando, J. Jellinek, R. L. Johnston, *Chem. Rev.* **2008**, *108*, 845-910.
2. M. B. Cortie, A. M. McDonagh, *Chem. Rev.* **2011**, *111*, 3713-3735.
3. K. Kusada, H. Kobayashi, R. Ikeda, Y. Kubota, M. Takata, S. Toh, T. Yamamoto, S. Matsumura, N. Sumi, K. Sato, K. Nagaoka, H. Kitagawa, *J. Am. Chem. Soc.* **2014**, *136*, 1864-1871.
4. S. García, L. Zhang, G. W. Piburn, G. Henkelman, S. M. Humphrey, *ACS Nano*, **2014**, *8*, 11512-11521.
5. H. Kobayashi, K. Kusada, H. Kitagawa, *Acc. Chem. Res.* **2015**, *48*, 1551-1559.
6. F.-J. Lai, L. S. Sarma, H.-L. Chou, D.-G. Liu, C.-A. Hsieh, J.-F. Lee, B.-J. Hwang, *J. Phys. Chem C* **2009**, *113*, 12674-12681.
7. W. Tang, L. Zhang, G. Henkelman, *J. Phys. Chem. Lett.* **2011**, *2*, 1328-1331.
8. D. Wang, H. L. Xin, H. Wang, Y. Yu, E. Rus, D. A. Muller, F. J. DiSalvo, H. D. Abruña, *Chem. Mater.* **2012**, *24*, 2274-2281.
9. P. Kunal, H. Li, B. L. Dewing, L Zhang, K. Jarvis, G. Henkelman, and S. M. Humphrey, *ACS Catal.* **2016**, *6*, 4882-4893.
10. S.-H. Tsai, Y.-H. Liu, P.-L. Wu, C.-S. Yeh, *J. Mater. Chem.* **2003**, *13*, 978-980.
11. Z.-L. Wang, Y. Ping, J.-M. Yan, H.-L. Wang, Q. Jiang, *Int. J. Hydrogen Energy* **2014**, 4850-4856.
12. H. Zhang, Y. Cao, L. Lu, Z. Cheng, S. Zhang, *Metall. Mater. Trans. B* **2015**, *46B*, 523-530.

13. Q. He, P. J. Miedziak, L. Kesavan, N. Dimitratos, M. Sankar, J. A. Lopez-Sanchez, M. M. Forde, J. K. Edwards, D. W. Knight, S. H. Taylor, C. J. Kiely, G. J. Hutchings, *Faraday Discuss.* **2013**, *162*, 365-378.

14. H. Zhang, L. Lu, Y. Cao, S. Du, Z. Cheng, S. Zhang, *Mater. Res. Bull.* **2014**, *49*, 393-398.

15. S. García, R. M. Anderson, H. Celio, N. Dahal, A. Dolocan, J. Zhou, S. M. Humphrey, *Chem. Commun.* **2013**, *39*, 4241-4243.

16. Y. Xiong, J. Chen, B. Wiley, Y. Xia, *J. Am. Chem. Soc.* **2005**, *127*, 7332-7333.

Chapter Five: Selective Hydrogenation by Rh Nanoparticles on Co_3O_4

Rhodium nanoparticles were supported on Co_3O_4 to replicate results indicating that the combination could achieve highly selective hydrogenation of crotonaldehyde to produce crotyl alcohol. Catalytic tests of Rh nanoparticles on amorphous Co_3O_4 resulted in almost exclusive production of butanal instead, although crotyl alcohol selectivity did rise somewhat upon reactivation of the catalyst. These results demonstrate the likely critical role played by the mesoporosity of the original support. Efforts to produce a mesoporous Co_3O_4 support to complete replication of the study are ongoing.

INTRODUCTION

In the previous two chapters, the study of hydrogenation catalysis by noble metal nanoparticles was focused on the hydrogenation of cyclohexene, a simple alkene. However, most industrially important molecules have multiple functional groups. It is therefore important to be able to conduct catalytic reactions in a selective way, such that the majority of the product results from reaction with the intended group. In this chapter, the examination of hydrogenation catalysis will be extended to α,β-unsaturated aldehydes, which will be modeled using crotonaldehyde (2-butenal).

Crotonaldehyde is a small organic molecule which is a liquid a room temperature. Its vapor pressure is less than a third of that of cyclohexene at room temperature, so a higher temperature must be maintained in any catalytic system to ensure that it stays in the gas phase. Industrially, crotonaldehyde is mostly used as a precursor to more complex chemicals, such as the preservative sorbic acid or vitamin E.[1] Crotonaldehyde is classified as "highly toxic" by the National Fire Protection Association, so care must be taken to minimize exposure both to the liquid and to its vapors; in this study, the gas flow

eluting from the GC was passed through a room-temperature water bubbler to pick up unreacted crotonaldehyde vapors and avoid excessive risk to nearby researchers.

As an unsaturated aldehyde, crotonaldehyde contains two groups that can be hydrogenated: the aldehyde group and an alkene group. Whereas the electron density in the alkene bond is distributed symmetrically, the carbonyl group is highly polarized, with the majority of the electron density residing around the more electronegative oxygen atom. As a result, carbonyl groups tend to bind to metal surfaces and organometallic catalysts oxygen-first, an orientation that does not readily expose the double bond to hydrogenation; the hydrogenation of the alkene bond is therefore favored both kinetically and thermodynamically on most noble metal surfaces.[2] Ultimately, this means that unsaturated aldehydes and ketones are more likely to undergo hydrogenation of their carbon-carbon double bonds than their carbon-oxygen double bonds. However, this is not usually the industrially desired outcome, since hydrogenation of an alkene yields an alkane that is chemically unreactive under most circumstances, whereas hydrogenation of a carbonyl leaves a versatile alcohol group. Of course, there is also the risk of over-hydrogenation to form the saturated alcohol if either of the initial products remains in the presence of the catalyst for too long. To further complicate matters, catalysts that can hydrogenate crotonaldehyde can generally also decarbonylate it, forming propene and carbon monoxide. Crotyl alcohol can even be converted to butenal under the wrong conditions. The full range of possibilities is laid out in Scheme 5.1. Given these complexities, the goal of the selective hydrogenation of crotonaldehyde to produce a new molecule (crotyl alcohol) that still has two useful functional groups that can contribute to further reactions is not a trivial challenge.

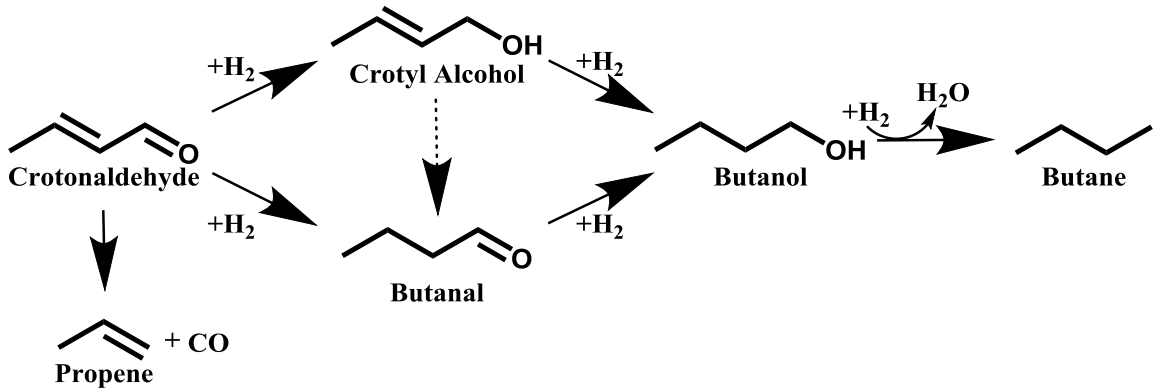

Scheme 5.1. Reaction pathways for crotonaldehyde in the presence of a hydrogenation catalyst.

Nevertheless, a number of catalytic systems have been able to achieve selectivities higher than 50% for crotyl alcohol.[2-18] This selectivity typically comes at the cost of reactivity.[6] For example, the industrial standard for this reaction is a catalyst made of gold nanoparticles supported on TiO_2. Gold is not used as a general-purpose hydrogenation catalyst because of its inability to dissociate hydrogen spontaneously at room temperature; though coordinatively unsaturated sites at the edges of gold particles can dissociate a small amount of hydrogen at higher temperatures.[3] The first major exploration of gold as a catalyst for the selective hydrogenation of crotonaldehyde was performed by Baillie and Hutchings in the late 1990s, who found that at 250 °C, thiophene-modified gold nanoparticles on ZnO could give crotyl alcohol selectivities as high as 65%.[7] This selectivity was attributed to the ability of interfacial sites between the hemispherical nanoparticles and the oxide support to guide crotonaldehyde into an orientation that would promote the hydrogenation of the carbonyl bond.

Numerous combinations of noble metals and metal oxide supports have been applied to this reaction since the 1990s to try to achieve high selectivity. Although the

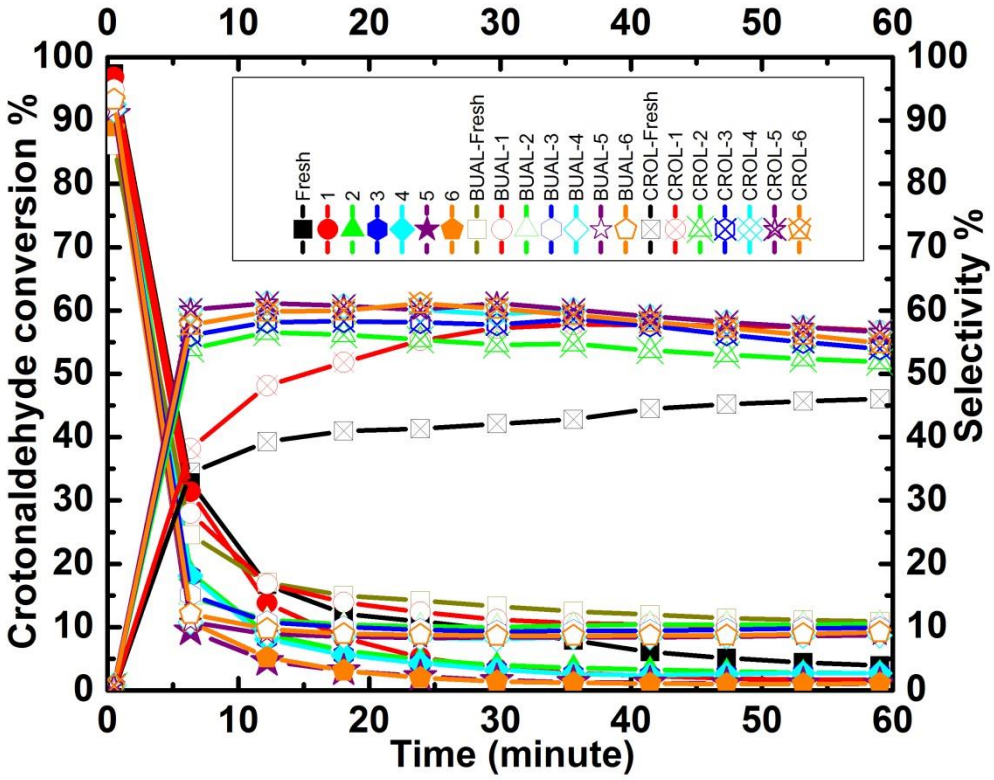

Figure 5.1. Catalytic data collected by Naween Dahal showing excellent selectivity for crotyl alcohol and robust recyclability.

exact reason why gold exhibits superior selectivity to other noble metals is not well understood, investigations into supported noble metal nanoparticles suggest that a variety of factors can contribute, including the identity of the metal,[6] selective poisoning,[7-9] metal oxide supports that modify the electronic properties of the metal or encourage C=O binding near the metal-support interface,[6,10-13] decoration of the catalyst surface with groups that activate the C=O bond,[9,14-18] and more. Porous supports have been used occasionally, though in the absence of bulky groups on the substrate molecule,[2] they do not consistently drive the selectivity of the catalyst in one direction or another.[11,19-20]

Approximately 6 years ago, Dr. Naween Dahal, then of the Humphrey Group, discovered that the combination of small rhodium nanoparticles with mesoporous Co_3O_4

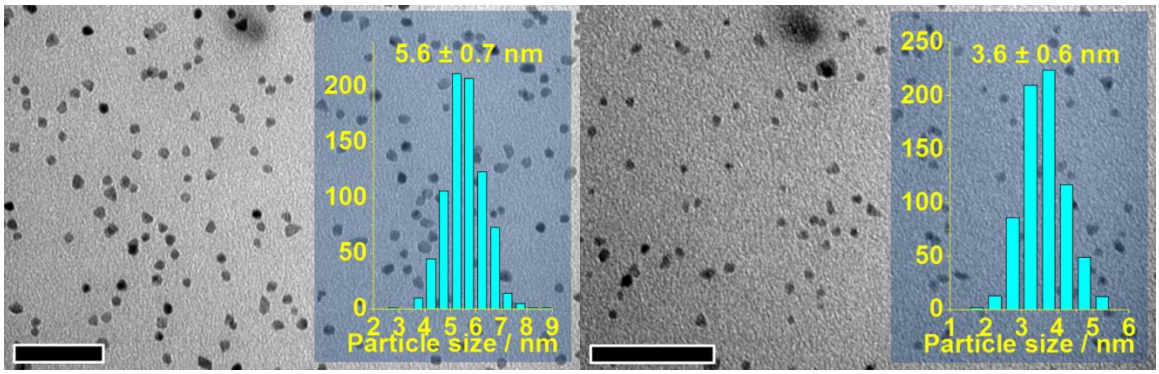

Figure 5.2. TEM images and size distributions of two different sizes of Rh nanoparticles.

led to crotyl alcohol selectivity near 50% with high recyclability (Figure 5.1). This is significant because rhodium alone has, at best, modest selectivity for crotyl alcohol.[16,17] The purpose of the project described here is to reproduce these findings and better understand the factors that contribute to this excellent selectivity.

RESULTS AND DISCUSSION

Preliminary Results

The first step toward making the desired catalyst was to synthesize rhodium nanoparticles using the method described by Dahal, *et al*.[21] The nanoparticles used in the previous study had been *ca.* 3.5 nm in diameter, so the reaction time was kept short (30 s) to prevent the smaller seed particles from growing or coalescing into larger particles. For comparison, larger rhodium nanoparticles were also produced by using a longer reaction time (30 min) but otherwise the same method. TEM imaging (Figure 5.2) confirmed that both nanoparticle samples had narrow size distributions around the expected average diameters.

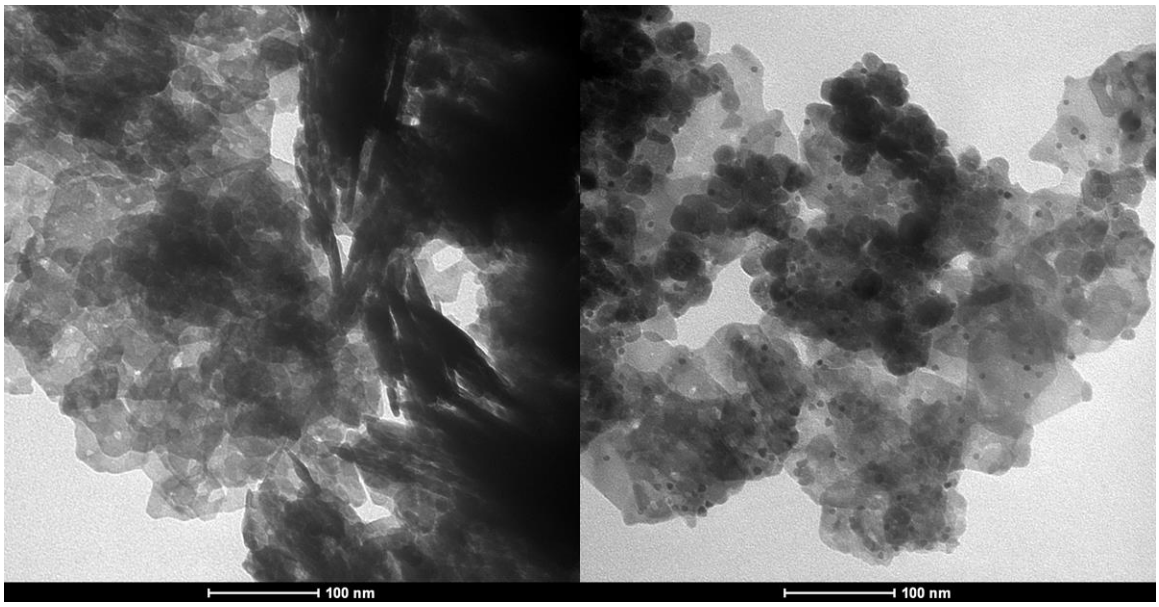

Figure 5.3. TEM images of amorphous Co_3O_4 (left) and 6 nm Rh particles loaded on Co_3O_4 (right).

The production of mesoporous cobalt oxide, the support used in the previous studies, proved more challenging. The procedures used were those described by Dahal, *et al.*,[22] starting with the soft-template method. The pH was adjusted to 12.7 with 1.0 M HCl before the cobalt nitrate was added, but the color of the solution did not consistently change as described. In most cases, several more milliliters of 1.0 M NaOH needed to be added before the solution was alkaline enough to begin converting Co(II) to Co(III) and ultimately gelling ions of both oxidation states around the Pluronic P-123 template. Despite this adjustment, the eventual product failed to demonstrate any ordered porous structure by TEM (Figure 5.3). The hard-template synthesis from the same paper has also been attempted; however, despite using good quality SBA-15 and CMK-3, the no appreciable yield of Co_3O_4 has been obtained using this method, let alone mesoporous material in the quantities reported. At the time of writing, neither route has produced

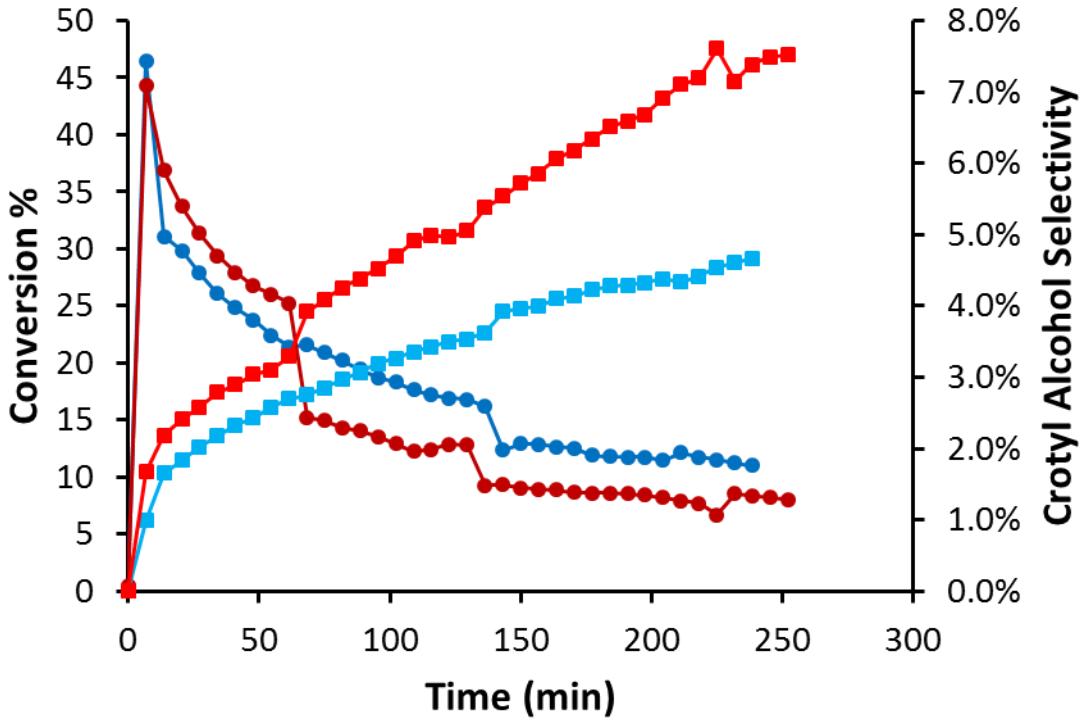

Figure 5.4. Total crotonaldehyde conversion (circles) and crotyl alcohol selectivity (squares) for Co_3O_4-supported Rh nanoparticles with diameters of 5.6 nm (blue) and 3.6 nm (red).

mesoporous material, so all the Co_3O_4 used for the following catalytic studies is amorphous Co_3O_4 produced by the soft-template route.

Rhodium nanoparticles with diameters of 3.5 nm and 5.5 nm were separately supported on amorphous Co_3O_4. The catalysts were activated before use on the catalysis line at 300 °C overnight under a flow of H_2/He gas to hydrogenate away the PVP capping agent and remove any impediments to crotonaldehyde reaching the nanoparticle surface. The catalytic study was carried out at 100 °C to prevent condensation of the crotonaldehyde vapors.

Notable catalysis results are presented in Figures 5.4 and 5.5. Little difference was found between overall reactivities of the two sizes of rhodium nanoparticles, but the

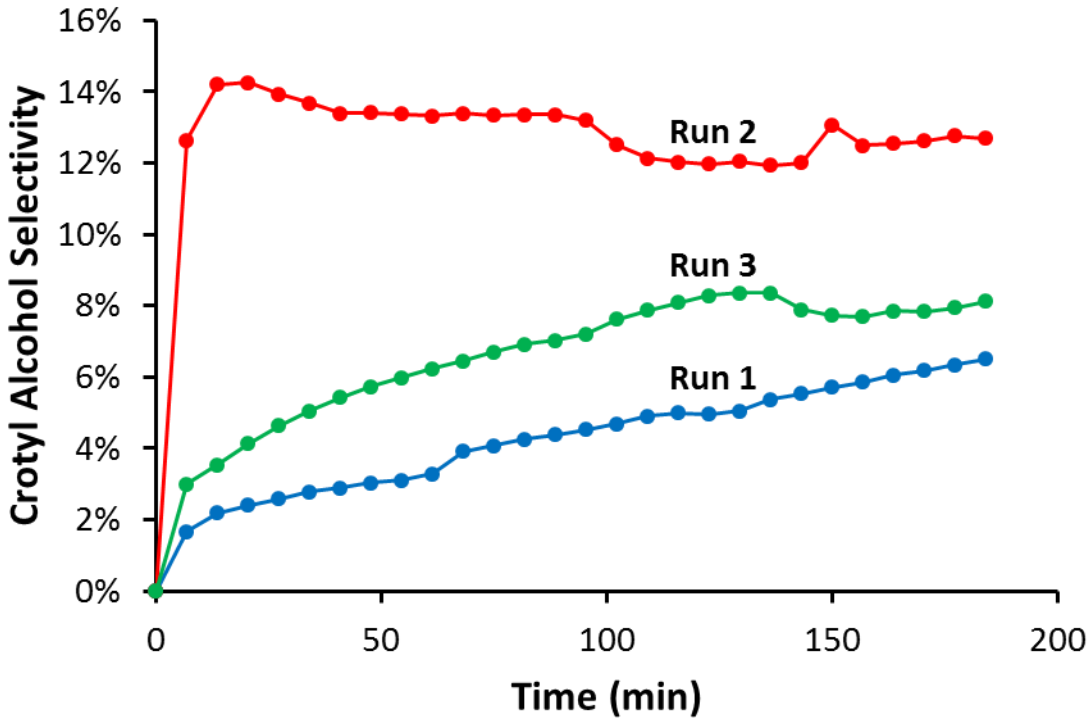

Figure 5.5. Selectivity for crotyl alcohol over the course of the recyclability study using 3.6 nm Rh nanoparticles on Co_3O_4.

smaller nanoparticles did achieve a higher selectivity toward crotyl alcohol (Figure 5.4). However, both catalysts displayed less than 10% selectivity for the desired product. This appears to be a clear indication that the mesoporosity of the support played a crucial role in the unexpected reactivity of the previously studied material. In the previous work, the selectivity of the catalyst improved slightly upon reactivation and remained consistent forseveral more cycles, so a recyclability study was performed to test whether the selectivity would improve for this system as well (Figure 5.5). Although the selectivity toward crotyl alcohol did improve during the second run, peaking near 15%, this gain was not sustained by the next cycle, which demonstrated selectivity no higher than 9%.

All in all, none of the conditions tested thus far achieved the 50% selectivity reported for the mesoporous system.

Future Goals

Given the apparent necessity of a mesoporous support, the synthesis of mesoporous Co_3O_4 with wide enough pores for 3.5 nm particles to fit inside is a top priority. The clearest route to this goal appears to be the hard-template synthesis, since modifying the soft-template method could require significant reworking of the synthetic conditions. The key problem with the hard-template method as it stands is the inability to sufficiently load cobalt nitrate into the CMK-3 template using the described procedure. This is not especially surprising considering that CMK-3 is a nonpolar mesoporous carbon, and the prescribed procedure calls for loading the template by stirring it in a refluxing, aqueous solution of the cobalt salt. To improve loading of the template, the surface of the CMK-3 will be modified to create surface carbonyl groups that can effectively bind the precursor salts, and the loading step will be done in a less polar solvent like THF to encourage interaction with the template rather than the solvent.[23] Once suitable mesoporous Co_3O_4 is obtained, it will be loaded with 3.5 nm Rh nanoparticles, and the catalytic studies will be repeated. This material should accurately replicate the exceptional material in the previous study by Dahal, and so it is expected to show similarly exceptional selectivity.

EXPERIMENTAL DETAILS

General

Rh nanoparticles were synthesized using the polyol method, utilizing $RhCl_3 \cdot xH_2O$ (Strem Chemicals, 38-41% Rh) as the metal precursor, poly(vinylpyrrolidone) (PVP; Alfa Aesar, MW = 58K, ~18 mol monomer/mol metal) as the capping agent, and ethylene glycol (Fischer Scientific, 99.8%) as the solvent and reducing agent. Co_3O_4 was synthesized using $Co(NO_3)_2 \cdot 6H_2O$ (Strem Chemicals, 99%), Pluronic P-123 (Aldrich; M.W. = 5,800), *n*-decane (Alfa Aesar; ≥99%), NH_4F (Alfa Aesar; 96%), and NaOH (Aldrich; ≥98%), and hydrochloric acid (Fisher; 12 M). These chemicals and all other solvents (analytical grade) were used as received. The microwave reactor was set up as described in Chapter 4. The pH of the Co_3O_4 was monitored using a Mettler Toledo SevenEasy pH meter with a three-point calibration.

Electron Microscopy

Transmission electron microscopy (TEM) images were produced using an FEI Technai microscope with an operating potential of 80 kV. Samples were prepared by drop-casting a dilute solution of nanoparticles in ethanol onto 200 mesh Cu/Formvar grids (Ted Pella, Inc.) and allowing the grid to air dry. The diameters of the nanoparticles were found by using the line tool in Image-J (http://rsbweb.nih.gov/ij) to measure the shortest distance across each particle that included the center of the particle. Over 300 particles across at least two images from different grid coordinates were measured for each set of reaction conditions.

X-ray Powder Diffraction

X-ray powder diffraction was performed using a Rigaku R-Axis Spider with a Cu Kα source (1.5418 Å) operating at 40 kV and 40 mA. X-ray spectra were collected using a sample rotation speed of 10° s^{-1} and a step width of 0.01° 2θ.

Synthesis of Rh Nanoparticles

Rh nanoparticles were synthesized using a version of the method reported by Dahal, *et al.*[21] 20 mg of $RhCl_3 \cdot xH_2O$ was dissolved in 2.5 mL of ethylene glycol in a scintillation vial. The precursor solution was then loaded into a 10 mL syringe. Meanwhile, 200 mg of PVP was dissolved in 15 mL of ethylene glycol in a 50 mL round-bottom flask. A magnetic stir bar was added to the flask, and the flask was attached to a water-cooled reflux condenser inside a CEM MARS 5 programmable microwave chamber. The syringe with the precursor solution was loaded into a programmable syringe pump. PTFE tubing was threaded down the condenser into the round-bottom flask and secured to the syringe needle with PTFE tape. Once the PVP solution had been heated to 150 °C (6 min ramp), the precursor solution was injected at 300 mL h^{-1}. Once the injection was complete, the solution was stirred at 150 °C for 30 s before the flask was transferred to an ice bath to quench the reaction. Once the solution was cold, it was evenly distributed between two 50 mL centrifuge tubes. Each half was diluted to 40 mL with acetone and centrifuged at 5500 rpm for 5 min to precipitate the nanoparticles. The clear supernatant was discarded. The dark, viscous fluid containing the nanoparticles was dispersed in 5 mL of ethanol per tube with the aid of sonication. The particles were re-precipitated by adding 30 mL of hexanes to each tube and centrifuging at 5500 rpm for 5 min. This ethanol-hexanes wash was performed a total of two times. The product was dried in a vacuum desiccator overnight to yield a black film.

Synthesis of Co_3O_4

The Co_3O_4 used in the catalytic studies presented in this chapter was made by the soft-template method described by Dahal, *et al*.[22] Pluronic-P123 (2.43 g) was measured into a 400 mL beaker, where it was dissolved in a 0.5 M NaOH solution (1:1 ethanol:water). A catalytic amount of NH_4F (0.028 g) was added once the surfactant had dissolved. The pH of the solution was adjusted to 12.7 with 1 M HCl; this process was tracked by a pH meter, and the solution was stirred throughout the process. Then, *n*-decane (15 mL) was added slowly by pipette, and the mixture was allowed to stir for 30 min while the decane was incorporated into the surfactant micelles. The cobalt precursor, $Co(NO_3)_2 \cdot 6H_2O$ (0.82 g), was delivered to the reaction vessel dissolved in 6 mL of ethanol. If the solution did not immediately turn blue, then green over the course of ten minutes, as prescribed, then 2 mL aqueous 1 M NaOH was added every few minutes until the color turned green-brown. The reaction solution was stirred at 35 °C for 20 h, eventually turning dark brown; it was then transferred to a 250 mL Nalgene bottle sealed with PTFE tape and heated in an oven at 82 °C for 48 h. The resulting solid was isolated by centrifugation because it was too fine to be effectively filtered. The solid was then calcined at 400 °C (ramp rate 1.0 °C min^{-1}) in a box furnace for 5 h to burn away the polymer template and anneal the Co_3O_4 product.

Catalyst Preparation

Rh nanoparticles were supported on Co_3O_4 by first wetting 500 mg amorphous Co_3O_4 with a small amount of 1:1 ethanol:water in a 20 mL scintillation vial. The entirety of the film produced by a single Rh nanoparticle synthesis was added to the vial,

and the total volume of ethanolic water was brought up to 10 mL. The nanoparticle film was dispersed by sonication, then sonicated an additional 30 min before a magnetic stir bar was added and the mixture was stirred overnight. Afterward, the stir bar was removed, and the solid product was isolated by filtration and dried overnight in an oven at 80 °C.

Catalysis Studies

For each catalytic trial, about 5 mg of previously prepared Rh-Co_3O_4 composite was thoroughly mixed with 125 mg of acid-washed, calcined sand and loaded into a custom-made quartz U-tube, resting on a D3-porosity frit. The catalyst was activated by heating it at 300 °C overnight under flowing H_2/He (1:1); this temperature was decreased to 100 °C before the crotonaldehyde was introduced to the line. The in-line, fritted crotonaldehyde bubbler was held at 0 °C by an ice bath, and the rest of the quartz reactor line was heated to 90 °C with heating tape. After taking several initial data points, crotonaldehyde vapor was introduced into the reactant gas mixture, initiating the catalysis trial. Data was collected *via* automated, pneumatically gated sampling of the exhaust stream into an HP Agilent 6890 GC with a 15 m Restek Stabilwax column and tandem FID and TCD detectors. Collection was continued for 6 h. A full diagram of the catalysis line setup can be found in Chapter 3.

REFERENCES

1. D. Castagnolo, L. Botta, M. Botta, *J.Org. Chem.* **2009**, *74*, 3172-3174.
2. P. Claus, *Top. Catal.* **1998**, *5*, 51-62.
3. P. Claus, *Appl. Catal. A* **2005**, *291*, 222-229.

4. L. McEwan, M. Julius, S. Roberts, J. C. Q. Fletcher, *Gold Bull.* **2010**, *43*, 298-306.

5. G. J. Hutchings, *Catal. Today* **2008**, *138*, 9-14.

6. R. Zanella, C. Louis, S. Giorgio, R. Touroude, *J. Catal.* **2004**, *223*, 328-339.

7. J. E. Bailie, G. J. Hutchings, *Chem. Commun.* **1999**, *21*, 2151-2152.

8. M. E. Chiu, D. J. Watson, G. Kyriakou, M. S. Tikhov, R. M. Lambert, *Angew. Chem. Int. Ed.* **2006**, *45*, 7530-7534.

9. Y. K. Du, J. Z. Xu, P. Yang, N. P. Hua, L. Jiang, *Coll. Surf. A* **2005**, 257-258, 75-78.

10. M. Englisch, A. Jentys, J. A. Lercher, *J. Catal.* **1997**, *166*, 25-35.

11. P. Reyes, M. C. Aguirre, G. Pecchi, J. L. G. Fierro, *J. Molec. Catal. A* **2000**, *164*, 245-251.

12. G. Kennedy, L. R. Baker, G. A. Somorjai, *Angew. Chem. Int. Ed.* **2014**, *53*, 3405-3408.

13. G. Kennedy, G. Melaet, H.-L. Han, W. T. Ralston, G. A. Somorjai, *ACS Catalysis* **2016**, *6*, 7140-7147.

14. D. I. Jerdev, A. Olivas, B. E. Koel, *J. Catal.* **2002**, *205*, 278-288.

15. F. Ammari, C. Milone, R. Touroude, *J. Catal*. **2005**, *235*, 1-9.

16. P. Reyes, M. C. Aguirre, J. L. G. Fierro, G. Santori, O. Ferretti, *J. Molec. Catal. A* **2002**, *184*, 431-441.

17. P. Reyes, G. Pecchi, J. L. G. Fierro, *Langmuir* **2001**, *17*, 522-527.

18. M. C. Aguirre, J. L. G. Fierro, P. Reyes, *React. Kinet. Catal. Lett.* **2005**, *84*, 351-358.

19. M. Chatterjee, Y. Ikushima, Y. Hakuta, H. Kawanami, *Adv. Synth. Catal.* **2006**, *348*, 1580-1590.

20. M. E. Grass, R. M. Rioux, G. A. Somorjai, *Catal. Lett.* **2009**, *128*, 1-8.

21. N. Dahal, S. García, J. Zhou, S. M. Humphrey, *ACS Nano* **2012** *6*, 9433-9446.

22. N. Dahal, I. A. Ibarra, S. M. Humphrey, *J. Mater. Chem.* **2012**, *22*, 12675-12681.

23. J. Roggenbuck, T. Waitz, M. Tiemann, *Micropor. Mesopor. Mat.* **2008**, *113*, 575-582.

References

CHAPTER ONE

1. F. J. Heiligtag, M. Niederberger *Mater. Today* **2013**, *16*, 262-271.
2. M. Magnani, L. Galluzzi, I. J. Bruce *J. Nanosci. Nanotechnol.* **2006**, *6*, 2302-2311.
3. S. Morneta, S. Vasseura, F. Grassteb, P. Veverkac, G. Goglioa, A. Demourguesa, J. Portiera, E. Pollertc, E. Duguet *Prog. Solid State Chem.* **2006**, *34*, 237-247.
4. T. Kim, D. S. Kim, B. Y. Lee, Z. H. Kim, S. Hong *Adv. Mater.* **2009**, *21*, 1238-1242.
5. L. Z. Zhang, G. Q. Tang *Opt. Mater.* **2004**, *21*, 217-220.
6. Y. Sun, G. P. Wiederrecht *Small* **2007**, *3*, 1964-1975.
7. M. C. Daniel, D. Astruc *Chem. Rev.* **2004**, *104*, 293-346.
8. A. Roucoux, J. Schultz, H. Patin *Chem. Rev.* **2002**, *102*, 3757-3778.
9. Y. Volokitin, J. Sinzing, L. J. de Jong, G. Schmid, M. N. Vargaftik, I. I. Moiseev *Nature* **1996**, *384*, 621-623.
10. S. Eustis, M. A. El-Sayed, *Chem. Soc. Rev.* **2006**, *35*, 209-217.
11. C. J. Murphy, N. R. Jana *Adv. Mater.* **2002**, *14*, 80-82.
12. D. Astruc, F. Lu, J. R. Aranzaes *Angew. Chem. Int. Ed.* **2005**, *44*, 7852-7872.
13. W. Zang, G. Li, L. Wang, X. Zhang *Catal. Sci. Technol.* **2015**, *5*, 2532-2553.
14. L. Shen, N. Bao, K. Yanagisawa, K. Domen, A. Gupta, C. Grimes *Nanotechnology* **2006**, *17*, 5117-5123.
15. J. S. Wang, S. Yin, M. Komatsu, Q. W. Zhang, F. Saito, T. Sato *Appl. Catal. B* **2004**, *52*, 11-21.
16. T. Tuval, A. Gedanken *Nanotechnology* **2007**, *18*, 255601.
17. J. M. Campelo, T. D. Conesa, M. J. Gracia, M. J. Jurado, R. Luque, J. M. Marinas, A. A. Romero *Green Chem.* **2008**, *10*, 853-858.
18. E. Rogemond, N. Essayem, R. Frety, V. Perrichon, M. Primet, F. Mathis *J. Catal.* **1997**, *166*, 229-235.
19. Y. Sugiura, D. Mukai, Y. Murai, S. Tochiya, Y. Sekine *J. Hypdrogen Energy* **2013**, *38*, 7822.
20. P. Zhang, S.-Y. Huang, B. N. Popov *J. Electrochem. Soc.* **2010**, *157*, B1163-B1172.
21. S. Campisi, M. Schiavoni, C. E. Chan-Thaw, A. Villa *Catalysts* **2016**, *6*, 185.

22. I. Ojea-Jiménez, J. M. Campanera *J. Phys. Chem. C* **2012**, *116*, 23682-23691

23. F. Fievet, J. P. Lagier, M. Figlarz *MRS Bull.* **1989**, *14*, 29-34.

24. F. Fievet, J. P. Lagier, B. Blin, B. Beaudoin, M. Figlarz *Solid State Ionics* **1989**, *32-33*, 198-205.

25. C. Burda, X. Chen, R. Narayanan, M. A. El-Sayed *Chem. Rev.* **2005**, *105*, 1025-1102.

26. P. Strasser, S. Koh, T. Anniyev, J. Greeley, K. More, C. Yu, Z. Liu, S. Kaya, D. Nordlund, H. Ogasawara, M. F. Toney, A. Nilsson *Nature Chem.* **2010**, *2*, 454-460.

27. R. Harpeness, A. Gedanken *Langmuir*, **2004**, *20*, 3431-3434.

28. S. García, N. Dahal, J. Zhou, H. Celio, A. Dolocan, S. M. Humphrey *Chem. Commun.* **2013**, *49*, 4241-4243.

29. S. Peng, C. Wang, J. Xie, S. Sun *J. Am. Chem. Soc.* **2006**, *128*, 10676-10677.

30. A. H. Latham, M. E. Williams *Acc. Chem. Res.* **2008**, *41*, 411-420.

31. N. Dahal, S. García, J. Zhou, S. M. Humphrey *ACS Nano*, **2012**, *6*, 9433-9446.

32. T. K. Sau, A. L. Rogach *Complex-shaped Metal Nanoparticles*; Wiley-VCH Verlag & Co.: Weinheim, 2012.

33. S. M. Humphrey, M. E. Grass, S. E. Habas, K. Niesz, G. A. Somorjai, T. D. Tilley *Nano Lett.* **2007**, *7*, 785-790.

34. C. O. Kappe *Angew. Chem. Int. Ed.* **2004**, *43*, 6250-6284.

35. S. García, G. W. Piburn, S. M. Humphrey *Microwave-assisted Synthesis of Metallic Nanoparticles*, In *Microwave Engineering of Materials – From Mesoscale to Nanoscale*, Ed. Erwann Guenin; Pan Stanford Publishing: Singapore, 2016.

36. S. García, L. Zhang, G. W. Piburn, G. Henkelman, S. M. Humphrey *ACS Nano* **2014**, *8*, 11512-11521.

37. D. Obermayer, B. Gutmann, C. O. Kappe *Angew. Chem. Int. Ed.* **2009**, *48*, 8321-8324.

38. J. Anwar, U. Shafique, W. uz-Zaman, R. Rehman, M. Salman, A. Dar, J. M. Anzano, U. Ashraf, S. Ashraf *Arab. J. Chem.* **2015**, *8*, 100-104.

39. W. Wang, B. Wang, J. Sun, Y. Mao, X. Zhao, Z. Song *RSC Adv.* **2016**, *6*, 52974-52981.

40. L. Gou, M. Chipara, J. M. Zaleski *Chem. Mater.* **2007**, *19*, 1755-1760.

41. W. Chen, B. Gutman, C. O. Kappe *ChemistryOpen* **2012**, *1*, 39-48.

42. M. B. Gawande, S. N. Shelke, R. Zboril, R. S. Varma *Acc. Chem. Res.* **2014**, *47*, 1338-1348.

43. T. R. Jensen, G. C. Schatz, R. P. Van Duyne *J. Phys. Chem. B* **1999**, *103*, 2394-2401.

44. S. K. Ghosh, T. Pal *Chem. Rev.* **2007**, *107*, 4797-4862.

45. P. Kunal, H. Li, B. L. Dewing, L. Zhang, K. Jarvis, G. Henkelman, S. M. Humphrey, *ACS Catalysis* **2016**, *6*, 4882-4893.

46. A. R. Denton, N. W. Ashcroft, *Phys. Rev. A* **1991**, *43*, 3161.

47. Y. Xiong, J. Chen, B. Wiley, Y. Xia, Y. Yin, Z.-Y. Li, *Nano Lett.* **2005**, *5*, 1237-1242.

48. U. Holzwarth, N. Gibson, *Nature Nanotech.* **2011**, *6*, 534.

49. D. B. Williams, C. B. Carter, *Transmission Electron Microscopy: A Textbook for Materials Science*; Springer: Berlin, 1996.

50. L. Reimer, *Scanning Electron Microscopy: Physics of Image Formation and Microanalysis*; Springer: Berlin, 2013.

51. L. Reimer, *Transmission Electron Microscopy: Physics of Image Formation and Microanalysis*; Springer: Berlin, 2013.

52. K. J. Ganesh, M. Kawasaki, J. P. Zhou, P. J. Ferreira, *Microsc. Microanal.* **2010**, *16*, 614-621.

53. C. C. Chusuei, D. W. Goodman, *X-ray Photoelectron Spectroscopy*, In *Encyclopedia of Physical Science and Technology, Third Edition, Volume 17*; Academic Press: Cambridge, MA, 2002.

54. S. Oswald, W. Brückner, *Surf Interface Anal*, **2004**, *36*, 17-22.

55. X. Hou, B. T. Jones, *Inductively Coupled Plasma/Optical Emission Spectrometry*, In *Encyclopedia of Analytical Chemistry*; John Wiley & Sons Ltd: Chichester, 2000.

56. J. D. Burrington, *Industrial Catalysis: Chemistry and Mechanism*; Imperial College Press, London, **2016**.

57. K. C. Taylor, *Catal. Rev.* **1993**, *35*, 457-481.

58. L. Yin, J. Liebscher, *Chem. Rev.* **2007**, *107*, 133-173.

59. F. Nerozzi, *Platinum Metals Rev.* **2012**, *56*, 236-241.

60. P. Fröhlich, T. Lorenz, G. Martin, B. Brett, M. Bertau, *Angew. Chem. Int. Ed.* **2017**, *56*, 2544-2480.

61. Y. Xia, Y. Xiong, B. Lim, S. E. Skrabalak, *Angew. Chem. Int. Ed* **2009**, *48*, 60-103.

62. L. Vitosa, A. V. Rubana, H. L. Skrivera, J. Kollárb, *Surf. Sci.* **1998**, *411*, 186-202.

63. C. J. Heard, S. Siahrostami, H. Grönbeck, *J. Phys. Chem. C* **2016**, *120*, 995-1003.

64. P. Claus *Top. Catal.* **1998**, *5*, 51-62.

65. H. Kobayashi, K. Kusada, H. Kitagawa *Acc. Chem. Res.* **2015**, *48*, 1551-1559.

66. K. Kusada, H. Kobayashi, R. Ikeda, Y. Kubota, M. Takata, S. Toh, T. Yamamoto, S. Matsumura, N. Sumi, K. Sato, K. Nagaoka, H. Kitagawa *J. Am. Chem. Soc.* **2014**, *136*, 1864-1871.

67. S.-Y. Wang, S. H. Moon, M. Albert Vannice, *J. Catal.* **1981**, *71*, 167-174.

68. S. J. Tauster, *Acc. Chem. Res.* **1987**, *20*, 389-394.

69. X. Liu, M.-H. Liu, Y.-C. Luo, C.-Y. Mou, S. D. Lin, H. Cheng, J.-M. Chen, J.-F. Lee, T.-S. Lin, *J. Am. Chem. Soc.* **2012**, *134*, 10251-10258.

70. K.-W. Park, K.-S. Ahn, Y.-C. Nah, J.-H. Choi, Y.-E. Sung, *J. Phys. Chem. B* **2003**, *107*, 4352-4355.

71. V. B. Parambhath, R. Nagar, K. Sethupathi, S. Ramaprabhu, *J. Phys. Chem. C* **2011**, *115*, 15679-15685.

72. Z. Wu, Y. Mao, X. Wang, M. Zhang, *Green Chem.* **2011**, *13*, 1311-1316.

73. S. K. Beaumont, S. Alayoglu, C. Specht, N. Kruse, G. A. Somorjai, *Nano Lett.* **2014**, *14*, 4792-4796.

74. H. Shen, H. Tang, H. Yan, W. Han, Y. Li, J. Ni, *RSC. Adv.*, **2014**, *4*, 30180-30185.

75. N. Tiengchad, O. Mekasuwandumrong, C. Na-Chiangmai, P. Weerachawanasak, J. Panpranot, *Catal. Commun.* **2011**, *12*, 910-916.

76. C. Li, H. Zhang, D. Jiang, Q. Yang, *Chem. Commun.* **2007**, 547-558.

77. T. Maschmeyer, F. Rey, G. Sankar, J. M. Thomas, *Nature*, **1995**, *378*, 159-162.

78. G. Kennedy, L. R. Baker, G. A. Somorjai *Angew. Chem. Int. Ed.* **2014**, *53*, 3405-3408.

79. G. Kennedy, G. Melaet, H.-L. Han, W. T. Ralston, G. A. Somorjai *ACS Catalysis* **2016**, *6*, 7140-7147.

80. K. S. W. Sing, D. H. Everett, R. A. W. Haul, L. Moscou, R. A. Pierotti, J. Rouquérol, T. Siemieniewska, *Pure Appl. Chem.* **1985**, *57*, 603.

81. S. M. Auerbach, K. A. Carrado, P. K. Dutta (Eds), *Handbook of Zeolite Science and Technology*; Marcel Dekker: New York, 2003.

82. T. Yanagisawa, T. Shimizu, K. Kuroda, C. Kato, *Bull. Chem. Soc. Jpn.* **1990**, *63*, 988.

83. C. T. Kresge, M. E. Leonowicz, W. J. Roth, J. C. Vartuli, J. S. Beck, *Nature* **1992**, *359*, 710.

84. J. S. Beck, J. C. Vartuli, W. J. Roth, M. E. Leonowicz, C. T. Kresge, K. D. Schmitt, C. T.-W. Chu, E. W. Olson, S. B. Sheppard, J. B. McCullen, J. B. Higgins, J. L. Schlenker, *J. Am. Chem Soc* **1992**, *114*, 10834.

85. S. Inagaki, Y. Fukushima, K. Kuroda, *J. Chem. Soc., Chem Commun.* **1993**, 680.

86 A. D. McNaught, A. Wilkinson, *IUPAC. Compendium of Chemical Terminology, The Gold Book*, 2nd Edn; Blackwell Scientific Publications; Oxford, 1997.

87. D. W. Bruce, D. O'Hare, R. I. Walton (Eds), *Porous Materials*; John Wiley & Sons: Chichester, 2011.

88. F. Schüth, *Angew. Chem. Int. Ed.* **2003**, *42*, 3604.

89. A. Taguchi, F. Schüth, *Microporous Mesoporous Mater.* **2005**, *77*, 1.

90. F. Jiao, P. G. Bruce, *Adv. Mater.*, **2007**, *19*, 657.

91. F. Jiao, J. Bao, A. H. Hill, P. G. Bruce, *Angew. Chem. Int. Ed.* **2008**, *47*, 9711.

92. S. Jun, S. H. Joo, R. Ryoo, M. Kruk, M. Jaroniec, Z. Liu, T. Ohsuna, O. Terasaki, *J. Am. Chem. Soc.*, 2000, **122**, 10712-10713.

93. J. Roggenbuck, T. Waitz, M. Tiemann *Micropor. Mesopor. Mat.* **2008**, *113*, 575-582.

94. N. Dahal, I. A. Ibarra, S. M. Humphrey *J. Mater. Chem.* **2012**, *22*, 12675-12681.

95. P. Yang, D. Zhao, D. I. Margolese, B. F. Chmelka, G. D. Stucky, *Nature*, **1998**, *396*, 152.

96. P. Yang, D. Zhao, D. I. Margolese, B. F. Chmelka, G. D. Stucky, *Chem. Mater.* **1999**, *11*, 2813.

97. D. Zhao, J. Feng, Q. Huo, N. Melosh, G. H. Fredrickson, B. F. Chmelka, G. D. Stucky, *Science*, 1998, **279**, 548-552.

98. T.-W. Kim, F. Kleitz, B. Paul, R. Ryoo, *J. Am. Chem. Soc.* **2005**, *127*, 7601-7610.

99. D. W. Bruce, D. O'Hare, I. Richard, *Gas Sorption in the Analysis of Nanoporous Solids*, In *Multi Length-scale Characterization*; Wiley & Sons: Chichester, 2013.

100. P. B. Balbuena, K. E. Gubbins, *Langmuir*, **1993**, *9*, 1801-1814.

101. S. Brunauer, P. H. Emmett, E. Teller, *J. Am. Chem. Soc.*, 1938, **60**, 309-319.

102. E. P. Barrett, L. G. Joyner, P. P. Halenda, *J. Am. Chem. Soc.*, 1951, **73**, 373-380.

103. K. An, G. A. Somorjai, *Catal. Lett.* **2015**, *145*, 233-248.

104. P. Simon, Y. Gogotsi, *Nature Mater.*, 2008, **7**, 845-854.

105. J.-Y. Luo, J.-J. Zhang, Y.-Y. Xia, *Chem. Mater.* **2006**, *18*, 5618.

CHAPTER TWO

1. B. E. Conway, *Electrochemical Supercapacitors: Scientific and Technological Applications*; Springer: Berlin, 2013.
2. A.S. Arico, P. Bruce, B. Scrosati, J. Tarascon, W. Van Schalkwijk, *Nature Mater.*, 2005, **4**, 366-377.
3. Mcdowall J., *Lithium battery technology* — Saft. Winter StatBatt Technical Sessions. StatBatt Technical Sessions. http://www.ewh.iee.org/cmte/PES-SBC, 2004.
4. P. Simon, Y. Gogotsi, *Nature Mater.*, **2008**, *7*, 845-854.
5. M. F. El-Kady, V. Strong, S. Dubin, R. B. Kaner, *Science*, **2012**, *335*, 1326-1330.
6. S. Chen, J. Zhu, X. Wu, Q. Han, X. Wang, *ACS Nano*, **2010**, *4*, 2822-2830.
7. G. Wang, L. Zhang, J. Zhang, *Chem. Soc. Rev.*, **2012**, *41*, 797-828.
8. J. Jiang, Y. Li, J. Liu, X. Huang, C. Yuan, X. W. Lou, *Adv. Mater.*, **2012**, *24*, 5166-5180.
9. X. Lang, A. Hirata, T. Fujita, M. Chen, *Nature Nanotechnol.*, **2011**, *6*, 232-236.
10. M. Zhi, C. Xiang, J. Li, M. Li, N. Wu, *Nanoscale*, **2013**, *5*, 72-88.
11. J. Liu, J. Jiang, C. Cheng, H. Li, J. Zhang, H. Gong, H. J. Fan, *Adv. Mater.*, **2011**, *23*, 2076-2081.
12. S. Bag, C. R. Raj, *J. Mater. Chem. A*, **2016**, *4*, 8384-8394.
13. B. E. Conway, V. Birss, J. Wojtowicz, *J. Power Sources*, **1997**, *66*, 1-14.
14. H. Y. Lee, J. B. Goodenough, *J. Solid State Chem.*, **1999**, *148*, 81-84.
15. S.-L. Kuo, N.-L. Wu, *J. Electrochem. Soc.*, **2006**, *153*, A1317-A1324.
16. J. P. Zheng, T. R. Jow, *J. Electrochem. Soc.*, **1995**, *142*, 6-8.
17. M. N. Patel, X. Wang, D. A. Slanac, D. A Ferrer, S. Dai, K. P. Johnston, K. J. Stevenson, *J. Mater. Chem.*, **2012**, *22*, 3160-3169.
18. H. Wang, H. S. Casalongue, Y. Liang, H. Dai, *J. Am. Chem. Soc.*, **2010**, *132*, 7472-7477.
19. J. T. Mefford, W. G. Hardin, S. Dai, K. P. Johnston and K. J. Stevenson, *Nature Mater.*, **2014**, *13*, 726–732.
20. M. A. Peña, J. L. G. Fierro, *Chem. Rev.*, **2001**, *101*, 1981-2018.
21. S. Jin, T. H. Tiefel, M. McCormack, R. A. Fastnacht, R. Ramesh, L. H. Chen, *Science*, **1994**, *264*, 413-415.
22. A. Sawa, *Mater. Today*, **2008**, *11*, 28-36.

23. L. G. Tejuca, J. L. G. Fierro, *Adv. Catal.*, **1989**, *36*, 237-328.

24. W. G. Hardin, D. A. Slanac, X. Wang, S. Dai, K. P. Johnston, K. J. Stevenson, *Phys. Chem. Lett.*, **2013**, *4*, 1254-1259.

25. W. G. Hardin, J. T. Mefford, D. A. Slanac, B. B. Patel, X. Wang, S. Dai, X. Zhao, R. S. Ruoff, K. P. Johnston, K. J. Stevenson, *Chem. Mater.*, **2014**, *26*, 3368-3376.

26. M. Nandi, K. Sarkar, M. Seikh, A. Bhaumik, *Micropor Mesopor. Mat.*, **2011**, *143*, 392-397.

27. Y. Wang, J. Ren, Y. Wang, F. Zhang, X. Liu, Y. Guo, G. Lu, *J. Phys. Chem. C*, **2008**, *112*, 15293-15298.

28. H. Arandiyan, H. Dai, J. Deng, Y. Liu, B. Bai, Y. Wang, X. Li, S. Xie, J. Li, *J. Catal.*, **2013**, *307*, 327-339.

29. D. Grosso, C. Boissière, B. Smarsly, T. Brezesinski, N. Pinna, P. A. Albouy, H. Amenitsch, M. Antonietti, C. Sanchez, *Nat. Mater.*, **2004**, *3*, 787-792.

30. Y. Liu, H. Dai, Y. Du, J. Deng, L. Zhang, Z. Zhao, C. T. Au, *J. Catal.*, **2012**, *287*, 149-160.

31. R. Chao, R. Munprom, R. Petrova, K. Gerdes, J. R. Kitchin, P. A. Salvador, *J. Am. Ceram. Soc.*, **2012**, *95*, 2339-2346.

32. H. Yang, D. Zhao, *J. Mater. Chem.*, **2005**, *15*, 1217-1231.

33. D. Gu, F. Schüth, *Chem. Soc. Rev.*, **2014**, *43*, 313-344.

34. M. M. Nair, F. Kleitz, S. Kaliaguine, *ChemCatChem*, **2012**, *4*, 387-394.

35. Y. Shi, B. Guo, S. A. Corr, Q. Shi, Y.-S. Hu, K R. Heier, L. Chen, R. Seshadri, G. D. Stucky, *Nano Lett.*, **2009**, *9*, 4215-4220.

36. V. K. Tomer, S. Duhan, *J. Mater. Chem. A*, **2016**, *4*, 1033-1043.

37. D. Zhao, J. Feng, Q. Huo, N. Melosh, G. H. Fredrickson, B. F. Chmelka, G. D. Stucky, *Science*, **1998**, *279*, 548-552.

38. S. Jun, S. H. Joo, R. Ryoo, M. Kruk, M. Jaroniec, Z. Liu, T. Ohsuna, O. Terasaki, *J. Am. Chem. Soc.*, **2000**, *122*, 10712-10713.

39. X. Lai, W. Li, W. Geng, J. Tu, J. Li, S. Qiu, *Angew. Chem. Int. Ed.*, **2006**, *46*, 738-741.

40. P. Półrolniczak, S. Kowalak, *J. Porous. Mat.*, **2010**, *18*, 703-706.

41. J. Roggenbuck, H. Schäfer, T. Tsoncheva, C. Minchev, J. Hanss, M. Tiemann, *Micropor. Mesopor. Mat.*, **2007**, *101*, 335-341.

42. X. Lai, H. Wang, D. Mao, N. Yang, J. Yao, C. Xing, D. Wang, X. Li, *Mater. Lett.*, **2008**, *62*, 3868-3871.

43. M. Sadakane, T. Horiuchi, N. Kato, C. Takahashi, W. Ueda, *Chem. Mater.*, **2007**, *19*, 5779-5785.

44. Y. Liu, H. Dai, Y. Du, J. Deng, L. Zhang, Z. Zhao, *Appl. Catal. B*, **2012**, *119*, 20-31.

45. M. M. Nair, F. Kleitz, S. Kaliaguine, *Chin. J. Catal.*, **2016**, *37*, 32-42.

46. E. P. Barrett, L. G. Joyner, P. P. Halenda, *J. Am. Chem. Soc.*, **1951**, *73*, 373-380.

47. S. Brunauer, P. H. Emmett, E. Teller, *J. Am. Chem. Soc.*, **1938**, *60*, 309-319.

48. H. Yen, Y. Seo, R. Guillet-Nicolas, S. Kaliaguine, F. Kleitz, *Chem. Commun.*, **2011**, *47*, 10473-10475.

49. Y.-Q. Quo, X.-H. Zhang, R. Waeppling, *J. Alloys Compds.*, **2000**, *306*, 133-140.

50. H. Xu, S. Xu, H. Wang, H. Yan, *J. Electrochem. Soc.*, **2005**, *152*, C803-C807.

51. N. N. Kovaleva, O. E. Kusmartseva, K. I. Kugel, A. A. Maksimov, D. Nuzhnyy, A. M. Balbashov, E. I. Demikhov, A. Dejneka, V. A. Trepakov, F. V. Kusmartsev, A. M. Stoneham, *J. Phys.: Condens. Matter*, **2013**, *25*, 155602.

52. C. Ramirez-Castro, O. Crosnier, L. Athouël, R. Retoux, D. Bélanger, T. Brousse, *J. Electrochem. Soc.*, **2015**, *162*, A5179-A5184.

53. Y. Chabre, J. Pannetier, *Progress in Solid State Chemistry*, **1995**, *23*, 1-130.

54. A. E. Fischer, K. A. Pettigrew, D. R. Rolison, R. M. Stroud, J. W. Long, *Nano Lett.*, **2007**, *7*, 281-286.

55. S.-C. Pang, M. A. Anderson, T. W. Chapman, *J. Electrochem. Soc.*, **2000**, *147*, 444-450.

56. H. Zhang, J. Sun, D. Ma, X. Bao, A. Klein-Hoffmann, G. Weinberg, D. Su, R. Schlögl, *J. Am. Chem. Soc.*, **2004**, *126*, 7440-7441.

CHAPTER THREE

1. J. D. Burrington, *Industrial Catalysis: Chemistry and Mechanism*, Imperial College Press, London, **2016**.

2. K. C. Taylor, *Catal. Rev.* **1993**, *35*, 457-481.

3. L. Yin, J. Liebscher, *Chem. Rev.* **2007**, *107*, 133-173.

4. N. R. Shiju, V. V. Guliants, *Appl. Catal. A*. **2009**, *356*, 1-17.

5. B. Yoon, C. M. Wai, *J. Am. Chem. Soc.* **2005**, *127*, 17174-17175.

6. X.-R. Ye, Y. Lin, C. Wang, M. H. Engelhard, Y. Wang, C. M. Wai, *J. Mater. Chem.* **2004**, *14*, 908-913.

7. R. Schlögl, *Angew. Chem. Int. Ed.* **2015**, *54*, 3465-3520.

8. P. Fröhlich, T. Lorenz, G. Martin, B. Brett, M. Bertau, *Angew. Chem. Int. Ed.* **2017**, *56*, 2544-2480.

9. D. Astruc, F. Lu, J. R. Aranzaes, *Angew. Chem. Int. Ed.* **2005**, *44*, 7852-7872.

10. T. P. Bigioni, X. M. Lin, T. T. Nguyen, E. I. Corwin, T. A. Witten, H. M. Jaeger, *Nat. Mater.* **2006**, *5*, 265-270.

11. N. R. Jana, L. Gearheart, C. J. Murphy, *Chem. Mater.* **2001**, *13*, 2313-2322.

12. T. K. Sau, C. J. Murphy, *J. Am. Chem. Soc.* **2004**, *126*, 8648-8649.

13. Y. G. Sun, Y. N. Xia, *Science* **2002**, *298*, 2176-2179.

14. S. García, L. Zhang, G. W. Piburn, G. Henkelman, S. M. Humphrey, *ACS Nano* **2014**, *8*, 11512-11521.

15. H. Kobayashi, K. Kusada, H. Kitagawa, *Acc. Chem. Res.* **2015**, *48*, 1551-1559.

16. S. N. Tripathi, S. R. Bharadwqi, *J. Phase Equilib.* **1994**, 15, 208-212.

17. H. Noh, T. B. Flanagan, B. Cerundolo, A. Craft, *Scr. Metall. Mater.* **1991**, *25*, 225-230.

18. H. Noh, J. D. Clewley, T. B. Flanagan, A. P. Craft, *J. Alloy Compd.* **1996**, *240*, 235-248.

19. A. K. M. F. Kibria, Y. Sakamoto, *Int. J. Hydrogen Energy*, **2000**, *25*, 853-859.

20. H. Kobayashi, H. Morita, M. Yamauchi, R. Ikeda, H. Kitagawa, Y. Kubota, K. Kato, M. Takata, S. Toh, S. Matsumura, *J. Am. Chem. Soc.* **2012**, *134*, 12390-12393.

21. J. Polte, *CrystEngComm*, **2015**, *17*, 6809-6830.

22. N. Dahal, S. García, J. Zhou, S. M. Humphrey, *ACS Nano* **2012**, *6*, 9433-9446.

23. Y. Xiong, J. Chen, B., Wiley, Y. Xia, S. Aloni, Y. Yin, *J. Am. Chem. Soc.* **2005**, *127*, 7332-7333.

24. P. Kunal, H. Li, B. L. Dewing, L. Zhang, K. Jarvis, G. Henkelman, S. M. Humphrey, *ACS Catal.* **2016**, *6*, 4882-4893.

25. W. Tang, G. Henkelman, *J. Chem. Phys.* **2009**, *130*, 194504.

26. G. Kresse, J. Hafner, *Phys. Rev. B: Condens. Matter Mater. Phys.* **1993**, *47*, 558−561.

27. P. E. Blöchl, *Phys. Rev. B: Condens. Matter Mater. Phys.* **1994**, *50*, 17953−17979.

28. G. Kresse, D. Joubert, *Phys. Rev. B: Condens. Matter Mater. Phys.* **1999**, *59*, 1758−1775.

29. J. P. Perdew, K. Burke, M. Ernzerhof, *Phys. Rev. Lett.* **1996**, *77*, 3865−3868.

30. P. Hohenberg, W. Kohn, *Phys. Rev.* **1964**, *136*, B864−B871.

31. W. Kohn, L. J. Sham, *Phys. Rev.* **1965**, *140*, A1133−A1138.

32. H. J. Monkhorst, J. D. Pack, *Phys. Rev. B* **1976**, *13*, 5188−5192.

33. M. Methfessel, A. T. Paxton, *Phys. Rev. B: Condens. Matter Mater. Phys.* **1989**, *40*, 3616−3621.

CHAPTER FOUR

1. R. Ferrando, J. Jellinek, R. L. Johnston, *Chem. Rev.* **2008**, *108*, 845-910.

2. M. B. Cortie, A. M. McDonagh, *Chem. Rev.* **2011**, *111*, 3713-3735.

3. K. Kusada, H. Kobayashi, R. Ikeda, Y. Kubota, M. Takata, S. Toh, T. Yamamoto, S. Matsumura, N. Sumi, K. Sato, K. Nagaoka, H. Kitagawa, *J. Am. Chem. Soc.* **2014**, *136*, 1864-1871.

4. S. García, L. Zhang, G. W. Piburn, G. Henkelman, S. M. Humphrey, *ACS Nano*, **2014**, *8*, 11512-11521.

5. H. Kobayashi, K. Kusada, H. Kitagawa, *Acc. Chem. Res.* **2015**, *48*, 1551-1559.

6. F.-J. Lai, L. S. Sarma, H.-L. Chou, D.-G. Liu, C.-A. Hsieh, J.-F. Lee, B.-J. Hwang, *J. Phys. Chem C* **2009**, *113*, 12674-12681.

7. W. Tang, L. Zhang, G. Henkelman, *J. Phys. Chem. Lett.* **2011**, *2*, 1328-1331.

8. D. Wang, H. L. Xin, H. Wang, Y. Yu, E. Rus, D. A. Muller, F. J. DiSalvo, H. D. Abruña, *Chem. Mater.* **2012**, *24*, 2274-2281.

9. P. Kunal, H. Li, B. L. Dewing, L Zhang, K. Jarvis, G. Henkelman, and S. M. Humphrey, *ACS Catal.* **2016**, *6*, 4882-4893.

10. S.-H. Tsai, Y.-H. Liu, P.-L. Wu, C.-S. Yeh, *J. Mater. Chem.* **2003**, *13*, 978-980.

11. Z.-L. Wang, Y. Ping, J.-M. Yan, H.-L. Wang, Q. Jiang, *Int. J. Hydrogen Energy* **2014**, 4850-4856.

12. H. Zhang, Y. Cao, L. Lu, Z. Cheng, S. Zhang, *Metall. Mater. Trans. B* **2015**, *46B*, 523-530.

13. Q. He, P. J. Miedziak, L. Kesavan, N. Dimitratos, M. Sankar, J. A. Lopez-Sanchez, M. M. Forde, J. K. Edwards, D. W. Knight, S. H. Taylor, C. J. Kiely, G. J. Hutchings, *Faraday Discuss.* **2013**, *162*, 365-378.

14. H. Zhang, L. Lu, Y. Cao, S. Du, Z. Cheng, S. Zhang, *Mater. Res. Bull.* **2014**, *49*, 393-398.

15. S. García, R. M. Anderson, H. Celio, N. Dahal, A. Dolocan, J. Zhou, S. M. Humphrey, *Chem. Commun.* **2013**, *39*, 4241-4243.

16. Y. Xiong, J. Chen, B. Wiley, Y. Xia, *J. Am. Chem. Soc.* **2005**, *127*, 7332-7333.

CHAPTER FIVE

1. D. Castagnolo, L. Botta, M. Botta, *J.Org. Chem.* **2009**, *74*, 3172-3174.

2. P. Claus, *Top. Catal.* **1998**, *5*, 51-62.

3. P. Claus, *Appl. Catal. A* **2005**, *291*, 222-229.

4. L. McEwan, M. Julius, S. Roberts, J. C. Q. Fletcher, *Gold Bull.* **2010**, *43*, 298-306.

5. G. J. Hutchings, *Catal. Today* **2008**, *138*, 9-14.

6. R. Zanella, C. Louis, S. Giorgio, R. Touroude, *J. Catal.* **2004**, *223*, 328-339.

7. J. E. Bailie, G. J. Hutchings, *Chem. Commun.* **1999**, *21*, 2151-2152.

8. M. E. Chiu, D. J. Watson, G. Kyriakou, M. S. Tikhov, R. M. Lambert, *Angew. Chem. Int. Ed.* **2006**, *45*, 7530-7534.

9. Y. K. Du, J. Z. Xu, P. Yang, N. P. Hua, L. Jiang, *Coll. Surf. A* **2005**, 257-258, 75-78.

10. M. Englisch, A. Jentys, J. A. Lercher, *J. Catal.* **1997**, *166*, 25-35.

11. P. Reyes, M. C. Aguirre, G. Pecchi, J. L. G. Fierro, *J. Molec. Catal. A* **2000**, *164*, 245-251.

12. G. Kennedy, L. R. Baker, G. A. Somorjai, *Angew. Chem. Int. Ed.* **2014**, *53*, 3405-3408.

13. G. Kennedy, G. Melaet, H.-L. Han, W. T. Ralston, G. A. Somorjai, *ACS Catalysis* **2016**, *6*, 7140-7147.

14. D. I. Jerdev, A. Olivas, B. E. Koel, *J. Catal.* **2002**, *205*, 278-288.

15. F. Ammari, C. Milone, R. Touroude, *J. Catal*. **2005**, *235*, 1-9.

16. P. Reyes, M. C. Aguirre, J. L. G. Fierro, G. Santori, O. Ferretti, *J. Molec. Catal. A* **2002**, *184*, 431-441.

17. P. Reyes, G. Pecchi, J. L. G. Fierro, *Langmuir* **2001**, *17*, 522-527.

18. M. C. Aguirre, J. L. G. Fierro, P. Reyes, *React. Kinet. Catal. Lett.* **2005**, *84*, 351-358.

19. M. Chatterjee, Y. Ikushima, Y. Hakuta, H. Kawanami, *Adv. Synth. Catal.* **2006**, *348*, 1580-1590.

20. M. E. Grass, R. M. Rioux, G. A. Somorjai, *Catal. Lett.* **2009**, *128*, 1-8.

21. N. Dahal, S. García, J. Zhou, S. M. Humphrey, *ACS Nano* **2012** *6*, 9433-9446.

22. N. Dahal, I. A. Ibarra, S. M. Humphrey, *J. Mater. Chem.* **2012**, *22*, 12675-12681.

23. J. Roggenbuck, T. Waitz, M. Tiemann, *Micropor. Mesopor. Mat.* **2008**, *113*, 575-582.